Isolation of a Bent Dysprosium Bis(amide) Single-Molecule Magnet

Jack Emerson-King, Gemma K Gransbury, George F S Whitehead, Iñigo J Vitorica-Yrezabal, Mathieu Rouzières, Rodolphe Clérac, Nicholas F Chilton, David P Mills

JACS
JOURNAL OF THE AMERICAN CHEMICAL SOCIETY
pubs.acs.org/JACS

Article

Isolation of a Bent Dysprosium Bis(amide) Single-Molecule Magnet

Jack Emerson-King, Gemma K. Gransbury, George F. S. Whitehead, Iñigo J. Vitorica-Yrezabal, Mathieu Rouzières, Rodolphe Clérac,* Nicholas F. Chilton,* and David P. Mills*

Cite This: J. Am. Chem. Soc. 2024, 146, 3331−3342

Read Online

ACCESS | Metrics & More | Article Recommendations | Supporting Information

ABSTRACT: The isolation of formally two-coordinate lanthanide (Ln) complexes is synthetically challenging, due to predominantly ionic Ln bonding regimes favoring high coordination numbers. In 2015, it was predicted that a near-linear dysprosium bis(amide) cation $[Dy\{N(Si^iPr_3)_2\}_2]^+$ could provide a single-molecule magnet (SMM) with an energy barrier to magnetic reversal (U_{eff}) of up to 2600 K, a 3-fold increase of the record U_{eff} for a Dy SMM at the time; this work showed a potential route to SMMs that can provide high-density data storage at higher temperatures. However, synthetic routes to a Dy complex containing only two monodentate ligands have not previously been realized. Here, we report the synthesis of the target bent dysprosium bis(amide) complex, $[Dy\{N(Si^iPr_3)_2\}_2][Al\{OC(CF_3)_3\}_4]$ (**1-Dy**), together with the diamagnetic yttrium analogue. We find U_{eff} = 950 ± 30 K for **1-Dy**, which is much lower than the predicted values for idealized linear two-coordinate Dy(III) cations. Ab initio calculations of the static electronic structure disagree with the experimentally determined height of the U_{eff} barrier, thus magnetic relaxation is faster than expected based on magnetic anisotropy alone. We propose that this is due to enhanced spin−phonon coupling arising from the flexibility of the Dy coordination sphere, in accord with ligand vibrations being of equal importance to magnetic anisotropy in the design of high-temperature SMMs.

INTRODUCTION

Raising the temperatures at which single-molecule magnets (SMMs) exhibit magnetic remanence is key to unlocking their potential applications in high-density data storage, as the liquid helium cooling currently required is expensive and unsustainable for widespread adoption.[1−3] For the last two decades, lanthanide (Ln) SMMs have shown the most promise to achieve this goal,[4−7] with axial dysprosium (Dy) complexes predicted to show the highest energy barriers to magnetic reversal (U_{eff}) as these ligand fields best complement the magnetic anisotropy intrinsic to the Dy(III) ion.[8−10] As the isolation of an ideal axial two-coordinate linear Dy(III) complex is a major synthetic challenge (see below), pentagonal bipyramidal Dy complexes with strongly donating apical alkoxides and five weak equatorial donor ligands were the first SMMs to achieve U_{eff} values > 1000 K.[11] Salts with axial dysprosocenium cations $[Dy(Cp^R)_2]^+$ (Cp^R = substituted cyclopentadienyl) and related derivatives subsequently raised 100 s magnetic blocking temperatures (T_B) ever closer to the boiling point of liquid nitrogen (77 K);[12−22] this was attributed to the rigidity of the coordinated aromatic ligands expediting magnetic relaxation via Raman pathways.[12,23] The current record-holding SMM $[Dy_2(C_5{}^iPr_5)_2(\mu\text{-}I)_3]$ has a U_{eff} of 2345 ± 36 K and a T_B of 72 K, with its $1e^-$ Dy−Dy bond providing a significant contribution to these parameters.[19]

Prior to the isolation of these high-barrier SMMs, the near-linear Ln(II) complexes $[Ln\{N(Si^iPr_3)_2\}_2]$ (Ln = Sm, Eu, Tm, and Yb) were prepared by salt metathesis reactions of 2 equiv of $[K\{N(Si^iPr_3)_2\}]$ with parent LnI_2.[24,25] The experimentally determined atomic coordinates of the Sm(II) derivative (N−Ln−N: 175.5(2)°) were used to calculate that an analogous Dy(III) bis(amide) cation $[Dy\{N(Si^iPr_3)_2\}_2]^+$ could show U_{eff} ≈ 2600 K;[24] this value was over triple that of the magnitude of the record barrier for Dy SMMs at the time (842 K for a polymetallic Dy-doped yttrium alkoxide complex).[26] Further calculations revealed that U_{eff} values could remain >1300 K even if the N−Dy−N angle was reduced to as low as 120°, provided that no additional ligands were coordinated.[27] In the interim, the bent Ln(III) bis(amide) complexes $[Ln\{N(Si^iPr_3)_2\}_2][B(C_6F_5)_4]$ for Ln = Sm, Tm, and Yb were synthesized by oxidation of the parent Ln(II) complexes $[Ln\{N(Si^iPr_3)_2\}_2]$;[24,25,28,29] recently, a related bent Yb(III) bis(amide) complex, $[Yb\{N(SiPh_2Me)_2\}_2][Al\{OC(CF_3)_3\}_4]$, has been reported.[30] However, due to synthetic difficulties

Received: November 7, 2023
Revised: January 9, 2024
Accepted: January 10, 2024
Published: January 29, 2024

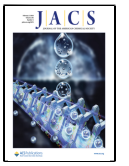

Scheme 1. Synthesis of 1-Ln, 2-Ln, 3-Ln, 4-Ln, and 5-Ln (Ln = Y and Dy)

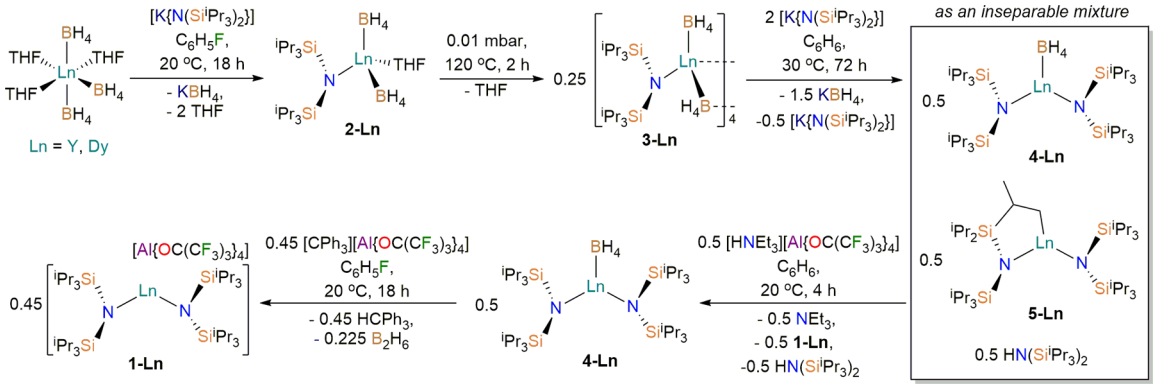

associated with directly installing bulky silylamides at small, charge-dense Ln(III) centers by salt metathesis protocols where side-reactions may occur (see below), the desired Dy(III) bis(amide) cation $[Dy\{N(Si^iPr_3)_2\}_2]^+$ has not previously been isolated. Indeed, the isolation of any Dy complex containing only two monodentate ligands has proved elusive for the wider synthetic chemistry community to date, which is particularly hampered by the predominantly ionic bonding regimes of relatively large Ln cations favoring higher coordination numbers (CNs).[31−33]

Here, we report the isolation and characterization of the bent Dy bis(amide) complex $[Dy\{N(Si^iPr_3)_2\}_2][Al\{OC(CF_3)_3\}_4]$ (**1-Dy**), together with the diamagnetic yttrium analogue **1-Y**, and other complexes that were prepared as starting materials toward these synthetic targets. Magnetic measurements reveal that the SMM properties of **1-Dy** are not as favorable as originally predicted, with magnetization *vs* field hysteresis loops close at zero field at 2 K. Ab initio calculations show that the bent geometry still imposes very large magnetic anisotropy in **1-Dy**, as large as for the first dysprosocenium cation $[Dy(Cp^{ttt})_2]^+$.[12,15,16] As molecular rigidity has been shown to be crucial for controlling spin−phonon relaxation in dysprosocenium cations,[12] we propose that the flexible coordination environment in **1-Dy** enables rapid magnetic relaxation; the large magnetic anisotropy generated by crystal-field (CF) splitting will therefore not necessarily result in a high-barrier Ln SMM unless spin−phonon relaxation enabled by molecular vibrations is adequately controlled.

RESULTS

Synthesis. Complexes **1-Ln** were prepared by the synthetic route shown in Scheme 1; we note that either fluorobenzene or benzene is used as a reaction solvent and in most steps is interchangeable; see the Experimental Section for full details. Analysis of mass balances and in situ ^{1}H NMR spectra for the Y congeners indicated that all reactions proceeded with complete consumption of the starting materials to give the products indicated exclusively. The separate salt elimination reactions of $[Ln(BH_4)_3(THF)_3]$ (Ln = Y and Dy)[34] with 1 equiv of $[K\{N(Si^iPr_3)_2\}]$[24] in fluorobenzene at ambient temperature for 1 h gave the heteroleptic Ln(III) mono(amide) bis(borohydride) complexes $[Ln\{N(Si^iPr_3)_2\}(BH_4)_2(THF)]$ (**2-Ln**) in 79−83% isolated yields following filtration and crystallization from *n*-hexane at −35 °C. The bound THF was removed from **2-Ln** by heating solid samples at 120 °C for 2 h at 0.01 mbar. Recrystallization of the desolvated products from 1,2-difluorobenzene layered with *n*-hexane gave, by slow diffusion, crystals of tetranuclear Ln(III) complexes $[Ln\{N(Si^iPr_3)_2\}(BH_4)(\mu\text{-}BH_4)]_4$ (**3-Ln**) in 54−67% isolated yields. It is critical to remove all of the KBH_4 evolved during the synthesis of **2-Ln**; failure to do so has a deleterious impact on the thermal desolvation step. We also found that samples of **3-Ln** recrystallized in the presence of trace amounts of KBH_4 were contaminated with several crystals of the adducts $[\{Ln\{N(Si^iPr_3)_2\}(BH_4)(\mu\text{-}BH_4)\}_2\{K(\mu\text{-}BH_4)\}]_\infty$ (**3-Ln·0.5KBH$_4$**), for which we report the single-crystal XRD structures here for completeness. The optimized experimental procedures described herein provide pure samples of **2-Ln**.

The separate salt elimination reactions of **3-Ln** with an excess (2 equiv) of $[K\{N(Si^iPr_3)_2\}]$ in benzene at the optimal temperature of 30 °C for 72 h gave full conversion to a mixture of the desired Ln(III) bis(amide) borohydride complexes $[Ln\{N(Si^iPr_3)_2\}_2(BH_4)]$ (**4-Ln**), species assigned as Ln(III) cyclometalates $[Ln\{N(Si^iPr_3)_2\}\{N(Si^iPr_3)[Si(^iPr)_2\{CH(Me)CH_2\}]\text{-}\kappa^2\text{-}N,C\}]$ (**5-Ln**) and $HN(Si^iPr_3)_2$; this product distribution is in accord with deprotonation of a silyl group in situ, likely promoted by a highly Lewis acidic Dy(III) ion.[31] The physical separation of these three highly alkane-soluble species proved challenging; as such, the mixture of **4-Ln**, **5-Ln**, and $HN(Si^iPr_3)_2$ was treated with 0.5 equiv of $[HNEt_3][Al\{OC(CF_3)_3\}_4]$[28] in benzene at 20 °C for 4 h, in order to protonate **5-Ln** and generate the target homoleptic Ln(III) bis(amide) complexes **1-Ln**. After removal of benzene and NEt_3 under vacuum, the resultant oils were triturated with *n*-hexane to give a solution containing a mixture of **4-Ln** and $HN(Si^iPr_3)_2$, together with the solid **1-Ln** and the contaminant $[HNEt_3][Al\{OC(CF_3)_3\}_4]$. The suspensions were filtered, the volatiles of the filtrates were removed in vacuo, and the resultant oils were recrystallized from hexamethyldisiloxane at −30 °C to enable the separation of **4-Ln** from $HN(Si^iPr_3)_2$. Unfortunately, we found the solid mixtures of **1-Ln** and $[HNEt_3][Al\{OC(CF_3)_3\}_4]$ challenging to separate; recrystallization from fluorobenzene solutions layered with *n*-hexane consistently afforded the cocrystallized material of both ionic species. As such, pure samples of **1-Ln** were instead prepared in 73−79% crystalline yields by a hydride abstraction strategy via the reaction of isolated **4-Ln** with 0.9 equiv of $[CPh_3][Al\{OC(CF_3)_3\}_4]$[35] in fluorobenzene at 20 °C for 18 h, followed by slow diffusion of *n*-hexane into the resulting solutions. Treating a mixture of **1-Y** and $[HNEt_3][Al\{OC(CF_3)_3\}_4]$ with excess $[K\{N(Si^iPr_3)_2\}]$ gave ^{1}H, $^{13}C\{^1H\}$ DEPTQ, $^{29}Si\{^1H\}$ DEPT90, and ^{19}F NMR spectra that are consistent with the concomitant formation of **5-Y**, HN-

https://doi.org/10.1021/jacs.3c12427
J. Am. Chem. Soc. 2024, 146, 3331−3342

$(Si^iPr_3)_2$, and $K[Al\{OC(CF_3)_3\}_4]$. We have not yet been able to isolate **5-Ln** in pure form for further characterization, but NMR data for a C_6D_6 solution of a 1:2 mixture of **5-Y** and $HN(Si^iPr_3)_2$ are in line with the proposed cyclometalate formulation (see below).

Spectroscopic Characterization. Bulk samples of crystalline **1-Ln**, **2-Ln**, **3-Ln**, and **4-Ln** were characterized by elemental analysis, multinuclear NMR spectroscopy, and ATR-IR spectroscopy (see Supporting Information Figures S1−S48 for annotated NMR spectra of **1-Ln**, **2-Ln**, **3-Ln**, **4-Ln**, and **5-Y**). The ^1H and $^{13}C\{^1H\}$ DEPTQ NMR spectra of **1-Y** in C_6H_5F solution show the anticipated resonances for the methyl and methine environments of the ^{i}Pr groups, with no additional Y−C or Y−H coupling observed (^{89}Y, I = 1/2, 100% abundance). The $^{29}Si\{^1H\}$ DEPT90 NMR spectrum of **1-Y** shows a single resonance at δ_{Si} = −4.8 ppm, while no resonance was observed in the corresponding spectrum of **1-Dy**. The ^{19}F NMR spectrum of **1-Dy** contains a single broad resonance at δ_F = −97.2 ppm (full-width at half-maximum, fwhm ≈ 280 Hz) for the $[Al\{OC(CF_3)_3\}_4]^-$ anion, that is paramagnetically shifted relative to that seen for **1-Y** (δ_F = −75.1 ppm).

The ^1H, ^{11}B, $^{13}C\{^1H\}$ DEPTQ, and $^{29}Si\{^1H\}$ DEPT90 NMR spectra of diamagnetic **2-Y**, **3-Y**, and **4-Y** were fully assigned in C_6D_6 solution. For brevity, we do not provide a full discussion of all resonances in the ^1H and $^{13}C\{^1H\}$ DEPTQ NMR spectra here as chemical shifts and coupling constants were in line with expected values for the functional groups present. In C_6D_6, the ^{11}B NMR spectra of **2-Y** and **4-Y** feature a single pentet resonance at δ_B = −22.0 ppm ($^1J_{BH}$ = 81 Hz) and δ_B = −21.4 ppm ($^1J_{BH}$ = 86 Hz), respectively. By contrast, for **3-Y**, two broad resonances were observed at δ_B = −20.7 and −3.6 ppm, which we assign as the terminal and bridging BH_4 groups, respectively, implying that this species remains oligomeric in benzene solution. In 1,2-difluorobenzene, a broad pentet resonance was observed at δ_B = −20.9 ppm ($^1J_{BH}$ = 80 Hz) for **3-Y**, consistent with a fluxional monomeric species, possessing equivalent time-averaged terminal BH_4 groups. The $^{29}Si\{^1H\}$ DEPT90 NMR spectra of **2-Y**, **3-Y**, and **4-Y** in C_6D_6 contain a similarly shielded singlet resonance (δ_{Si}/ppm = −2.7, **2-Y**; −3.7, **3-Y**; −3.4, **4-Y**); with **3-Y**, no significant difference was observed in 1,2-difluorobenzene (δ_{Si} = −3.6 ppm). Interpretation of the NMR data for **2-Dy**, **3-Dy**, and **4-Dy** was limited due to paramagnetic broadening of signals, though their $^{11}B\{^1H\}$ NMR spectra contain a single resonance (δ_B/ppm = −18.1, **2-Dy**; −9.9, **3-Dy**; −14.1, **4-Dy**). Additionally, the solution magnetic susceptibilities of these complexes were determined at 298 K by the Evans method;[36] all values obtained (range χT = 12.5−14.2 cm^3 K mol^{-1}) are in line with that expected for a Dy(III) free ion (χT = 14.17 cm^3 K mol^{-1}).[37]

The species assigned as the cyclometalate **5-Y** exhibits three signals in the $^{29}Si\{^1H\}$ DEPT90 NMR spectrum at −3.2, −5.8, and −7.6 ppm. Three magnetically inequivalent silyl groups are also seen in the corresponding ^1H and $^{13}C\{^1H\}$ DEPTQ NMR spectra; the latter spectrum contains a doublet resonance at δ_C = 55.3 ppm, $^1J_{YC}$ = 47.4 Hz with the correct phase for a methylene group, which was assigned to the Y-bound carbon atom. Due to the presence of multiple coincident resonances in $^1H-^{13}C$ HSQC and $^1H-^{13}C$ HMBC NMR spectra, we were unable to assign the associated ^1H resonance. The resonances assigned to **5-Y** in the ^1H, $^{13}C\{^1H\}$ DEPTQ, and $^{29}Si\{^1H\}$ DEPT90 NMR spectra of **5-Y** are comparable to those previously reported for the Y(III) silylamide cyclometalate $[Y\{N(SiMe_3)_2\}_2\{N(SiMe_3)[Si(Me)_2CH_2]$-$\kappa^2$-$N,C\}K]$, which has δ_{Si} = −26.1, −13.5, and −12.0 ppm, and also shows resonances for the bound methylene group at δ_H = −1.27 ppm ($^2J_{YH}$ = 2.6 Hz) and δ_C = 23.6 ppm ($^1J_{YC}$ = 22.9 Hz).[38]

The ATR-IR spectra of each Dy/Y pair in **1-Ln**, **2-Ln**, **3-Ln**, and **4-Ln** overlap with each other and show a number of red-shifted C−H stretching bands that are diagnostic of some methine and methyl groups being in close proximity to and interacting with the Ln centers (see Supporting Information Figures S49−S56). These spectroscopic markers were corroborated by a qualitative analysis of the density-functional theory (DFT)-calculated IR spectra for **1-Y**, **2-Y**, **3-Y**, and **4-Y** (see Supporting Information Figures S57−S60) and are in accord with their crystallographically determined solid-state structures (see below and Supporting Information Figures S61−S70). For **1-Ln**, these features extended down to 2560 cm^{-1}, with the lowest energy modes computationally assigned to the methine C−H group that is closest to the Ln center; the corresponding resonance for **3-Ln** was observed at 2745 cm^{-1}, and for **4-Ln** there are two bands at 2756 and 2729 cm^{-1}. Characteristic borohydride vibrations were also observed for **2-Ln**, **3-Ln**, and **4-Ln**.[39] The apical B−H stretch of the terminal borohydrides corresponded to sharp features at 2486, 2519, and 2495 cm^{-1} for **2-Ln**, **3-Ln**, and **4-Ln**, respectively, while the stretching modes of the B−H bonds that are proximal to the metal gave broad, convoluted bands between 2360 and 2060 cm^{-1} for all complexes.

Solid-State Structural Characterization. The solid-state structures of **1-Ln**, **2-Ln**, **3-Ln**, **4-Ln**, and **3-Ln·0.5KBH$_4$** were characterized by single-crystal X-ray diffraction (XRD). All bond distances and angles are in line with expected values, and these only vary to a small extent for each Dy/Y pair in accord with the difference in six-coordinate ionic radii of Dy(III) (0.912 Å) and Y(III) (0.900 Å),[40] thus we focus our discussion herein on the target axial Dy(III) bis(amide) cation in **1-Dy** (Figure 1). We note that the diffraction data for **1-Dy** are weak (maximum diffraction angle, 55°); see the Experimental Section for further details. The remaining structures and all crystallographic parameters are collated in the Supporting Information (see Figures S61−S71 and Tables S1−S3).

The $[Dy\{N(Si^iPr_3)_2\}_2]^+$ cation exhibits a bent geometry, with a N−Dy−N angle that deviates significantly from linearity (128.7(2)°), with the NSi_2 fragments in a staggered conformation (twist angle: 63.12(6)°) and at a mean Dy−N distance of 2.206(7) Å. The structure of this cation is similar to the previously reported Sm, Tm, and Yb congeners,[28] with deviations in metrical parameters expected on the basis of variation of Ln(III) cation size and Lewis acidity.[31] In common with the previously reported heavy $[Ln\{N(Si^iPr_3)_2\}_2]^+$ cations, the Dy coordination sphere of **1-Dy** is completed by three short Dy···Si (range: 3.207(2)−3.229(2) Å), six short Dy···C (range: 2.845(5)−3.036(7) Å), and six short Dy···H distances (range: 2.293−2.455 Å) for methine and methyl fragments of three different ^{i}Pr groups. These interactions are presumably driven by the electrostatic stabilization of the coordinatively unsaturated Dy(III) center by the electron density of the Si−C/C−H bonds of the silyl groups, which are proposed to set the bent geometry of the cation, as previously described for Sm, Tm, and Yb congeners.[28] The Dy atom is sterically protected by this extremely bulky ligand system, with all visible access channels restricted to <3.4% of the solid angle at Dy (Figure S71).[41] Powder XRD was performed on a sample of

https://doi.org/10.1021/jacs.3c12427
J. Am. Chem. Soc. 2024, 146, 3331−3342

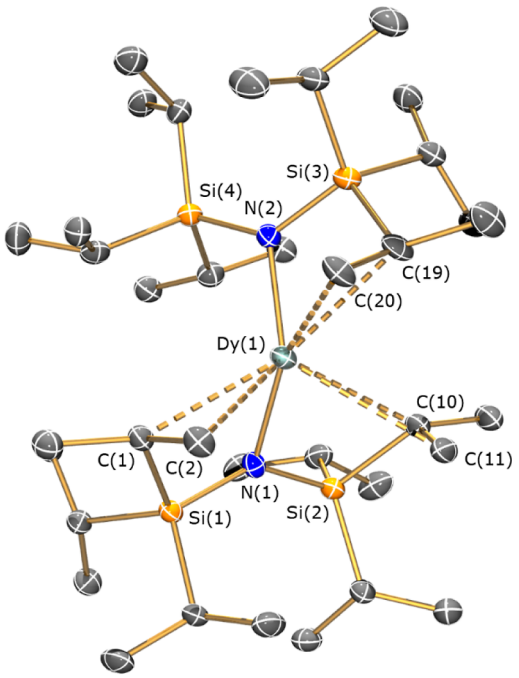

Figure 1. Solid-state structure of the cation of **1-Dy** at 100(2) K. Displacement ellipsoids are set at 50% probability level. Hydrogen atoms and the $[Al\{OC(CF_3)_3\}_4]^-$ counteranion are omitted for clarity. Selected bond distances (Å) and angles (deg): Dy(1)−N(1): 2.209(5); Dy(1)−N(2): 2.202(5); Dy(1)···C(1): 2.845(5); Dy(1)···C(2): 2.987(6); Dy(1)···C(10): 2.883(7); Dy(1)···C(11): 3.036(7); Dy(1)···C(19): 2.863(6); Dy(1)···C(20): 2.929(6); Dy(1)···Si(1): 3.215(2); Dy(1)···Si(2): 3.229(2); Dy(1)···Si(3): 3.207(2); N(1)−Dy(1)−N(2): 128.7(2).

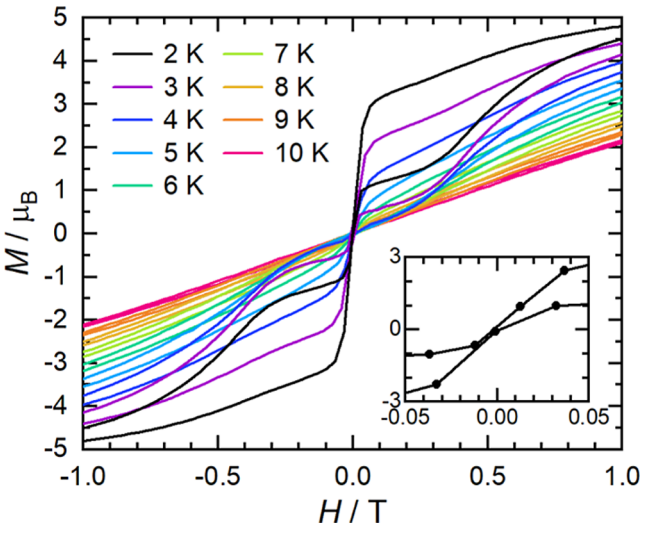

Figure 2. *M vs H* hysteresis loops of **1-Dy** suspended in eicosane from 2 to 10 K in between −1 and +1 T; the inset shows closing of the loop at zero field at 2 K. Sweep rate is 22 Oe s^{-1}.

microcrystalline **1-Dy** (see Supporting Information Figure S72 and Table S4), confirming that the single-crystal structure obtained is representative of the bulk crystalline material used for magnetic characterization.

Magnetic Measurements. The static and dynamic magnetic properties of **1-Dy** in the solid state and as a 200 mM frozen solution sample in fluorobenzene were probed by dc (direct current) and ac (alternating current) susceptibility measurements (see Supporting Information Figures S73−S107 and Tables S5−S10). The χT value determined at 300 K under a 0.1 T dc field (14.75 cm^3 K mol^{-1}, Figure S73) is slightly higher than that determined at 298 K in fluorobenzene solution (12.97 cm^3 K mol^{-1}, Figure S74) and the expected Dy(III) free ion value (14.17 cm^3 K mol^{-1}).[37] We observe a regular decrease in χT with decreasing temperature as excited CF states are thermally depopulated until *ca.* 10 K where there is a sharper decrease, reaching χT = 7.71 cm^3 K mol^{-1} at 2 K (Figure S73); zero field-cooled (ZFC) and field-cooled (FC) data collected in a smaller 0.001 or 0.005 T dc field show that this drop is mainly due to Zeeman depopulation effects, dropping only to χT = 11.3 cm^3 K mol^{-1} at 1.85 K (Figures S76 and S77). Magnetization (M) *vs* field (H) experiments show that the magnetization saturates at M_{sat} = 5.42 μ_B under a 7 T applied dc field (Figure S78), suggesting an $m_J = \pm 15/2$ ground state (M_{sat} = 5.00 μ_B).[7] The waist-restricted M *vs.* H hysteresis loops of **1-Dy** (Figure 2) are typical for Ln SMMs;[5] the presence of rapid quantum tunneling of magnetization (QTM) is evidenced by the closed loop at zero field at 2 K (Figure S80). The nonlinearity of the M *vs.* H data at low fields is in accord with rapid QTM being quenched in increasing fields.

Magnetization

Ac susceptibility measurements of polycrystalline **1-Dy** were performed up to 10 kHz to study the magnetization dynamics. Temperature- and frequency-dependent behavior were seen for the in-phase (χ') and out-of-phase (χ'') components of ac susceptibility in zero dc field, with maxima in χ'' due to slow relaxation of the magnetization present between 2 and 108 K (Figures S89−S91, Table S5).[42] The ac data were fit using the generalized Debye model[42,43] to extract relaxation times along with estimated standard deviations (ESDs) as arising from a distribution in the relaxation times;[44,45] note that T_B is not defined in zero field as τ < 100 s at all temperatures. The temperature dependence of the magnetic relaxation time suggests Orbach relaxation at high temperatures, Raman-I relaxation at intermediate temperatures, and QTM at the lowest temperatures (Figure 3a).[2] The average temperature-dependent relaxation time was modeled using eq 1, giving initial estimates of U_{eff} = 850 K, $\tau_0 = 6.8 \times 10^{-9}$ s, $C = 8 \times 10^{-4}$ s^{-1} K^{-n}, n = 3.3, and τ_{QTM}^{-1} = 7.4 s (Figure S104). Ac susceptibility measurements in a 0.08 T dc field (Figures S92−S94, Table S6) indicate that QTM is quenched under these conditions (Figure 3a), and the average relaxation time can be fit with eq 1, with $\tau_{QTM}^{-1} = 0$ to give U_{eff} = 915 K, $\tau_0 = 3.8 \times 10^{-9}$ s, $C = 4 \times 10^{-5}$ s^{-1} K^{-n}, and n = 4.1 (Figure S105).

$$\tau^{-1}(\mathrm{T}) = CT^n + \tau_0^{-1}\exp\left(-\frac{U_{eff}}{T}\right) + \tau_{QTM}^{-1} \quad (1)$$

$$\tau^{-1}(\mathrm{H}) = \frac{\tau_{QTM}^{-1}}{1 + QH^p} + C_T + DH^m \quad (2)$$

$$\tau^{-1}(\mathrm{H, T}) = \frac{\tau_{QTM}^{-1}}{1 + QH^p} + CT^n + AH^4T + \tau_0^{-1}\exp\left(-\frac{U_{eff}}{T}\right) \quad (3)$$

Performing an ac susceptibility experiment at 12 K as a function of magnetic field allows us to investigate field-

https://doi.org/10.1021/jacs.3c12427
J. Am. Chem. Soc. 2024, 146, 3331−3342

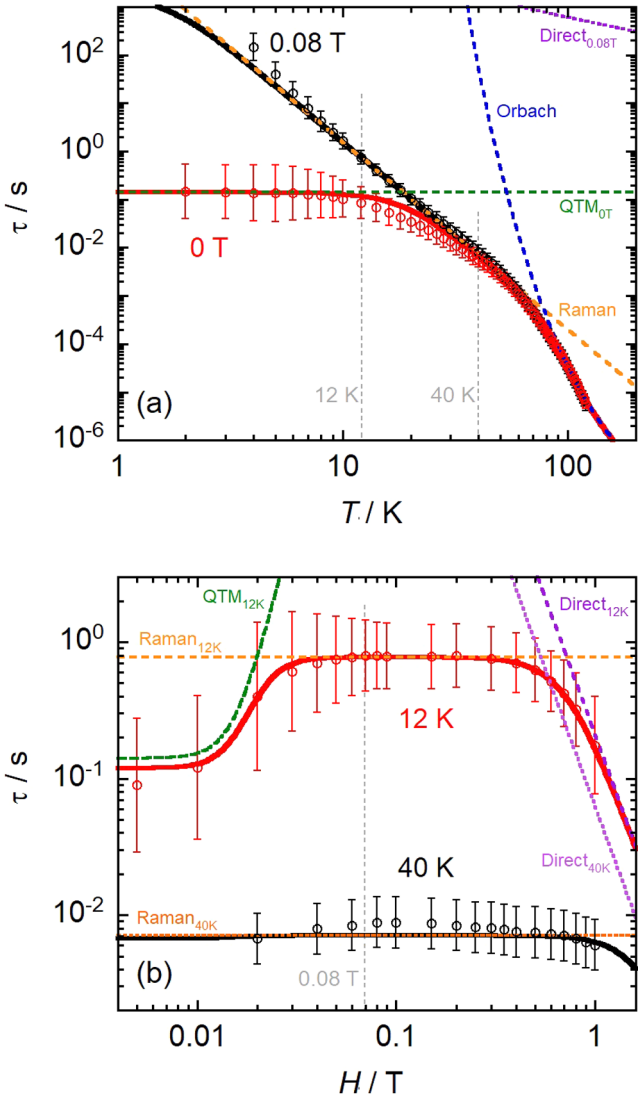

Figure 3. Temperature dependence (a; at 0 and 0.08 T) and field-dependence (b; at 12 and 40 K) of the magnetic relaxation time (τ) for **1-Dy**. Open circles are the experimental data and bars denote ESDs from the generalized Debye model and the relaxation time distribution.[42,43] Solid lines are the result of the best global simulation (eq 3) as discussed in the text.

dependent relaxation dynamics (Figures S95 and S96, Table S7). The relaxation time increases with increasing field below *ca.* 0.04 T and then plateaus until *ca.* 0.4 T, above which it increases again (Figure 3b). This is consistent with the quenching of QTM in low fields,[46,47] followed by a plateau defined by the field-independent processes (predominately the Raman-I mechanism,[48] as the Orbach contribution is insignificant at 12 K), and then an increase at higher fields owing to either a field-dependent Raman-II or a Direct single-phonon mechanism.[47,48] Fitting the average field-dependent relaxation time with a model accounting for these three terms (eq 2) gives $\tau_{QTM}^{-1} = 10\ s^{-1}$, $Q = 2 \times 10^{7}\ T^{-p}$, $p = 3.8$, $C_{12\ K} = 1.3\ s^{-1}$, $D = 4.4\ s^{-1}\ T^{-m}$, and $m = 3.8$ (Figure S106). The field exponent of the Raman-II/Direct term (m) is approaching the value expected for the single-phonon Direct process in the high-temperature limit of $m = 4$,[49] and so we suggest this as the more likely mechanism.

The parameters of these individual models are in reasonable agreement; however, we sought to determine parameters for a unified model that can describe the complete field and temperature dependence of the relaxation time. To do so, we refined a set of global parameters for QTM, Raman-I, Direct, and Orbach processes (eq 3) against the temperature-dependent rates at 0 and 0.08 T dc fields and the field-dependent rates at 12 and 40 K (Figures S97 and S98, Table S8) using the individual model parameters as starting values (Figure 3). To reduce the number of parameters, we assumed a Direct process with H^4 field dependence and linear temperature dependence,[50] and τ_{QTM}^{-1} was fixed to the average of the 2−5 K rates in 0 dc field. This function is complex and nonlinear, so errors were determined by independently varying each parameter such that the resultant time lies within one ESD of the experimental distributions. The global model provides good reproduction of all experimental data with the following parameters: $\tau_{QTM}^{-1} = 7.1^{+0.8}_{-0.6}\ s^{-1}$, $Q = 2^{+2}_{-1} \times 10^{10}\ T^{-p}$, $p = 5.7^{+0.5}_{-0.2}$, $C = 8^{+2}_{-1} \times 10^{-5}\ s^{-1}\ K^{-n}$, $n = 3.9 \pm 0.1$, $A = 0.4 \pm 0.2\ s^{-1}\ K^{-1}\ T^{-4}\ s^{-1}$, $U_{eff} = 950 \pm 30$ K, and $\tau_0 = (2.6 \pm 0.4) \times 10^{-9}$ s. The zero-field QTM rate (τ_{QTM}^{-1}) is rapid, in agreement with the M *vs* H hysteresis data, and the field-exponent (p) is slightly larger than the axial SMM $[Dy(O^tBu)(Cl)(THF)_5][B(C_6F_5)_4]$ of 3.8 ± 0.2.[46]

It has previously been shown that the linearity of the N−Dy−N angle in bis−amide complexes should correlate with U_{eff}.[27] We hypothesized that in solution the N−Dy−N angle in **1-Dy** may increase, as has been observed for the Yb congener;[28] phase-dependent geometries have previously been shown to be a feature of f-block silylamide chemistry.[54] A *ca.* 200 mM solution of **1-Dy** in fluorobenzene was prepared by dissolving a known mass of solid in an appropriate mass of solvent, and this solution was flash-frozen in liquid nitrogen. The ac susceptibility experiments for the frozen solution sample give relatively noisy data (Figure S99); the Cole−Cole profiles are much broader and more asymmetric than the solid-state data and cannot be modeled well by the generalized Debye model. To account for the asymmetric distribution in relaxation times, the low-temperature (2−13 K) data were fit to a phenomenological Havriliak−Negami model (eq 4, Figures S100 and S101, Table S9) which includes parameters for the skew (γ) and the width (α) of the relaxation time distribution. For symmetric distributions ($\gamma = 1$), the Havriliak−Negami model becomes equivalent to the generalized Debye model.[51]

$$\chi(\omega) = \chi_S + \frac{\chi_T - \chi_S}{[1 + (i\omega\tau)^{1-\alpha}]^{\gamma}} \quad (4)$$

At higher temperatures (31−79 K), a shoulder in the Cole−Cole plot emerges, and the ac data are best fit by a double-generalized Debye model (Figures S102 and S103 and Table S10). Furthermore, magnetic hysteresis loops are more open in frozen solution than in the solid state (but remain waist-restricted, Figures S86−S88). The low-temperature frozen solution relaxation data show a comparable QTM rate to the solid-state sample, whereas the high-temperature fits encompass a major component (65%) that has rates in line with the solid-state data and a minor component (35%) that has considerably slower dynamics (Figure S107); the minor component and the hysteresis data are both in accord with a sample that relaxes measurably slower than the solid-state material. These observations are consistent with the frozen solution sample containing a broader and more asymmetric

https://doi.org/10.1021/jacs.3c12427
J. Am. Chem. Soc. 2024, 146, 3331−3342

distribution of molecular geometries, with some molecules in the distribution having larger N−Dy−N angles and hence larger anisotropy and slower magnetic relaxation rates; we note that the interactions of Si−C/C−H bonds of the silyl groups with the Dy(III) ion seen in the solid state are also likely to be important in the solution phase.

Ab Initio Calculations. First-principles complete active space self-consistent field spin−orbit (CASSCF-SO) calculations were performed using OpenMolcas[52] from the atomic coordinates of the cation in **1-Dy** determined by single-crystal XRD. These calculations show that the ground state is an almost pure $m_J = \pm 15/2$ Kramers doublet, with Ising-like g-values ($g_x = g_y = 0$, $g_z = 19.86$; Table S11). The first two excited Kramers doublets are at 616 K (98% $m_J \pm 13/2$, 0.8° between excited g_z and ground g_z) and 1185 K (94% $m_J \pm 11/2$, 1.6°) above the ground state (Figures S108 and S109), with the second excited state being highly mixed.[12]

DISCUSSION

All previously reported examples of axial Dy SMMs with no equatorial donor ligands contain bulky η^5-cyclopentadienyl ligands or related derivatives,[12−22] hence there is no literature precedent for refined magnetostructural comparisons with **1-Dy**. The Dy(III) ion in **1-Dy** is bound by two monodentate σ-donor bis(silyl)amides; although some of the charge density is delocalized about the ligand scaffolds due to negative hyperconjugation with the triisopropylsilyl groups,[53,54] the N atoms can be formally treated as point-charge Lewis bases to a first approximation. This differs from the highest-performing Dy SMMs bound by π-aromatic ligands in the literature,[12−22] which donate the electron density to Dy from delocalized molecular orbitals located about a pentagonal arrangement of atoms. Accordingly, the degree of magnetic anisotropy and the purity of m_J states should be more sensitive to deviations from ideal linearity in complexes like **1-Dy** than for a sandwich-type complex. We previously reported the solid-state structures of the bent Tm(III) complex $[Tm\{N(Si^iPr_3)_2\}_2][B(C_6F_5)_4]$ (N−Tm−N: 125.49(9)°),[28] and considering that the six-coordinate ionic radii of Dy(III) (0.912 Å) and Tm(III) (0.88 Å) are quite similar,[40] we anticipated a similar N−Dy−N angle for **1-Dy**. However, previous computational studies on a series of model two-coordinate DyL_2 compounds (L = mono- or dianionic monodentate C- or N-donor ligand) predicted that U_{eff} should decrease regularly with bending (e.g., $[Dy\{N(SiH_3)_2\}_2]$; $U_{eff} = 2072$ cm^{-1} at 180° N−Dy−N and 919 cm^{-1} at 120°),[27] thus **1-Dy** remained a desirable synthetic target.

The N−Dy−N angle in **1-Dy** (128.7(2)°) is far more bent than the corresponding $Cp_{centroid}\cdots Dy\cdots Cp_{centroid}$ angle of any isolated dysprosocenium cation (smallest known, $[(C_5{}^iPr_4H)_2]^+$ = 147.2(8)°),[13] and **1-Dy** has shorter Dy−N bonds (2.206(7) Å mean) than the mean $Dy\cdots Cp_{centroid}$ distances in these systems (e.g., $[Dy(C_5{}^iPr_4H)_2]^+$ = 2.29(1) Å).[13] Despite substantially different structures, a comparison of the total calculated CF splitting of the $^6H_{15/2}$ multiplet between **1-Dy** and $[Dy(Cp^{ttt})_2]^+$ (for which we have commensurate CASSCF-SO calculations; Cp^{ttt} = {$C_5H_2{}^tBu_3$-1,2,4}, mean $Dy\cdots Cp_{centroid}$ = 2.416(2) Å and mean $Cp_{centroid}\cdots Dy\cdots Cp_{centroid}$ = 152.56(7)°)[12] shows that **1-Dy** has a substantially larger overall splitting (2459 K *vs* 2124 K); however, the energy gap to the first excited state is slightly smaller (616 *vs* 703 K), and the second excited state of **1-Dy** has large transverse g-values. Although these calculations may not fully capture the full effects of the multiple Dy···Si−C/C−H interactions present in **1-Dy**, we note that the two close equatorial Dy···H−C contacts seen in the solid-state structure of $[Dy(Cp^{ttt})_2][B(C_6F_5)_4]$ did not appear to have a significant effect on SMM behavior.[12] However, the U_{eff} for **1-Dy** (950 ± 30 K) is roughly half the value observed for $[Dy(Cp^{ttt})_2]^+$ (1780 ± 40 K).[44] Conventional usage of the average transition matrix elements of magnetic moment to infer magnetic relaxation probabilities[27] suggests that the U_{eff} value for **1-Dy** should be near the top of the CF manifold (Figure S108), while the experimentally determined U_{eff} value lies in between the first and second excited states. This discrepancy highlights that the static electronic structure alone is insufficient to predict relaxation dynamics. While this would be an excellent opportunity to deploy our recent methods to calculate magnetic relaxation dynamics ab initio,[55,56] unfortunately, for **1-Dy**, there are eight formula units in the crystallographic unit cell (1472 atoms), thus this system is currently too large to perform periodic DFT calculations. We propose that the modulation of the CF by phonons (i.e., spin−phonon coupling) has a larger impact on the electronic states in **1-Dy** than for $[Dy(Cp^R)_2]^+$ because in the former complex the CF is almost exclusively dominated by two flexible monatomic donor ligands rather than the more rigid η^5-Cp^R rings in $[Dy(Cp^R)_2]^+$ and related derivatives,[12−22] which have been shown to be crucial for dictating spin dynamics in $[Dy(Cp^{ttt})_2]^+$.[57]

CONCLUSIONS

In this work, the isolation of compounds containing the $[Dy\{N(Si^iPr)_3\}_2]^+$ cation has realized a long-standing goal to synthesize a formally two-coordinate Dy(III) complex, allowing the magnetic properties of this new class of SMM to be determined. We have found a larger than predicted effect of the molecular geometry on SMM behavior, with the significantly bent $[Dy\{N(Si^iPr)_3\}_2]^+$ cation showing relatively low-lying and highly mixed excited m_J states. Frozen solution magnetic data indicate a species with substantially slower relaxation dynamics, suggesting that a more linear N−Dy−N angle can be adopted in this phase, but this could not be unambiguously confirmed. We propose that fast magnetic relaxation in $[Dy\{N(Si^iPr)_3\}_2]^+$ arises from a combination of its large deviation from linearity and the flexible coordination environment providing multiple close Dy···H−C/C−Si contacts, in accord with the rigidity of coordinated ligands being of equal importance to the control of molecular geometry for SMMs to show high-blocking temperatures.

EXPERIMENTAL SECTION

Experimental Materials and Methods. All manipulations were conducted under argon with the strict exclusion of oxygen and water by using Schlenk line and glovebox techniques. Glassware was flame-dried under vacuum prior to use. Argon was passed through a column of activated 3 Å molecular sieves and Cu catalyst prior to use. Isolated compounds were dried in vacuo on a Schlenk line to the point at which the flask could maintain a constant static pressure of less than 5 × 10^{-3} mbar. C_6H_6 and C_6D_6 were purchased in anhydrous form, degassed, and stored under argon over a K mirror or activated 3 Å molecular sieves, respectively. *n*-Hexane was refluxed over molten K for 3 days, distilled, and stored under argon over a K mirror. C_6H_5F and 1,2-$C_6H_5F_2$ were stirred over neutral alumina for 4−6 h, filtered, refluxed over CaH_2 for 3 days, distilled, and stored under argon over activated 3 Å molecular sieves. Hexamethyldisiloxane (HMDSO) was refluxed over CaH_2 for 3 days, distilled, and stored under argon over activated 3 Å molecular sieves. $[Ln(BH_4)_3(THF)_3]$ (Ln = Y, Dy),[34]

https://doi.org/10.1021/jacs.3c12427
J. Am. Chem. Soc. 2024, 146, 3331−3342

$[HNEt_3][Al\{OC(CF_3)_3\}_4]$,[17] and $[CPh_3][Al\{OC(CF_3)_3\}_4]$[35] were prepared according to literature procedures; $[K\{N(Si^iPr_3)_2\}]$ was prepared by an adapted literature procedure,[24] which is detailed in the Supporting Information.

NMR spectra (see Figures S1−S48) of **1-Ln**, **2-Ln**, **3-Ln**, **4-Ln**, **5-Y**/$HN(Si^iPr_3)_2$, $HN(Si^iPr_3)_2$, and $[K\{N(Si^iPr_3)_2\}]$ were recorded at 298 K on a Bruker AVIII HD 400 cryoprobe spectrometer operating at 400.07 (^{1}H) 128.36 (^{11}B), 100.60 (^{13}C), 376.40 (^{19}F), or 79.48 (^{29}Si) MHz. Chemical shifts are reported in ppm and coupling constants in Hz. ^{1}H and $^{13}C\{^1H\}$ DEPTQ NMR spectra recorded in C_6D_6 were referenced to the solvent signal.[58] Spectra recorded in protonated solvents were locked to, and where possible referenced with, an internal sealed capillary of C_6D_6. The solution magnetic susceptibilities of **1-Dy**, **2-Dy**, **3-Dy**, and **4-Dy** were determined at 298 K by the Evans method;[36] ^{1}H NMR spectra recorded in C_6H_5F or 1,2-$C_6H_4F_2$ were referenced using the highest intensity peak of the highest frequency fluoroarene multiplet (δ_H: 6.87 or 6.85 respectively). $^{11}B/^{11}B\{^1H\}$ (H_3BO_3/D_2O), ^{19}F ($C_7H_5F_3/CDCl_3$), and $^{29}Si\{^1H\}$ DEPT90 ($SiMe_4$) NMR spectra were referenced to external standards. The $C(CF_3)_3$ carbon resonances of the $[Al\{OC(CF_3)_3\}_4]^-$ anion were not observed in the $^{13}C\{^1H\}$ NMR spectra of **1-Ln**, likely due to quadrupolar broadening by the 100% abundant I = 5/2 ^{27}Al nuclei and coupling to multiple 100% abundant I = 1/2 ^{19}F nuclei.

ATR-IR spectra of **1-Ln**, **2-Ln**, **3-Ln**, and **4-Ln** were recorded as microcrystalline powders using a Bruker Alpha FT-IR spectrometer with a Platinum-ATR module within a nitrogen-filled glovebox at ambient temperature (see Figures S49−S56). Elemental analysis (C, H, and N) samples were prepared in an argon-filled glovebox, and the analysis was carried out either by Mr. Martin Jennings and Mrs. Anne Davies at the Microanalytical Service, Department of Chemistry, the University of Manchester, or the Elemental Analysis Services Team, Science Centre, London Metropolitan University. Elemental analysis values obtained for **1-Ln**, **2-Ln**, **3-Ln**, and **4-Ln** typically gave carbon compositions that were lower than expected values; this phenomenon has commonly been ascribed to incomplete combustion due to carbide formation, and we note that we have previously observed low carbon values reproducible for Ln $\{N(Si^iPr_3)_2\}$ complexes.[24,25,28,29]

Single-crystal XRD data were collected on either an Oxford Diffraction Agilent Supernova diffractometer equipped with a CCD area detector and a mirror-monochromated Mo Kα source (**1-Y**, **2-Dy**, **3-Dy**, **3-Dy·0.5KBH$_4$·1,2-$C_6H_4F_2$**, and **4-Y**), a Rigaku XtalLAB Synergy-S diffractometer equipped with a HyPix 6000HE photon counting pixel array detector with a mirror-monochromated Mo Kα X-ray source (**4-Dy**), or a Rigaku FR-X diffractometer equipped with a HyPix 6000HE photon counting pixel array detector and a mirror-monochromated X-ray source (**1-Dy**, **2-Y**, **3-Y**, and **3-Y·0.5KBH$_4$·C_6H_6**) (λ = 0.71073 Å for Mo Kα or λ = 1.5418 Å for Cu Kα radiation, Figures S61−S71 and Tables S1−S3). Intensities were integrated from data recorded on 0.5° (**1-Dy**, **2-Y**, **3-Y**, and **3-Y·0.5KBH$_4$·C_6H_6**), or 1° (**1-Y**, **2-Dy**, **3-Dy**, **3-Dy·0.5KBH$_4$·1,2-$C_6H_4F_2$**, **4-Dy**, and **4-Y**) frames by ω rotation. Cell parameters were refined from the observed positions of all strong reflections in each data set. A Gaussian grid face-indexed with a beam profile was applied for all structures.[59] The structures were solved using SHELXT;[60] the data sets were refined by full-matrix least-squares on all unique F^2 values.[60] Anisotropic displacement parameters were used for all non-hydrogen atoms with constrained riding hydrogen geometries, with the exception of borohydride H atoms, which were located in the difference map and refined isotropically; U_{iso}(H) was set at 1.2 (1.5 for methyl groups) times U_{eq} of the parent atom. The largest features in final difference syntheses were close to heavy atoms and were of no chemical significance. CrysAlisPro[59] was used for control and integration, and SHELX[60,61] was employed through OLEX2[62] for structure solution and refinement. ORTEP-3[63] and POV-Ray[64] were used for molecular graphics. Despite the use of a highly intense X-ray source (Rigaku FR-X rotating anode), crystals of **1-Dy** and **3-Dy** only diffracted to 0.94 and 1.06 Å of resolution, respectively, and thus the data were trimmed accordingly. Complex **3-Dy** was also found to be highly sensitive to X-ray irradiation, presenting signs of beam damage (reduction of data resolution and diffracted intensities) with moderate X-ray exposure at 100 K. The data affected by the beam damage were removed, leading to a low completeness (91%) at 1.06 Å.

Powder XRD data of a microcrystalline sample of **1-Dy** mounted with a minimum amount of Fomblin were collected at 100(2) K using a Rigaku FR-X rotating-anode single-crystal X-ray diffractometer using Cu Kα radiation (λ = 1.5418 Å) with a HyPix-6000HE detector and an Oxford Cryosystems nitrogen flow gas system (Figure S72). Data were collected at θ between 2 and 70° with a detector distance of 150 mm and a beam divergence of 1.5 mRad using CrysAlisPro.[59] For data processing, the instrument was calibrated using silver behenate as standard, then the data were reduced and integrated using CrysAlisPro.[59] Le Bail profile analysis was performed using JANA2006 software.[65]

Magnetic measurements of **1-Dy** (Figures S73−S107 and Tables S5−S10) were performed on a Quantum Design MPMS3 superconducting quantum interference device (SQUID) magnetometer at The University of Manchester or an MPMS XL magnetometer or a PPMS EverCool II susceptometer housed at the Centre de Recherche Paul Pascal at temperatures between 1.8 and 300 K and dc magnetic fields ranging from −7 to +7 T (MPMS3 and MPMS XL) or −9 to +9 T (PPMS EverCool II).

The MPMS3 measurements were collected on a finely ground powder sample of **1-Dy** (27.4 mg) restrained in eicosane (22.0 mg) and a 200 mM fluorobenzene (0.102 g) solution of **1-Dy** (35.7 mg); these samples were prepared in a glovebox under an atmosphere of argon loaded into borosilicate tubes, which were later flame-sealed under vacuum and loaded into a plastic straw held in place by friction between the diamagnetic tape at the top of the tube and the straw. The solution sample was flash-frozen in liquid nitrogen and rapidly cooled in zero field after loading into the instrument. Measurements were performed in dc scan mode using 40 mm scan length and 6 s scan time. Equilibrium susceptibility measurements were performed on cooling in temperature settle mode 1.8−300 K (solid) or 1.8−180 K (frozen solution) in 0.1 T dc field. Field dependence (H) of the magnetization (M) curves (2 K, 0−7 T) and M *vs* H hysteresis curves (±5 T for 2−7 K; ±3 T for 8−10 or 12 K) were performed in continuous sweep mode with a sweep rate of 22 Oe s^{-1}. Raw magnetic data were scaled for the shape of the sample using a Quantum Design MPMS3 Geometry Correction Simulator (correction factor: 1.003 for solid and 0.817 for solution), corrected for the diamagnetic contribution of the sample holder (straw + borosilicate tube) and for the mass of eicosane using calibrated blanks or for the mass of fluorobenzene using Pascal's constants.[66] The magnetic susceptibility was corrected for the intrinsic diamagnetism of the sample estimated as the molecular weight (g mol^{-1}) multiplied by -0.5×10^{-6} cm^3 K mol^{-1}. Ac magnetic data were recorded for the frozen solution of **1-Dy** at 0.1−1000 Hz between 2 and 76 K. Low-temperature (2−13 K) ac data were fit to the Havriliak−Negami model, and high-temperature (31−79 K) data were fit to the double-generalized Debye model in CC-FIT2 5.0.1.[44,45,67]

The MPMS XL and PPMS EverCool II measurements were collected on polycrystalline **1-Dy** in sealed polypropylene (PP) bags. For the PPMS VSM dc measurements, the sample was suspended in mineral oil (MPMS RSO dc: 40.2 mg **1-Dy** and 10.9 mg PP; PPMS VSM dc: 19.5 mg **1-Dy**, 18.3 mg PP, and 13.9 mg oil; MPMS ac and PPMS ACMS ac: 40.2 mg **1-Dy** and 10.9 mg PP; MPMS ac: 22.9 mg **1-Dy** and 9.46 mg PP); these samples were prepared in a glovebox under an atmosphere of argon. Data were collected as follows: (i) via an MPMS XL for dc measurements using the RSO option with fields up to 7 T and for ac measurements in the 0.001−1500 Hz range and (ii) via a PPMS EverCool II for dc measurements with the large bore VSM option with fields up to 9 T and for the ac measurements with the ACMS-II option in the 10−10,000 Hz range. The FC/ZFC measurements were performed from 50 K cooling to 1.85 K without dc field (reset magnet). The field (10 Oe) was set at 1.85 K, and ZFC measurements were recorded upon heating up to 50 K. FC cooling measurements were performed by cooling from 50 to 1.85 K, and FC heating data were collected upon heating from 1.85 to 50 K. During

https://doi.org/10.1021/jacs.3c12427
J. Am. Chem. Soc. 2024, 146, 3331−3342

the MPMS XL and PPMS EverCool II experiments, it is clear that the amplitude of the magnetization for **1-Dy** decreased slightly over a period of several weeks and more rapidly during sample transfer/loading in the experimental setup; we attribute this to a small amount of sample decomposition as **1-Dy** is relatively air- and moisture-sensitive and the PP bags are not completely impervious to air and moisture. However, no modification of the global, qualitative magnetic behavior was seen, with no shift or shape modification of the relaxation process. Therefore, the amplitude of the magnetic data presented herein was normalized to the MPMS3 measurements collected at Manchester directly after the synthesis and isolation of **1-Dy** in sealed borosilicate tubes. The maximum normalization factor used in this study was 1.19, which also incorporates errors in the sample mass, magnetometer calibration, and background corrections. Ac data for solid **1-Dy** were fitted with the generalized Debye model with MagSuite software, restraining the frequency window to where the model fits well.[68]

Computational Methods. OpenMolcas[50] was used to perform CASSCF-SO calculations on **1-Dy** to determine its electronic structure (Figures S108 and S109 and Table S11). The molecular geometry of the single-crystal XRD structure was used with no optimization, taking the largest disorder component only. Integrals were performed in the SEWAD module using basis sets from ANO-RCC library[69−72] with VTZP quality for Dy atoms, VDZP quality for the N atoms, and VDZ quality for all remaining atoms, employing the second-order DKH transformation. Cholesky decomposition of the two-electron integrals with a threshold of 10^{-8} was performed to save disk space and reduce computational demand. The molecular orbitals (MOs) were optimized in state-averaged CASSCF calculations in the RASSCF module, where the active space was defined by the nine 4f electrons in the seven 4f orbitals of Dy(III). Three such calculations were performed independently for each possible spin state, where 21 roots were included for $S = 5/2$, 224 roots were included for $S = 3/2$, and 490 roots were included for $S = 1/2$. The wave functions obtained from these CASSCF calculations were then mixed by spin−orbit coupling in the RASSI module, where all the 21 $S = 5/2$ states, 128 of the $S = 3/2$ states, and 130 of the $S = 1/2$ states were included. SINGLE_ANISO was used to decompose the resulting spin−orbit wave functions into the CF Hamiltonian formalism.[73] Diamond was employed for molecular graphics.[74]

DFT geometry optimizations and vibrational analyses were performed on the cation of **1-Y** and **2-Y**, the monomer of **3-Y**, and **4-Y**, for the purposes of assigning experimental IR spectra (Figures S57−S60). All calculations were executed by the Orca 5.0 software package at the PBE0[75,76]-D4[77,78]/def2-TZVP[79] level (including the default effective core potential for yttrium[80]). The default Orca 5.0 integration grids, convergence method, and convergence thresholds (for both SCF and geometry iterations) were used throughout. The SCF energy calculations were expedited by employing the RIJCOSX approximation[81] (and the associated def2/J auxiliary basis set[82]) and DIIS convergence acceleration[83] (as is default in Orca 5.0). Geometry-optimized structures were verified as being minima on the potential energy surface through the absence of imaginary vibrational modes. A linear energy scaling was applied to the computed IR spectra.

Synthesis. *[Y{N(Si^{i}Pr$_3$)$_2$}$_2$][Al{OC(CF$_3$)$_3$}$_4$] (**1-Y**).* C_6H_5F (5 mL) was added to a mixture of **4-Y** (0.168 g, 0.221 mmol) and $[CPh_3][Al\{OC(CF_3)_3\}_4]$ (0.242 g, 0.200 mmol), and the reaction mixture was stirred for 18 h at 20 °C. The resulting suspension was filtered and layered with excess *n*-hexane (*ca.* 20 mL), which upon diffusion at ambient temperature afforded the title compound as colorless needles. The crystals were isolated and dried thoroughly in vacuo. Yield: 0.251 g, 0.146 mmol, 73%. This reaction can also be performed in benzene with equivalent success, yielding under the same conditions a biphasic mixture comprising a benzene-clathrated oil of **1-Y** beneath a benzene solution of other reaction components. Anal. Calcd for $C_{52}H_{84}AlF_{36}O_4N_2Si_4Y$ (1713.42 g mol^{-1}) C, 36.45; H, 4.94, N, 1.63. Found: C, 34.38; H, 4.51, N, 1.41. ^{1}H NMR (400.07 MHz, C_6H_5F): δ 1.15 (d, $^3J_{HH}$ = 7.4 Hz, 72H, CH_3), 0.86 (sept, $^3J_{HH}$ = 7.4 Hz, 12H, CH). ^{13}C{^{1}H} DEPTQ NMR (100.60 MHz, C_6H_5F): δ 123.28 (q, $^1J_{FC}$ = 294 Hz, CF_3), 19.57 (s, CH_3), 18.25 (s, CH). ^{19}F NMR (376.40 MHz, C_6H_5F): δ −75.05 (s, CF_3). ^{29}Si{^{1}H} DEPT90 NMR (79.48 MHz, C_6H_5F): δ −4.79 (s, *Si*^{i}Pr$_3$). FTIR (ATR, microcrystalline): $\tilde{\nu}$ = 2945 (m), 2867 (m), 1465 (m), 1352 (m), 1296 (m), 1274 (m), 1241 (m), 1208 (s) 1167 (m), 968 (s), 953 (m), 920 (m), 880 (m), 725 (s) cm^{-1}.

*[Dy{N(Si^{i}Pr$_3$)$_2$}$_2$][Al{OC(CF$_3$)$_3$}$_4$] (**1-Dy**).* C_6H_5F (5 mL) was added to a mixture of **4-Dy** (0.350 g, 0.418 mmol) and $[CPh_3][Al\{OC(CF_3)_3\}_4]$ (0.484 g, 0.400 mmol), and the reaction mixture was stirred for 18 h at 20 °C. The resulting suspension was filtered and layered with excess *n*-hexane (*ca.* 20 mL), which upon diffusion at ambient temperature afforded the title compound as colorless needles. The crystals were isolated and dried thoroughly in vacuo. Yield: 0.567 g, 0.317 mmol, 79%. This reaction can also be performed in benzene with equivalent success, yielding under the same conditions a biphasic mixture comprising a benzene-clathrated oil of **1-Dy** beneath a benzene solution of the other reaction components. Anal. Calcd for $C_{52}H_{84}AlDyF_{36}O_4N_2Si_4$ (1786.91 g mol^{-1}) C, 34.95; H, 4.74, N, 1.57. Found: C, 33.66; H, 4.37, N, 1.41. χT product = 14.2 cm^3 mol^{-1} K, μ_{eff} = 10.7 μ_B mol^{-1} (Evans method). ^{1}H NMR (400.07 MHz, C_6D_6): δ 4.76 (br, fwhm ≈ 60 Hz), 4.23 (br, fwhm ≈ 50 Hz), 3.95 (br, fwhm ≈ 160 Hz), 3.67 (br, fwhm ≈ 60 Hz). ^{19}F NMR (376.40 MHz, C_6H_5F): δ 97.22 (br, fwhm ≈ 280 Hz, CF_3). FTIR (ATR, microcrystalline): $\tilde{\nu}$ = 2945 (m), 2867 (m), 1465 (m), 1352 (m), 1296 (m), 1274 (m), 1241 (m), 1208 (s) 1167 (m), 968 (s), 953 (m), 920 (m), 880 (m), 725 (s) cm^{-1}.

*[Y{N(Si^{i}Pr$_3$)$_2$}(BH$_4$)$_2$(THF)] (**2-Y**).* C_6H_5F (10 mL) was added to a mixture of $[Y(BH_4)_3(THF)_3]$ (2.389 g, 5.000 mmol) and $[K\{N(Si^iPr_3)_2\}]$ (1.857 g, 5.050 mmol), and the resulting suspension was stirred at 20 °C for 1 h. The volatiles were removed in vacuo, and the residues were extracted into *n*-hexane (3 × 20 mL) with vigorous agitation and filtered. The solution was concentrated to *ca.* 10 mL and stored at −25 °C, affording the title complex as colorless needles, which were isolated and thoroughly dried in vacuo. Yield: 2.298 g, 4.424 mmol, 88%. This reaction can also be successfully performed in benzene, following an otherwise identical procedure. Anal. Calcd for $C_{22}H_{58}B_2ONSi_2Y$ (519.35 g mol^{-1}) C, 50.87; H, 11.26, N, 2.70. Found: C, 49.55; H, 11.09, N, 2.45. ^{1}H NMR (400.07 MHz, C_6D_6, 298 K): δ 3.60 (br s, fwhm ≈ 19 Hz, 4H, CH_2CH_2O), 1.33 (d, $^3J_{HH}$ = 7.3 Hz, 36H, CH_3CH), 1.26 (q, 8H, $^1J_{BH}$ = 81 Hz, BH_4), 1.15 (sept, $^3J_{HH}$ = 7.3 Hz, 6H, CH_3CH), 1.06 (br s, fwhm ≈ 21 Hz, 4H, CH_2CH_2O). ^{11}B NMR (128.36 MHz, C_6D_6, 298 K): δ 22.0 (p, $^1J_{BH}$ = 81 Hz, BH_4). ^{13}C{^{1}H} DEPTQ NMR (100.60 MHz, C_6D_6, 298 K): δ 74.6 (CH_2CH_2O), 24.8 (CH_2CH_2O), 20.6 (CH_3CH), 18.4 (CH_3CH). ^{29}Si{^{1}H} DEPT90 NMR (79.48 MHz, C_6D_6, 298 K): δ −2.7 (*Si*^{i}Pr$_3$). FTIR (ATR, microcrystalline): $\tilde{\nu}$ = 2951 (m), 2867 (m), 2488 (m), 2178 (b), 1463 (m), 1185 (m), 1095 (w), 999 (m), 923 (s), 873 (s), 719 (s), 653 (s) cm^{-1}.

*[Dy{N(Si^{i}Pr$_3$)$_2$}(BH$_4$)$_2$(THF)] (**2-Dy**).* C_6H_5F (10 mL) (or benzene, see above) was added to a mixture of $[Dy(BH_4)_3(THF)_3]$ (2.757 g, 5.000 mmol) and $[K\{N(Si^iPr_3)_2\}]$ (1.857 g, 5.050 mmol), and the resulting suspension was stirred at 20 °C for 1 h. The volatiles were removed in vacuo, and the residues were extracted into *n*-hexane (3 × 20 mL) with vigorous agitation and filtered. The solution was concentrated to *ca.* 10 mL and stored at −25 °C, affording the title complex as pale-yellow needles, which were isolated and thoroughly dried in vacuo. Yield: 2.470 g, 4.165 mmol, 83%. This reaction can also be successfully performed in benzene, following an otherwise identical procedure. Anal. Calcd for $C_{22}H_{58}B_2DyONSi_2$ (592.94 g mol^{-1}) C, 44.56; H, 9.86, N, 2.36. Found: C, 43.86; H, 10.22, N, 2.84. χT product = 13.9 cm^3 mol^{-1} K, μ_{eff} = 10.5 μ_B mol^{-1} (Evans method). ^{1}H NMR (400.07 MHz, C_6D_6): δ 40.13 (vbr, fwhm ≈ 650 Hz, OCH_2CH_2), 1.55 (br, fwhm ≈ 20 Hz), 1.11 (br, fwhm ≈ 20 Hz, CH_3), 0.78 (br, fwhm ≈ 20 Hz), 0.63 (br, fwhm ≈ 20 Hz), −42.80 (vbr, fwhm ≈ 1610 Hz, OCH_2CH_2). The BH_4 resonance was not located. ^{11}B{^{1}H} NMR (128.36 MHz, C_6D_6): δ −18.14 (vbr, fwhm ≈ 2490 Hz), BH_4. FTIR (ATR, microcrystalline): $\tilde{\nu}$ = 2951 (m), 2867 (m), 2488 (m), 2178 (b), 1463 (m), 1185 (m), 1095 (w), 999 (m), 923 (s), 873 (s), 719 (s), 653 (s) cm^{-1}.

https://doi.org/10.1021/jacs.3c12427
J. Am. Chem. Soc. 2024, 146, 3331−3342

[Y{N(Si^{i}Pr$_3$)$_2$}(BH$_4$)(μ-BH$_4$)]$_4$ ***(3-Y)***. In a long resealable ampule, **2-Y** (4.290 g, 8.259 mmol) was heated to 120 °C in the solid state at *ca.* 0.01 mbar for 2 h, resulting in partial sublimation of the solid material. After cooling to ambient temperature, the residues were found to have a mass of 3.699 g (8.270 mmol assuming the formula weight of **3-Y**), consistent with the removal of 99.2% of the bound THF. The ^{1}H, ^{11}B, ^{13}C, and ^{29}Si NMR spectra of this amorphous material were found to be identical to an authentic crystalline sample of **3-Y**, which was prepared as follows. In a long resealable ampule, **2-Y** (1.390 g, 2.676 mmol) was heated to 150 °C in the solid state at *ca.* 0.01 mbar for 2 h, resulting in the partial sublimation of the solid material and minor production of a high-boiling point colorless oil. After cooling to ambient temperature, the residues were extracted into 1,2-C$_6$H$_4$F$_2$ (3 × 5 mL), filtered, and the solution concentrated to *ca.* 5 mL. Slow diffusion of excess *n*-hexane (*ca.* 20 mL) at −25 °C gave the title complex as colorless plates, which were isolated and thoroughly dried in vacuo. An additional crop was obtained upon storage at −25 °C after concentrating the fully diffused supernatant to *ca.* 5 mL. Yield: 0.641 g, 1.433 mmol, 54%. On one occasion, a sample of **3-Y** contaminated with trace KBH$_4$ was recrystallized by slow evaporation of benzene. Several crystals of **3-Y·0.5KBH$_4$·C$_6$H$_6$** were identified in the crop by single-crystal XRD, though as a homogeneous sample of the impurity was neither obtained nor sought, no further characterization data are reported. Characterization data for **3-Y**: Anal. Calcd for C$_{18}$H$_{50}$B$_2$NSi$_2$Y (447.25 g mol^{-1}) C, 48.33; H, 11.27, N, 3.13. Found: C, 45.67; H, 10.77, N, 2.81. ^{1}H NMR (400.07 MHz, C$_6$D$_6$): δ 1.13−1.07 (m, 50H, C*H*CH$_3$, CHC*H*$_3$ and B*H*$_4$). ^{11}B NMR (128.36 MHz, C$_6$D$_6$, 298 K): δ −20.7 (br., fwhm ≈ 480 Hz, *B*H$_4$), −3.6 (br., fwhm ≈ 2240 Hz, μ-*B*H$_4$). ^{13}C{^{1}H} DEPTQ NMR (100.60 MHz, C$_6$D$_6$): δ 19.3 (s, *C*H$_3$CH), 14.9 (s, CH$_3$*C*H). ^{29}Si{^{1}H} DEPT90 NMR (79.48 MHz, C$_6$D$_6$): δ −3.7 (s, *Si*^{i}Pr$_3$). ^{1}H NMR (400.07 MHz, C$_6$H$_4$F$_2$, C$_6$D$_6$): δ 1.13−1.00 (m, 50H, C*H*CH$_3$, CHC*H*$_3$ and B*H*$_4$). ^{11}B NMR (128.36 MHz, C$_6$H$_4$F$_2$, C$_6$D$_6$, 298 K): δ −20.9 (br. p, $^1J_{BH}$ ≈ 80 Hz, fwhm ≈ 120 Hz, *B*H$_4$). ^{13}C{^{1}H} DEPTQ NMR (100.60 MHz, C$_6$H$_4$F$_2$, C$_6$D$_6$): δ 18.8 (s, *C*H$_3$CH), 14.9 (s, CH$_3$*C*H). ^{29}Si{^{1}H} DEPT90 NMR (79.48 MHz, C$_6$H$_4$F$_2$, C$_6$D$_6$): δ −3.6 (s, *Si*^{i}Pr$_3$). FTIR (ATR, microcrystalline): $\tilde{\nu}$ = 2945 (m), 2865 (m), 2747 (w), 2519 (w), 2291 (m), 2178 (w), 2142 (w), 1467 (m), 1241 (s), 1194 (s), 908 (s), 873 (s), 715 (s), 655 (s) cm^{-1}.

[Dy{N(Si^{i}Pr$_3$)$_2$}(BH$_4$)(μ-BH$_4$)]$_4$ ***(3-Dy)***. In a long resealable ampule, **2-Dy** (0.3822 g, 0.6446 mmol) was heated to 120 °C in the solid state at *ca.* 0.01 mbar for 2 h, resulting in the partial sublimation of the solid material. After cooling to ambient temperature, the residues were found to have a mass of 0.3357 g (0.6446 mmol assuming the formula weight of **3-Dy**), consistent with the removal of 100% of the bound THF. The ^{1}H and ^{11}B NMR spectra of this amorphous material were found to be identical to that of an authentic crystalline sample of **3-Dy**, which was prepared as follows. In a long resealable ampule, **2-Dy** (1.770 g, 2.985 mmol) was heated to 150 °C in the solid state at *ca.* 0.01 mbar for 2 h, resulting in the partial sublimation of the solid material and minor production of a high-boiling point colorless oil. After cooling to ambient temperature, in a glovebox, the residues were returned to the base of the flask and the above procedure repeated. After cooling to ambient temperature, the residues were extracted into 1,2-C$_6$H$_4$F$_2$ (3 × 5 mL), filtered, and the solution was concentrated to *ca.* 5 mL. Slow diffusion of excess *n*-hexane (*ca.* 20 mL) at −25 °C afforded the title complex as pale-yellow plates, which were isolated and thoroughly dried in vacuo. An additional crop of the title complex was obtained upon storage at −25 °C after concentrating the fully diffused supernatant to *ca.* 5 mL. Yield: 1.067 g, 2.049 mmol, 67%. As described for **3-Y**, trace KBH$_4$ contamination led to the formation of several crystals of **3-Dy·0.5KBH$_4$·C$_6$H$_4$F$_2$-1,2** following recrystallization from 1,2-C$_6$H$_4$F$_2$ layered with hexane. This complex was characterized by single-crystal XRD only. Characterization data for **3-Dy**: Anal. Calcd for C$_{18}$H$_{50}$B$_2$DyNSi$_2$ (520.84 g mol^{-1}) C, 41.50; H, 9.67, N, 2.69. Found: C, 39.55; H, 9.81, N, 2.55. χT product = 12.5 cm^3 mol^{-1} K, μ_{eff} = 10.0 μ_B mol^{-1} (Evans method). ^{1}H NMR (400.07 MHz, C$_6$D$_6$): δ 1.71 (br, fwhm ≈ 20 Hz, C*H*$_3$), 1.25 (br, fwhm ≈ 30 Hz), 0.34 (br, fwhm ≈ 30 Hz). ^{11}B{^{1}H} NMR (128.36 MHz, C$_6$D$_6$): δ −9.94 (vbr, fwhm ≈ 2450 Hz, B*H*$_4$). FTIR (ATR, microcrystalline): $\tilde{\nu}$ = 2947 (m), 2867 (m), 2751 (w), 2517 (w), 2287 (m), 2166 (w), 2143 (w), 1467 (m), 1208 (s), 1189 (s), 904 (s), 873 (s), 715 (s), 656 (s) cm^{-1}.

[Y{N(Si^{i}Pr$_3$)$_2$}$_2$(BH$_4$)] ***(4-Y)***. A solution of **3-Y** (0.447 g, 1.000 mmol) and [K{N(Si^{i}Pr$_3$)$_2$}] (0.734 g, 2.000 mmol) in benzene (10 mL) was stirred at 30 °C for 72 h. The volatiles were then removed in vacuo and the residues extracted into *n*-hexane and filtered. The volatiles were again removed in vacuo, and [HNEt$_3$][Al{OC(CF$_3$)$_3$}$_4$] (0.535 g, 0.500 mmol) was added followed by benzene (10 mL). The resulting suspension was vigorously stirred for 4 h at 20 °C, after which the volatiles were removed in vacuo, and the residues were extracted into HMDSO (3 × 1 mL) and filtered. Storage of the solution at −35 °C afforded the title compound as colorless blocks, which were isolated and thoroughly dried in vacuo. Yield: 0.178 g, 0.234 mmol, 23% with respect to **3-Y**. Anal. Calcd for C$_{36}$H$_{88}$BN$_2$Si$_4$Y (761.08 g mol^{-1}) C, 56.81; H, 11.65, N, 3.68. Found: C, 51.98; H, 11.17; N, 2.12. ^{1}H NMR (400.07 MHz, C$_6$D$_6$): δ 1.47 (qd, $^1J_{BH}$ = 72 Hz, $^1J_{YH}$ = 14 Hz, 4H, B*H*$_4$), 1.35 (d, $^3J_{HH}$ = 7.4 Hz, 72H, C*H*$_3$), 1.06 (sept, $^3J_{HH}$ = 7.5 Hz, 12H, C*H*). ^{11}B NMR (128.36 MHz, C$_6$D$_6$): δ −21.41 (p, $^1J_{BH}$ = 86 Hz, *B*H$_4$). ^{13}C{^{1}H} DEPTQ NMR (100.60 MHz, C$_6$D$_6$): δ 21.0 (s, *C*H$_3$CH), 19.8 (s, CH$_3$*C*H). ^{29}Si{^{1}H} DEPT90 NMR (79.48 MHz, C$_6$D$_6$): δ −3.36 (s, *Si*^{i}Pr$_3$). FTIR (ATR, microcrystalline): $\tilde{\nu}$ = 2943 (s), 2864 (s), 2756 (w), 2731 (w), 2495 (w), 2229 (br), 1463 (m), 1241 (s), 1216 (s), 941 (s), 879 (s), 698 (s), 658 (s) cm^{-1}.

[Dy{N(Si^{i}Pr$_3$)$_2$}$_2$(BH$_4$)] ***(4-Dy)***. A solution of **3-Dy** (0.520 g, 1.000 mmol) and [K{N(Si^{i}Pr$_3$)$_2$}] (0.734 g, 2.000 mmol) in benzene (10 mL) was stirred at 30 °C for 72 h. The volatiles were then removed in vacuo and the residues extracted into *n*-hexane and filtered. The volatiles were again removed in vacuo, and [HNEt$_3$][Al{OC(CF$_3$)$_3$}$_4$] (0.535 g, 0.500 mmol) was added followed by benzene (10 mL). The resulting suspension was vigorously stirred for 4 h at 20 °C, after which the volatiles were removed in vacuo and the residues extracted into HMDSO (3 × 1 mL) and filtered. Storage of the solution at −35 °C afforded the title compound as colorless blocks, which were isolated and thoroughly dried in vacuo. Yield: 0.089 g, 0.117 mmol, 12% with respect to **3-Dy**. Anal. Calcd for C$_{36}$H$_{88}$BDyN$_2$Si$_4$ (834.67 g mol^{-1}) C, 51.80; H, 10.63, N, 3.36. Found: C, 49.16; H, 10.73; N, 2.97. χT product = 12.6 cm^3 mol^{-1} K, μ_{eff} = 10.1 μ_B mol^{-1} (Evans method). ^{1}H NMR (400.07 MHz, C$_6$D$_6$): δ 1.35 (br, fwhm ≈ 25 Hz), 0.62 (br, fwhm ≈ 18 Hz). ^{11}B{^{1}H} NMR (128.36 MHz, C$_6$D$_6$): δ −14.1 (vbr, fwhm ≈ 1690 Hz, *B*H$_4$). FTIR (ATR, microcrystalline): $\tilde{\nu}$ = 2943 (s), 2864 (s), 2753 (w), 2727 (w), 2488 (w), 2240 (br), 1463 (m), 1239 (s), 1212 (s), 939 (s), 879 (s), 698 (s), 659 (s) cm^{-1}.

[Y{N(Si^{i}Pr$_3$)$_2$}{N(Si^{i}Pr$_3$)[Si(^{i}Pr)$_2${CH(Me)CH$_2$}]-κ^2-N,C}] ***(5-Y)***. The HMDSO-insoluble residues (250 mg), obtained from the synthesis of **3-Y** similar to that outlined above and found by ^{1}H NMR spectroscopy to contain 11.3 mol % **1-Y** (42.4 mg, 0.0247 mmol) and 88.7 mol % [HNEt$_3$][Al{OC(CF$_3$)$_3$}$_4$] (207.6 mg, 0.194 mmol), were combined with [K{N(Si^{i}Pr$_3$)$_2$}] (150 mg, 0.408 mmol) and the mixture suspended in benzene (5 mL). After stirring at ambient temperature for 1 h, the volatiles were removed in vacuo and the residues extracted into hexane. The volatiles were again removed in vacuo, and a portion of the resulting colorless oil containing a mixture of the title compound and HN(Si^{i}Pr$_3$)$_2$ was analyzed in C$_6$D$_6$ solution by NMR spectroscopy. ^{1}H NMR (400.07 MHz, C$_6$D$_6$): 1.67 (d, $^3J_{HH}$ = 6.2 Hz, 3H, Si^{i}Pr$_2$CH(C*H*$_3$)CH$_2$Y), 1.45 (d, $^3J_{HH}$ = 6.9 Hz, 3H, Si^{i}Pr$_2$CH(CH$_3$)CH$_2$Y), 1.43 (d, $^3J_{HH}$ = 6.5 Hz, 3H, Si^{i}Pr$_2$CH(CH$_3$)-CH$_2$Y), 1.38−1.32 (m, 9H, C*H*$_3$), 1.30−1.25 (m, 54H, C*H*$_3$), 1.12−1.02 (obsc. m, 9H, C*H*), 1.00−0.90 (m, 3H, C*H*). ^{13}C{^{1}H} DEPTQ NMR (100.60 MHz, C$_6$D$_6$, selected signals): δ 55.34 (d, $^1J_{YC}$ = 47.4 Hz, Si^{i}Pr$_2$CH(CH$_3$)CH$_2$Y), 24.50 (s, Si^{i}Pr$_2$CH(CH$_3$)CH$_2$Y), 21.79 (s, Si^{i}Pr$_2$CH(CH$_3$)CH$_2$Y), 20.69 (s, Si^{i}Pr$_2$CH(CH$_3$)CH$_2$Y). ^{29}Si{^{1}H} DEPT90 NMR (79.48 MHz, C$_6$D$_6$): δ, −3.32 (s, ^{i}Pr$_3$*Si*NSi^{i}Pr$_2$CH-(CH$_3$)CH$_2$), −5.75 (s, ^{i}Pr$_3$*Si*NS*i*^{i}Pr$_3$), −7.62 (s, ^{i}Pr$_3$SiNS*i*^{i}Pr$_2$CH-(CH$_3$)CH$_2$).

https://doi.org/10.1021/jacs.3c12427
J. Am. Chem. Soc. 2024, 146, 3331−3342

■ ASSOCIATED CONTENT

Data Availability Statement

Research data files supporting this publication are available from FigShare at https://figshare.com/doi/10.6084/m9.figshare.23807376.

Supporting Information

The Supporting Information is available free of charge at https://pubs.acs.org/doi/10.1021/jacs.3c12427.

Additional experimental details, materials, methods, and associated data (PDF)

Accession Codes

CCDC 2284722−2284732 contain the supplementary crystallographic data for this paper. These data can be obtained free of charge via www.ccdc.cam.ac.uk/data_request/cif, or by emailing data_request@ccdc.cam.ac.uk, or by contacting The Cambridge Crystallographic Data Centre, 12 Union Road, Cambridge, CB2 1EZ, UK; fax: +44 1223 336033.

■ AUTHOR INFORMATION

Corresponding Authors

Rodolphe Clérac − *Univ. Bordeaux, CNRS, CRPP, 33600 Pessac, France;* orcid.org/0000-0001-5429-7418; Email: rodolphe.clerac@u-bordeaux.fr

Nicholas F. Chilton − *Department of Chemistry, The University of Manchester, Manchester M13 9PL, U.K.; Research School of Chemistry, The Australian National University, Canberra, ACT 2601, Australia;* orcid.org/0000-0002-8604-0171; Email: nicholas.chilton@anu.edu.au

David P. Mills − *Department of Chemistry, The University of Manchester, Manchester M13 9PL, U.K.;* orcid.org/0000-0003-1575-7754; Email: david.mills@manchester.ac.uk

Authors

Jack Emerson-King − *Department of Chemistry, The University of Manchester, Manchester M13 9PL, U.K.;* orcid.org/0000-0002-0309-8344

Gemma K. Gransbury − *Department of Chemistry, The University of Manchester, Manchester M13 9PL, U.K.;* orcid.org/0000-0002-7579-4226

George F. S. Whitehead − *Department of Chemistry, The University of Manchester, Manchester M13 9PL, U.K.;* orcid.org/0000-0003-1949-4250

Iñigo J. Vitorica-Yrezabal − *Department of Chemistry, The University of Manchester, Manchester M13 9PL, U.K.*

Mathieu Rouzières − *Univ. Bordeaux, CNRS, CRPP, 33600 Pessac, France*

Complete contact information is available at: https://pubs.acs.org/10.1021/jacs.3c12427

Notes

The authors declare no competing financial interest.

■ ACKNOWLEDGMENTS

We thank the University of Manchester for access to the Computational Shared Facility and the European Research Council (StG-851504 and CoG-816268) and the UK EPSRC (EP/R002605X/1, EP/P001386/1, EP/S033181/1 and EP/T011289/1) for funding. We acknowledge the EPSRC UK National Electron Paramagnetic Resonance Service for access to the SQUID magnetometer and the National Nuclear User Facility at the Center for Radiochemical Research for access to a diffractometer. R.C. and M.R. thank the University of Bordeaux, the CNRS, the Region Nouvelle Aquitaine, and Quantum Matter Bordeaux. N.F.C. thanks the Royal Society for a University Research Fellowship (URF191320).

■ REFERENCES

(1) Giansiracusa, M. J.; Gransbury, G. K.; Chilton, N. F.; Mills, D. P. Single-Molecule Magnets. In *Encyclopedia of Inorganic and Bioinorganic Chemistry*; Scott, R. A., Ed.; John Wiley: Chichester, 2021, .
(2) Chilton, N. F. Molecular Magnetism. *Annu. Rev. Mater. Res.* **2022**, *52*, 79−101.
(3) Gatteschi, D.; Sessoli, R.; Villain, J. *Molecular Nanomagnets*; Oxford University Press: Oxford, 2006,.
(4) Ishikawa, N.; Sugita, M.; Ishikawa, T.; Koshihara, S. Y.; Kaizu, Y. Lanthanide Double-Decker Complexes Functioning as Magnets at the Single-Molecular Level. *J. Am. Chem. Soc.* **2003**, *125* (29), 8694−8695.
(5) Layfield, R. A.; Murugesu, M. *Lanthanides and Actinides in Molecular Magnetism*; Wiley: Hoboken, 2015, .
(6) Liddle, S. T.; Van Slageren, J. Improving f-Element Single Molecule Magnets. *Chem. Soc. Rev.* **2015**, *44* (19), 6655−6669.
(7) Liu, J.-L.; Chen, Y.-C.; Tong, M.-L. Symmetry Strategies for High Performance Lanthanide-Based Single-Molecule Magnets. *Chem. Soc. Rev.* **2018**, *47* (7), 2431−2453.
(8) Rinehart, J. D.; Long, J. R. Exploiting Single-Ion Anisotropy in the Design of f-Element Single-Molecule Magnets. *Chem. Sci.* **2011**, *2* (11), 2078−2085.
(9) Ungur, L.; Chibotaru, L. F. Magnetic Anisotropy in the Excited States of Low Symmetry Lanthanide Complexes. *Phys. Chem. Chem. Phys.* **2011**, *13* (45), 20086−20090.
(10) Ungur, L.; Chibotaru, L. F. Strategies toward High-Temperature Lanthanide-Based Single-Molecule Magnets. *Inorg. Chem.* **2016**, *55* (20), 10043−10056.
(11) Parmar, V. S.; Mills, D. P.; Winpenny, R. E. P. Mononuclear Dysprosium Alkoxide and Aryloxide Single-Molecule Magnets. *Chem.-Eur. J.* **2021**, *27* (28), 7625−7645.
(12) Goodwin, C. A. P.; Ortu, F.; Reta, D.; Chilton, N. F.; Mills, D. P. Molecular Magnetic Hysteresis at 60 kelvin in Dysprosocenium. *Nature* **2017**, *548* (7668), 439−442.
(13) Randall McClain, K.; Gould, C. A.; Chakarawet, K.; Teat, S. J.; Groshens, T. J.; Long, J. R.; Harvey, B. G. High-Temperature Magnetic Blocking and Magneto-Structural Correlations in a Series of Dysprosium(III) Metallocenium Single-Molecule Magnets. *Chem. Sci.* **2018**, *9* (45), 8492−8503.
(14) Guo, F.-S.; Day, B. M.; Chen, Y. C.; Tong, M. L.; Mansikkamäki, A.; Layfield, R. A. Magnetic Hysteresis up to 80 kelvin in a Dysprosium Metallocene Single-molecule Magnet. *Science* **2018**, *362* (6421), 1400−1403.
(15) Guo, F.-S.; Day, B. M.; Chen, Y.-C.; Tong, M.-L.; Mansikkamäki, A.; Layfield, R. A. A Dysprosium Metallocene Single-Molecule Magnet Functioning at the Axial Limit. *Angew. Chem., Int. Ed.* **2017**, *56* (38), 11445−11449.
(16) Guo, F.-S.; Day, B. M.; Chen, Y.-C.; Tong, M.-L.; Mansikkamäki, A.; Layfield, R. A. Corrigendum: A Dysprosium Metallocene Single-Molecule Magnet Functioning at the Axial Limit. *Angew. Chem., Int. Ed.* **2020**, *59* (43), 18844.
(17) Evans, P.; Reta, D.; Whitehead, G. F. S.; Chilton, N. F.; Mills, D. P. Bis-Monophospholyl Dysprosium Cation Showing Magnetic Hysteresis at 48 K. *J. Am. Chem. Soc.* **2019**, *141* (50), 19935−19940.
(18) Gould, C. A.; McClain, K. R.; Yu, J. M.; Groshens, T. J.; Furche, F.; Harvey, B. G.; Long, J. R. Synthesis and Magnetism of Neutral, Linear Metallocene Complexes of Terbium(II) and Dysprosium(II). *J. Am. Chem. Soc.* **2019**, *141* (33), 12967−12973.
(19) Gould, C. A.; McClain, K. R.; Reta, D.; Kragskow, J. G. C.; Marchiori, D. A.; Lachman, E.; Choi, E.-S.; Analytis, J. G.; Britt, R. D.; Chilton, N. F.; Harvey, B. G.; Long, J. R. Ultrahard Magnetism from

Mixed-Valence Dilanthanide Complexes with Metal-Metal Bonding. *Science* **2022**, *375* (6577), 198−202.
(20) Guo, F. S.; He, M.; Huang, G. Z.; Giblin, S. R.; Billington, D.; Heinemann, F. W.; Tong, M. L.; Mansikkamäki, A.; Layfield, R. A. Discovery of a Dysprosium Metallocene Single-Molecule Magnet with Two High-Temperature Orbach Processes. *Inorg. Chem.* **2022**, *61* (16), 6017−6025.
(21) Vanjak, J. C.; Wilkins, B. O.; Vieru, V.; Bhuvanesh, N. S.; Reibenspies, J. H.; Martin, C. D.; Chibotaru, L. F.; Nippe, M. A High-Performance Single-Molecule Magnet Utilizing Dianionic Aminoborolide Ligands. *J. Am. Chem. Soc.* **2022**, *144* (39), 17743−17747.
(22) Vincent, A. H.; Whyatt, Y. L.; Chilton, N. F.; Long, J. R. Strong Axiality in a Dysprosium(III) Bis(Borolide) Complex Leads to Magnetic Blocking at 65 K. *J. Am. Chem. Soc.* **2023**, *145* (3), 1572−1579.
(23) Reta, D.; Kragskow, J. G. C.; Chilton, N. F. Ab Initio Prediction of High-Temperature Magnetic Relaxation Rates in Single-Molecule Magnets. *J. Am. Chem. Soc.* **2021**, *143* (15), 5943−5950.
(24) Chilton, N. F.; Goodwin, C. A. P.; Mills, D. P.; Winpenny, R. E. P. The First Near-Linear Bis(Amide) f-Block Complex: A Blueprint for a High Temperature Single Molecule Magnet. *Chem. Commun.* **2015**, *51*, 101−103.
(25) Goodwin, C. A. P.; Chilton, N. F.; Vettese, G. F.; Moreno Pineda, E.; Crowe, I. F.; Ziller, J. W.; Winpenny, R. E. P.; Evans, W. J.; Mills, D. P. Physicochemical Properties of Near-Linear Lanthanide(II) Bis(Silylamide) Complexes (Ln = Sm, Eu, Tm, Yb). *Inorg. Chem.* **2016**, *55* (20), 10057−10067.
(26) Blagg, R. J.; Ungur, L.; Tuna, F.; Speak, J.; Comar, P.; Collison, D.; Wernsdorfer, W.; McInnes, E. J. L.; Chibotaru, L. F.; Winpenny, R. E. P. Magnetic Relaxation Pathways in Lanthanide Single-Molecule Magnets. *Nat. Chem.* **2013**, *5* (8), 673−678.
(27) Chilton, N. F. Design Criteria for High-Temperature Single-Molecule Magnets. *Inorg. Chem.* **2015**, *54* (5), 2097−2099.
(28) Nicholas, H. M.; Vonci, M.; Goodwin, C. A. P.; Loo, S. W.; Murphy, S. R.; Cassim, D.; Winpenny, R. E. P.; McInnes, E. J. L.; Chilton, N. F.; Mills, D. P. Electronic Structures of Bent Lanthanide(III) Complexes with Two N-Donor Ligands. *Chem. Sci.* **2019**, *10* (45), 10493−10502.
(29) Goodwin, C. A. P.; Réant, B. L. L.; Kragskow, J. G. C.; DiMucci, I. M.; Lancaster, K. M.; Mills, D. P.; Sproules, S. Heteroleptic Samarium(III) Halide Complexes Probed by Fluorescence-Detected L_3-Edge X-Ray Absorption Spectroscopy. *Dalton Trans.* **2018**, *47* (31), 10613−10625.
(30) Errulat, D.; Harriman, K. L. M.; Gálico, D. A.; Kitos, A. A.; Mansikkamäki, A.; Murugesu, M. A Trivalent 4f Complex with Two Bis-Silylamide Ligands Displaying Slow Magnetic Relaxation. *Nat. Chem.* **2023**, *15*, 1100−1107.
(31) Atwood, D. A., Ed. In *The Rare Earth Elements: Fundamentals and Applications*; John Wiley & Sons Ltd: Chichester, 2012.
(32) Ortu, F.; Mills, D. P. Low-Coordinate Rare-Earth and Actinide Complexes Bünzli, J.-C. G., Pecharsky, V. K., Eds.; *Handbook on the Physics and Chemistry of Rare Earths*; Elsevier B. V.: Amsterdam, 2019; Vol. *55*, pp 1−87, .
(33) Yang, K.; Sun, R.; Zhao, J.; Deng, C.; Wang, B.; Gao, S.; Huang, W. A Combined Synthetic, Magnetic, and Theoretical Study on Enhancing Ligand-Field Axiality for Dy(III) Single-Molecule Magnets Supported by Ferrocene Diamide Ligands. *Inorg. Chem.* **2023**, *62* (25), 9892−9903.
(34) Goodwin, C. A. P.; Reta, D.; Ortu, F.; Liu, J.; Chilton, N. F.; Mills, D. P. Terbocenium: Completing a Heavy Lanthanide Metallocenium Cation Family with an Alternative Anion Abstraction Strategy. *Chem. Commun.* **2018**, *54* (66), 9182−9185.
(35) Krossing, I.; Brands, H.; Feuerhake, R.; Koenig, S. New Reagents to Introduce Weakly Coordinating Anions of Type $Al(ORF)_4^-$: Synthesis, Structure and Characterization of Cs and Trityl Salts. *J. Fluorine Chem.* **2001**, *112*, 83−90.
(36) Sur, S. K. Measurement of Magnetic Susceptibility and Magnetic Moment of Paramagnetic Molecules in Solution by High-Field Fourier Transform NMR Spectroscopy. *J. Magn. Reson.* **1989**, *82*, 169−173.
(37) Kahn, O. *Molecular Magnetism*; VCH-Verlag: Weinheim, 1993.
(38) Niemeyer, M. Reactions of Hypersilyl Potassium with Rare-Earth Metal Bis(Trimethylsilylamides): Addition versus Peripheral Deprotonation. *Inorg. Chem.* **2006**, *45* (22), 9085−9095.
(39) Marks, T. J.; Kolb, J. R. Covalent Transition Metal, Lanthanide, and Actinide Tetrahydroborate Complexes. *Chem. Rev.* **1977**, *77* (2), 263−293.
(40) Shannon, R. D. Revised Effective Ionic Radii and Systematic Studies of Interatomic Distances in Halides and Chalcogenides. *Acta Crystallogr., Sect. A* **1976**, *32* (5), 751−767.
(41) Gransbury, G. K.; Corner, S. C.; Kragskow, J. G. C.; Evans, P.; Yeung, H. M.; Blackmore, W. J. A.; Whitehead, G. F. S.; Vitorica-Yrezabal, I. J.; Oakley, M. S.; Chilton, N. F.; Mills, D. P. AtomAccess: A Predictive Tool for Molecular Design and Its Application to the Targeted Synthesis of Dysprosium Single-Molecule Magnets. *J. Am. Chem. Soc.* **2023**, *145* (41), 22814−22825.
(42) van Vleck, J. H. Paramagnetic Relaxation Times for Titanium and Chrome Alum. *Phys. Rev.* **1940**, *57* (5), 426−447.
(43) Shrivastava, K. N. Theory of Spin-Lattice Relaxation. *Phys. Status Solidi B* **1983**, *117* (2), 437−458.
(44) Reta, D.; Chilton, N. F. Uncertainty Estimates for Magnetic Relaxation Times and Magnetic Relaxation Parameters. *Phys. Chem. Chem. Phys.* **2019**, *21* (42), 23567−23575.
(45) Blackmore, W. J. A.; Gransbury, G. K.; Evans, P.; Kragskow, J. G. C.; Mills, D. P.; Chilton, N. F. Characterisation of Magnetic Relaxation on Extremely Long Timescales. *Phys. Chem. Chem. Phys.* **2023**, *25*, 16735−16744.
(46) Ding, Y. S.; Blackmore, W. J. A.; Zhai, Y. Q.; Giansiracusa, M. J.; Reta, D.; Vitorica-Yrezabal, I.; Winpenny, R. E. P.; Chilton, N. F.; Zheng, Y. Z. Studies of the Temperature Dependence of the Structure and Magnetism of a Hexagonal-Bipyramidal Dysprosium(III) Single-Molecule Magnet. *Inorg. Chem.* **2022**, *61* (1), 227−235.
(47) Ding, Y. S.; Yu, K. X.; Reta, D.; Ortu, F.; Winpenny, R. E. P.; Zheng, Y. Z.; Chilton, N. F. Field- and Temperature-Dependent Quantum Tunnelling of the Magnetisation in a Large Barrier Single-Molecule Magnet. *Nat. Commun.* **2018**, *9*, 3134.
(48) Chiesa, A.; Cugini, F.; Hussain, R.; MacAluso, E.; Allodi, G.; Garlatti, E.; Giansiracusa, M.; Goodwin, C. A. P.; Ortu, F.; Reta, D.; Skelton, J. M.; Guidi, T.; Santini, P.; Solzi, M.; De Renzi, R.; Mills, D. P.; Chilton, N. F.; Carretta, S. Understanding Magnetic Relaxation in Single-Ion Magnets with High Blocking Temperature. *Phys. Rev. B* **2020**, *101*, 174402.
(49) Abragam, A.; Bleaney, B. *Electron Paramagnetic Resonance of Transition Ions*; Oxford University Press: Oxford, 1970.
(50) Orbach, R. Spin-lattice relaxation in rare-earth salts. *Proc. R. Soc. London, Ser. A* **1961**, *264* (1319), 458−484.
(51) Topping, C. V.; Blundell, S. J. A.C. Susceptibility as a Probe of Low-Frequency Magnetic Dynamics. *J. Phys.: Condens. Matter* **2019**, *31* (1), 013001.
(52) Fdez Galván, I.; Vacher, M.; Alavi, A.; Angeli, C.; Aquilante, F.; Autschbach, J.; Bao, J. J.; Bokarev, S. I.; Bogdanov, N. A.; Carlson, R. K.; Chibotaru, L. F.; Creutzberg, J.; Dattani, N.; Delcey, M. G.; Dong, S. S.; Dreuw, A.; Freitag, L.; Frutos, L. M.; Gagliardi, L.; Gendron, F.; Giussani, A.; González, L.; Grell, G.; Guo, M.; Hoyer, C. E.; Johansson, M.; Keller, S.; Knecht, S.; Kovačević, G.; Källman, E.; Li Manni, G.; Lundberg, M.; Ma, Y.; Mai, S.; Malhado, J. P.; Malmqvist, P. Å.; Marquetand, P.; Mewes, S. A.; Norell, J.; Olivucci, M.; Oppel, M.; Phung, Q. M.; Pierloot, K.; Plasser, F.; Reiher, M.; Sand, A. M.; Schapiro, I.; Sharma, P.; Stein, C. J.; Sørensen, L. K.; Truhlar, D. G.; Ugandi, M.; Ungur, L.; Valentini, A.; Vancoillie, S.; Veryazov, V.; Weser, O.; Wesołowski, T. A.; Widmark, P. O.; Wouters, S.; Zech, A.; Zobel, J. P.; Lindh, R. OpenMolcas: From Source Code to Insight. *J. Chem. Theory Comput.* **2019**, *15* (11), 5925−5964.
(53) Scheschkewitz, D., Ed.; *Functional Molecular Silicon Compounds II*; Structure and Bonding; Springer International Publishing: Cham, 2014; Vol. *156*, .

https://doi.org/10.1021/jacs.3c12427
J. Am. Chem. Soc. 2024, 146, 3331−3342

(54) Goodwin, C. A. P.; Mills, D. P. Silylamides: Towards a Half-Century of Stabilising Remarkable f-Element Chemistry Fairlamb, I. J. S., Lynam, J., Patmore, N. J., Elliott, P., Eds.; *Specialist Periodical Reports: Organometallic Chemistry*; RSC Publishing: Cambridge, 2017; Vol. *41*, pp 123−156, .
(55) Kragskow, J. G. C.; Mattioni, A.; Staab, J. K.; Reta, D.; Skelton, J. M.; Chilton, N. F. Spin-Phonon Coupling and Magnetic Relaxation in Single-Molecule Magnets. *Chem. Soc. Rev.* **2023**, *52*, 4567−4585.
(56) Nabi, R.; Staab, J. K.; Mattioni, A.; Kragskow, J. G. C.; Reta, D.; Skelton, J. M.; Chilton, N. F. Accurate and Efficient Spin-Phonon Coupling and Spin Dynamics Calculations for Molecular Solids. *J. Am. Chem. Soc.* **2023**, *145* (45), 24558−24567.
(57) Ortu, F.; Reta, D.; Ding, Y. S.; Goodwin, C. A. P.; Gregson, M. P.; McInnes, E. J. L.; Winpenny, R. E. P.; Zheng, Y. Z.; Liddle, S. T.; Mills, D. P.; Chilton, N. F. Studies of Hysteresis and Quantum Tunnelling of the Magnetisation in Dysprosium(III) Single Molecule Magnets. *Dalton Trans.* **2019**, *48* (24), 8541−8545.
(58) Fulmer, G. R.; Miller, A. J. M.; Sherden, N. H.; Gottlieb, H. E.; Nudelman, A.; Stoltz, B. M.; Bercaw, J. E.; Goldberg, K. I. NMR Chemical Shifts of Trace Impurities: Common Laboratory Solvents, Organics, and Gases in Deuterated Solvents Relevant to the Organometallic Chemist. *Organometallics* **2010**, *29* (9), 2176−2179.
(59) *CrysAlis PRO*; Agilent Technologies Ltd. Yarnton, England, 2014.
(60) Sheldrick, G. M. SHELXT - Integrated Space-Group and Crystal-Structure Determination. *Acta Crystallogr., Sect. A* **2015**, *71*, 3−8.
(61) Sheldrick, G. M. Crystal Structure Refinement with SHELXL. *Acta Crystallogr., Sect. C* **2015**, *71*, 3−8.
(62) Dolomanov, O. V.; Bourhis, L. J.; Gildea, R. J.; Howard, J. A. K.; Puschmann, H. OLEX2: A Complete Structure Solution, Refinement and Analysis Program. *J. Appl. Crystallogr.* **2009**, *42* (2), 339−341.
(63) Farrugia, L. J. WinGX and ORTEP for Windows: An Update. *J. Appl. Crystallogr.* **2012**, *45* (4), 849−854.
(64) *Persistence of Vision Raytracer, v.3.7*, Persistence of Vision Raytracer Pty. Ltd., 2013. http://www.povray.org/download/(accessed 10−03−2023).
(65) Kabova, E. A.; Blundell, C. D.; Muryn, C. A.; Whitehead, G. F. S.; Vitorica-Yrezabal, I. J.; Ross, M. J.; Shankland, K. SDPD-SX: Combining a Single Crystal X-Ray Diffraction Setup with Advanced Powder Data Structure Determination for Use in Early Stage Drug Discovery. *CrystEngComm* **2022**, *24*, 4337−4340.
(66) Bain, G. A.; Berry, J. F. Diamagnetic Corrections and Pascal's Constants. *J. Chem. Educ.* **2008**, *85* (4), 532.
(67) Reta, D.; Kragskow, J. G. C.; Chilton, N. F. *CC-FIT2. v.5.0.1*. https://gitlab.com/chilton-group/cc-fit2 (accessed 06−22-2023).
(68) *MagSuite v.3.2*. Rouzières, M., Zenodo, 2023, .
(69) Roos, B. O.; Veryazov, V.; Widmark, P.-O. Relativistic Atomic Natural Orbital Type Basis Sets for the Alkaline and Alkaline-Earth Atoms Applied to the Ground-State Potentials for the Corresponding Dimers. *Theor. Chem. Acc.* **2004**, *111* (2−6), 345−351.
(70) Roos, B. O.; Lindh, R.; Malmqvist, P. Å.; Veryazov, V.; Widmark, P. O. Main Group Atoms and Dimers Studied with a New Relativistic ANO Basis Set. *J. Phys. Chem. A* **2004**, *108* (15), 2851−2858.
(71) Roos, B. O.; Lindh, R.; Malmqvist, P.-Å.; Veryazov, V.; Widmark, P.-O. New Relativistic ANO Basis Sets for Transition Metal Atoms. *J. Phys. Chem. A* **2005**, *109* (29), 6575−6579.
(72) Roos, B. O.; Lindh, R.; Malmqvist, P.-Å.; Veryazov, V.; Widmark, P.-O.; Borin, A. C. New Relativistic Atomic Natural Orbital Basis Sets for Lanthanide Atoms with Applications to the Ce Diatom and LuF_3. *J. Phys. Chem. A* **2008**, *112* (45), 11431−11435.
(73) Chibotaru, L. F.; Ungur, L. Ab Initio Calculation of Anisotropic Magnetic Properties of Complexes. I. Unique Definition of Pseudospin Hamiltonians and Their Derivation. *J. Chem. Phys.* **2012**, *137* (6), 064112.
(74) *Diamond − Crystal and Molecular Structure Visualization; Crystal Impact v.4.6.8*. Putz, H.; Brandenburg, H., Bonn, Germany, 2022.
(75) Adamo, C.; Barone, V. Toward Reliable Density Functional Methods without Adjustable Parameters: The PBE0Model. *J. Chem. Phys.* **1999**, *110* (13), 6158−6170.
(76) Perdew, J. P.; Ernzerhof, M.; Burke, K. Rationale for Mixing Exact Exchange with Density Functional Approximations. *J. Chem. Phys.* **1996**, *105* (22), 9982−9985.
(77) Caldeweyher, E.; Bannwarth, C.; Grimme, S. Extension of the D3 Dispersion Coefficient Model. *J. Chem. Phys.* **2017**, *147* (3), 034112.
(78) Caldeweyher, E.; Ehlert, S.; Hansen, A.; Neugebauer, H.; Spicher, S.; Bannwarth, C.; Grimme, S. A Generally Applicable Atomic-Charge Dependent London Dispersion Correction. *J. Chem. Phys.* **2019**, *150* (15), 154122.
(79) Weigend, F.; Ahlrichs, R. Balanced Basis Sets of Split Valence, Triple Zeta Valence and Quadruple Zeta Valence Quality for H to Rn: Design and Assessment of Accuracy. *Phys. Chem. Chem. Phys.* **2005**, *7* (18), 3297−3305.
(80) Andrae, D.; Häußermann, U.; Dolg, M.; Stoll, H.; Preuß, H. Energy-Adjusted Ab Initio Pseudopotentials for the Second and Third Row Transition Elements. *Theor. Chim. Acta* **1990**, *77* (2), 123−141.
(81) Neese, F.; Wennmohs, F.; Hansen, A.; Becker, U. Efficient, Approximate and Parallel Hartree-Fock and Hybrid DFT Calculations. A 'Chain-of-Spheres' Algorithm for the Hartree-Fock Exchange. *Chem. Phys.* **2009**, *356* (1−3), 98−109.
(82) Weigend, F. Accurate Coulomb-Fitting Basis Sets for H to Rn. *Phys. Chem. Chem. Phys.* **2006**, *8* (9), 1057−1065.
(83) Pulay, P. Convergence acceleration of iterative sequences. The case of SCF iteration. *Chem. Phys. Lett.* **1980**, *73* (2), 393−398.

https://doi.org/10.1021/jacs.3c12427
J. Am. Chem. Soc. 2024, 146, 3331−3342

Supplementary Information for:

Isolation of a bent dysprosium bis(amide) single-molecule magnet

Jack Emerson-King,[1] Gemma K. Gransbury,[1] George F. S. Whitehead,[1] Iñigo J. Vitorica-Yrezabal,[1] Mathieu Rouzières,[2] Rodolphe Clérac,[2,*] Nicholas F. Chilton,[1,3,*] and David P. Mills[1,*]

[1]*Department of Chemistry, The University of Manchester, Oxford Road, Manchester, M13 9PL, UK.*

[2]*Univ. Bordeaux, CNRS, CRPP, UMR 5031, 33600 Pessac, France.*

[3]*Research School of Chemistry, The Australian National University, Sullivans Creek Road, Canberra, ACT, 2601, Australia.*

Contents

1. Modified synthesis of [KN(Si^{i}Pr$_3$)$_2$]

General considerations. We have previously reported the synthesis of HN(Si^{i}Pr$_3$)$_2$ and [KN(Si^{i}Pr$_3$)$_2$].[1] Here we describe a modified synthesis using $NaNH_2$ as a more operationally convenient starting material in place of condensed NH_3, with other synthetic optimizations. The previously reported NMR data are included for completeness. Under dinitrogen, solvents were either refluxed over molten potassium for 4 days (*n*-hexane), or passed over a column of activated alumina (pentanes, THF, toluene). All solvents were degassed, placed under an argon atmosphere, and stored over either a K mirror (*n*-hexane, pentanes, toluene) or over activated 3 Å molecular sieves (THF). All subsequent manipulations were performed under argon using standard Schlenk line techniques, with use of a glove box for storage of $NaNH_2$, KH and [KN(Si^{i}Pr$_3$)$_2$] under argon. ^{n}BuLi (2.5 M in hexanes) and $NaNH_2$ were purchased from Fisher Scientific and were used as received. KH was purchased from Merck as a dispersion in mineral oil, which was removed prior to use through sequential pentane washes. Si^{i}Pr$_3$Cl was purchased from Fluorochem, degassed, and stirred over Mg turnings prior to use. 3 Å molecular sieves were activated by heating at 310 °C *in vacuo* for > 6 hours.

HN(Si^{i}Pr$_3$)$_2$. Si^{i}Pr$_3$Cl (42.1 mL, 200 mmol) was added cautiously to a stirring suspension of $NaNH_2$ (7.80 g, 200 mmol) in THF (200 mL) at ambient temperature, with appropriate external cooling with an ice bath when required to moderate any resulting exotherm. The reaction mixture was stirred at ambient temperature overnight, and the resultant suspension filtered to afford a solution of $H_2NSi^{i}Pr_3$. ^{n}BuLi (2.5 M in hexane, 80 mL, 200 mmol) was added to this solution, and the reaction mixture warmed with stirring until butane gas evolution was observed (at *ca.* 50-60 ºC). The reaction was held at this temperature until all gas evolution had subsided, typically 1-2 h, affording a solution of LiHNSi^{i}Pr$_3$. Si^{i}Pr$_3$Cl (42.1 mL, 200 mmol) was added, and the reaction mixture was heated to 70 ºC for 72 hours.

The volatiles were removed *in vacuo* and the residues extracted into pentane (*ca*. 50 mL) and filtered. Following removal of pentane in vacuo, $HN(Si^iPr_3)_2$ was obtained as a colorless oil by fractional distillation of the crude residues (10^{-2} mbar through a Vigreux column, unreacted $^iPr_3SiCl$ removed at *ca*. 40 ºC, $HN(Si^iPr_3)_2$ collected at *ca*. 100 ºC, significant quantities of some non-volatile material remain). Yield: 21.60 g, 65.6 mmol, 33%, formed a white crystalline solid upon standing (melting point *ca*. 25 ºC). ^{1}H NMR (500 MHz, C_6D_6): δ 1.02–0.87 (complex set of resonances, 42H, $CH(CH_3)_2$ & $(CHCH_3)_2$), –0.37 (s, 1H, N*H*). ^{29}Si{^{1}H} DEPT90 NMR (79.48 MHz, C_6D_6): δ 6.06.

[KN(Si^{i}Pr$_3$)$_2$]. A solution of $HN(Si^iPr_3)_2$ (21.6 g, 65.6 mmol) in toluene (100 mL) was added to a stirring suspension of KH (2.62 g, 65.6 mmol) in toluene (100 mL). The reaction mixture was heated until hydrogen evolution was observed (*ca*. 120 °C). The reaction was held at this temperature until gas evolution had ceased (typically 3 h), allowed to cool, and filtered to remove any insoluble K salts. The solution was concentrated to the point of incipient crystallization and layered with excess hexane, which after slow diffusion afforded the title compound as large colorless crystalline blocks. Occasionally, a brown discoloration is observed when using $HN(Si^iPr_3)_2$ containing trace impurities. Two or three recrystallizations as outlined above are sufficient to afford a product with no detectable protic impurities. Yield: 17.90 g, 48.7 mmol, 74%, colorless crystalline solid. ^{1}H NMR (400.07 MHz, C_6D_6): δ 1.30 (d, $^3J_{HH}$ = 7.4 Hz, 36H, $CHCH_3$), 0.90 (sept, $^3J_{HH}$ = 7.5 Hz, 6H, $CHCH_3$). ^{29}Si{^{1}H} DEPT90 NMR (79.48 MHz, C_6D_6): δ 16.35.

2. NMR spectra

2.1 $HN(Si^iPr_3)_2$

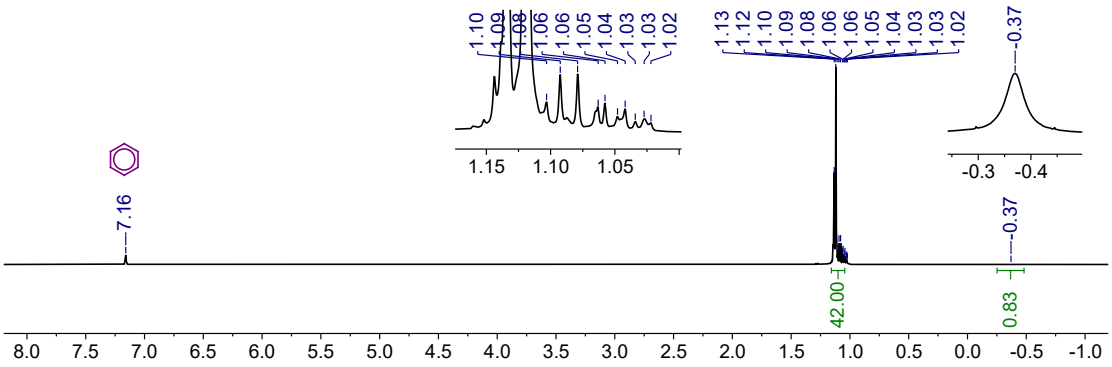

Figure S1. ^1H NMR spectrum (400.07 MHz, C_6D_6) of $HN(Si^iPr_3)_2$ at 298 K.

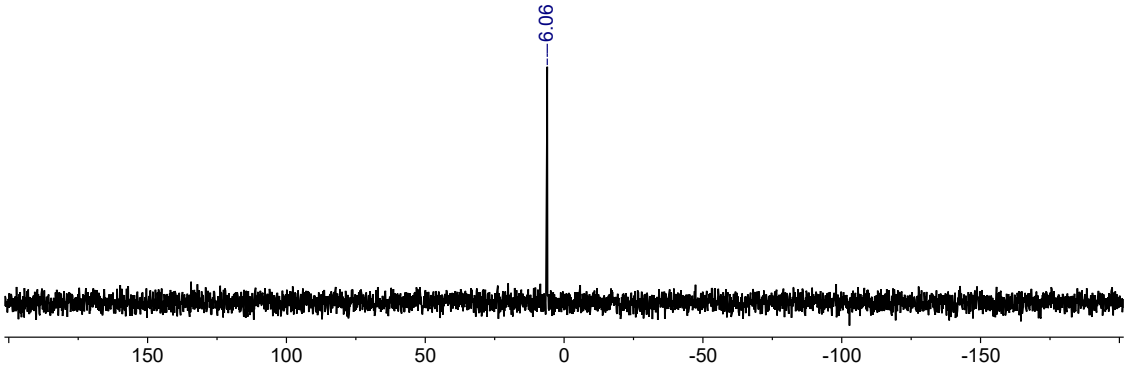

Figure S2. $^{29}Si\{^1H\}$ DEPT90 NMR spectrum (79.48 MHz, C_6D_6) of $HN(Si^iPr_3)_2$ at 298 K.

2.2 $[KN(Si^iPr_3)_2]$

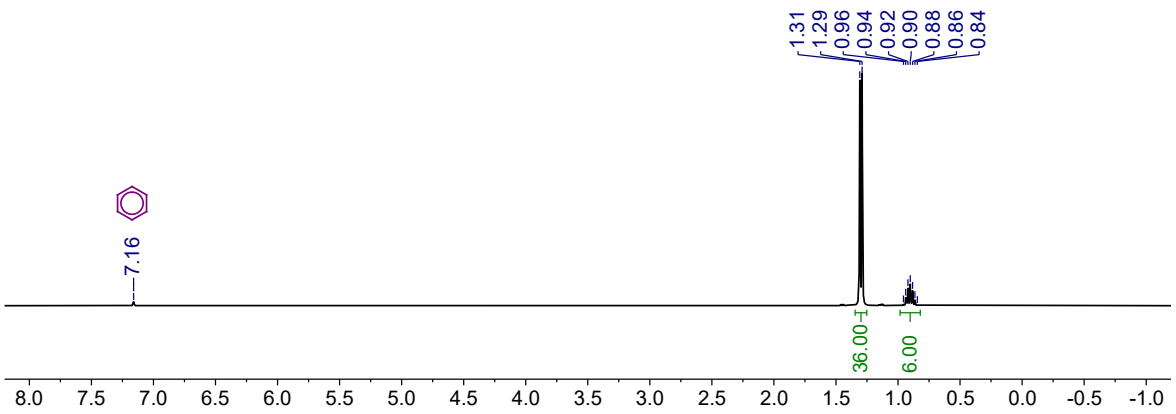

Figure S3. ^1H NMR spectrum (400.07 MHz, C_6D_6) of $[KN(Si^iPr_3)_2]$ at 298 K.

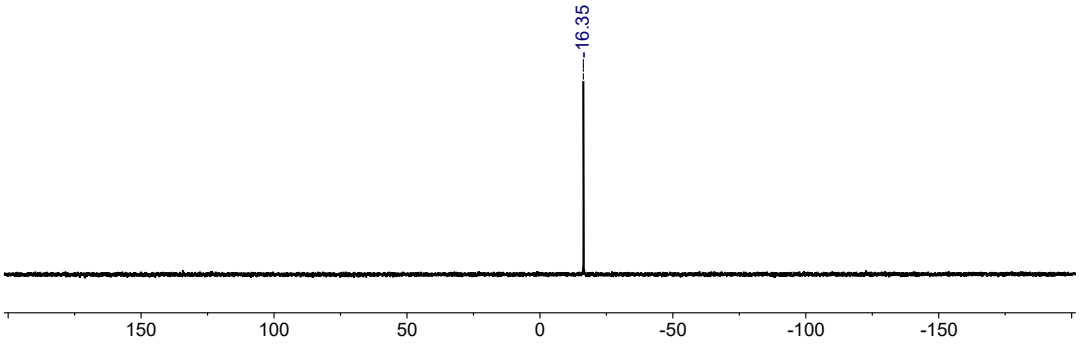

Figure S4. $^{29}Si\{^{1}H\}$ DEPT90 NMR spectrum (79.48 MHz, C_6D_6) of $[KN(Si^{i}Pr_3)_2]$ at 298 K.

2.3 $[Y\{N(Si^{i}Pr_3)_2\}_2][Al\{OC(CF_3)_3\}_4]$ (1-Y)

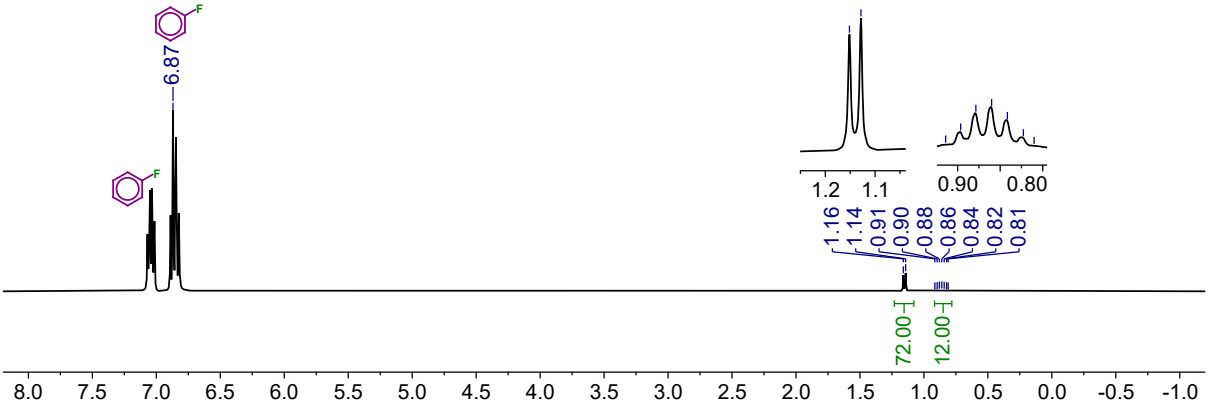

Figure S5. ^{1}H NMR spectrum (400.07 MHz, C_6H_5F) of **1-Y** at 298 K.

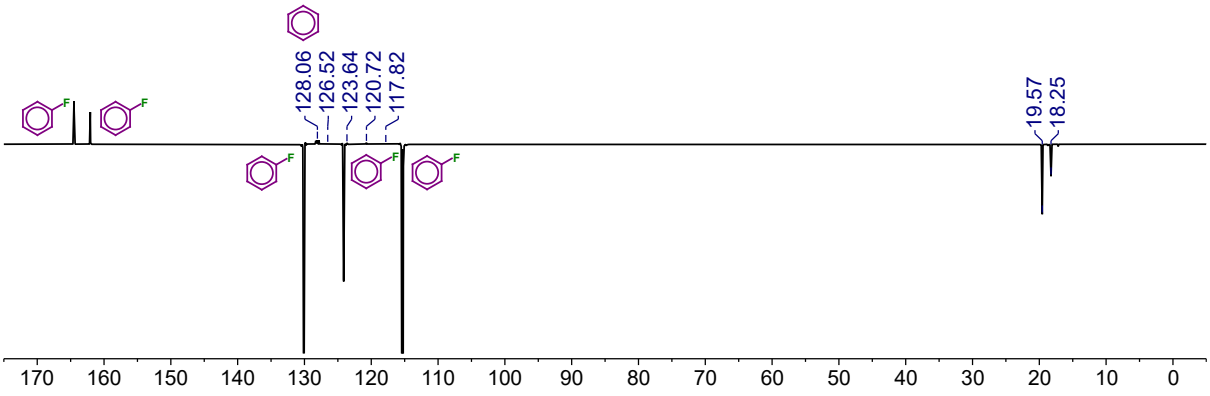

Figure S6. $^{13}C\{^{1}H\}$ DEPTQ NMR spectrum (100.60 MHz, C_6H_5F) of **1-Y** at 298 K.

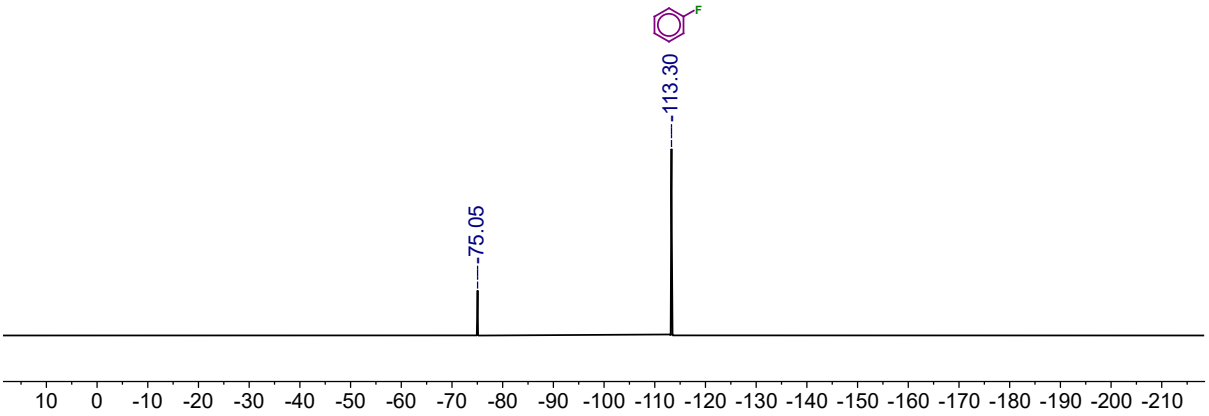

Figure S7. ^{19}F NMR spectrum (376.40 MHz, C_6H_5F) of **1-Y** at 298 K.

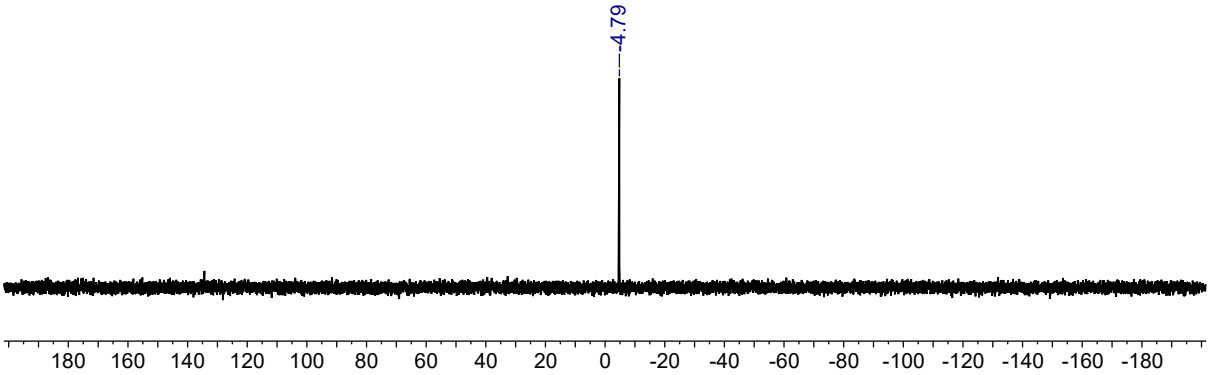

Figure S8. ^{29}Si{^{1}H} DEPT90 NMR spectrum (79.48 MHz, C_6H_5F) of **1-Y** at 298 K.

2.4 [Dy{N(Si^{i}Pr$_3$)$_2$}$_2$][Al{OC(CF$_3$)$_3$}$_4$] (1-Dy)

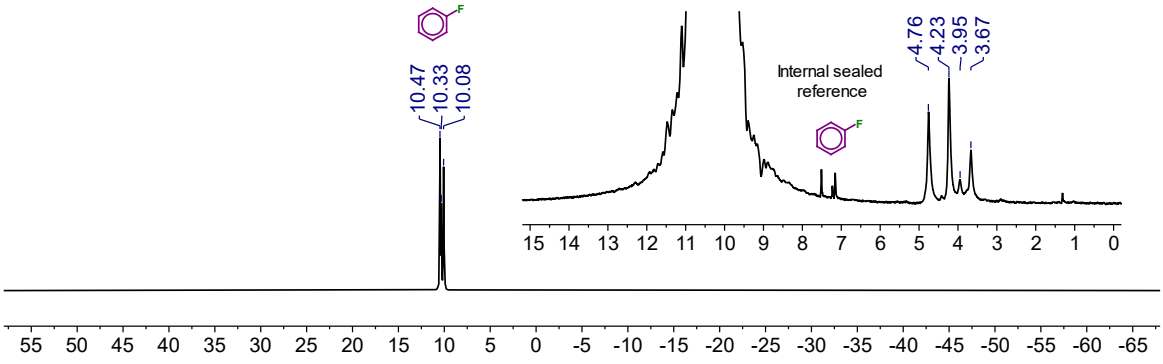

Figure S9. ^{1}H NMR spectrum (400.07 MHz, C_6H_5F) of **1-Dy** at 298 K containing an internal sealed capillary of 1 : 1 C_6D_6 : C_6H_5F.

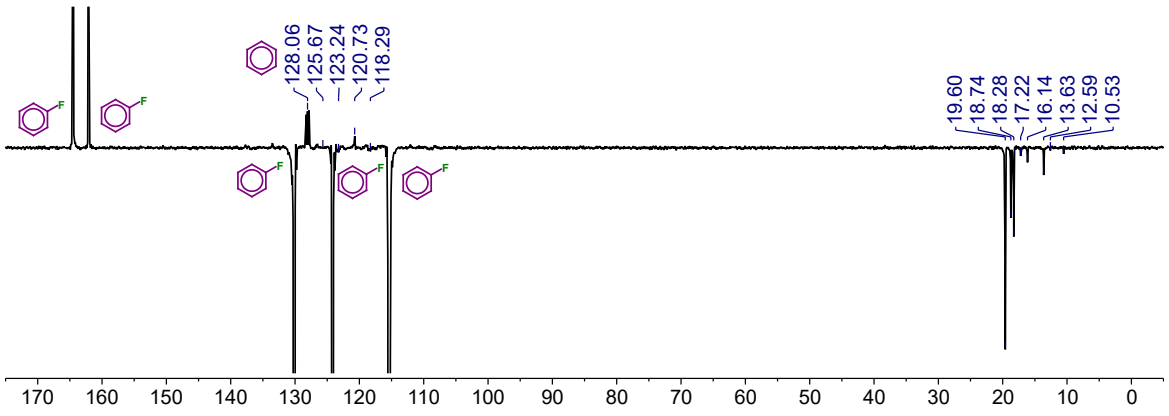

Figure S10. $^{13}C\{^{1}H\}$ DEPTQ NMR spectrum (100.60 MHz, C_6H_5F) of **1-Dy** at 298 K containing an internal sealed capillary of 1 : 1 C_6D_6 : C_6H_5F.

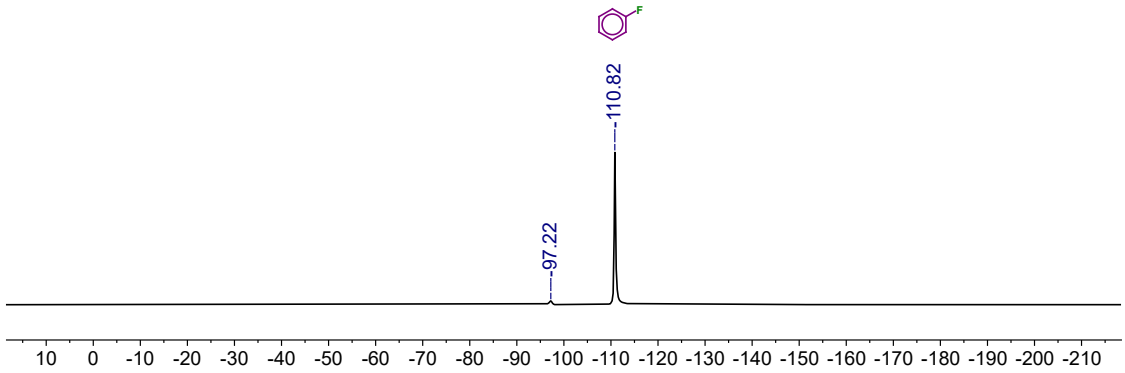

Figure S11. ^{19}F NMR spectrum (376.40 MHz, C_6H_5F) of **1-Dy** at 298 K containing an internal sealed capillary of 1 : 1 C_6D_6 : C_6H_5F.

2.5 [Y{N(Si^{i}Pr$_3$)$_2$}(BH$_4$)$_2$(THF)] (2-Y)

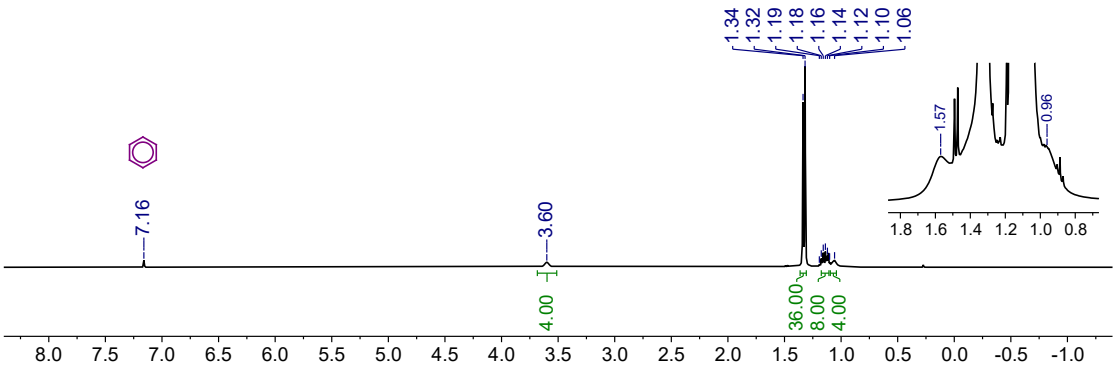

Figure S12. ^{1}H NMR spectrum (400.07 MHz, C_6D_6) of **2-Y** at 298 K.

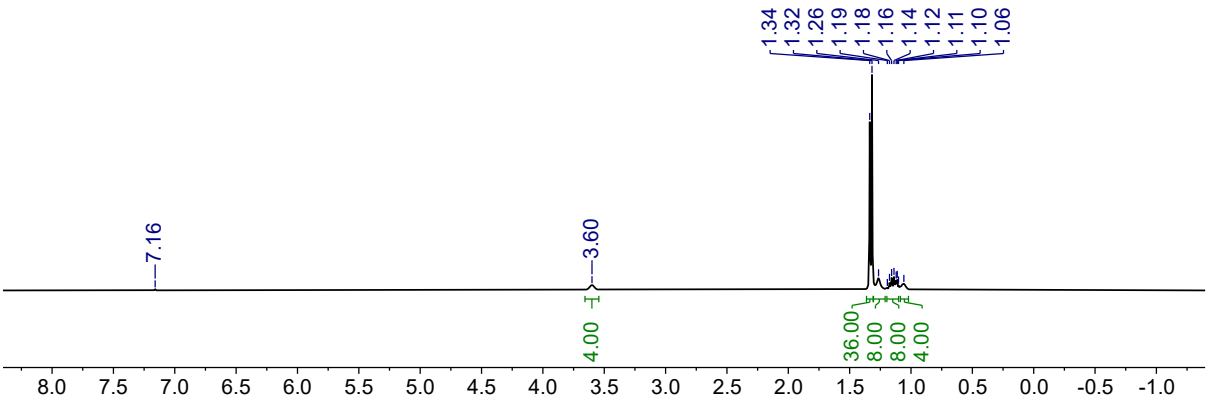

Figure S13. $^{1}H\{^{11}B\}$ NMR spectrum (400.07 MHz, C_6D_6) of **2-Y** at 298 K.

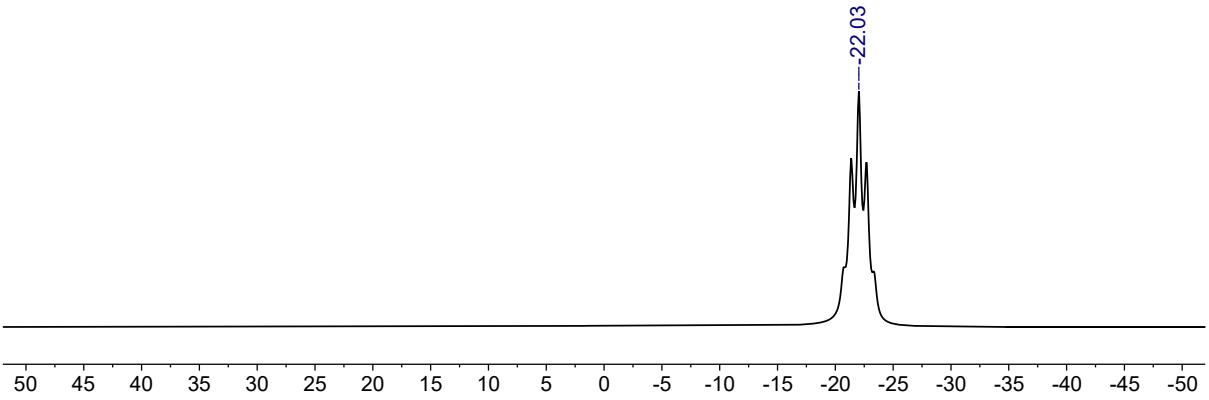

Figure S14. ^{11}B NMR spectrum (128 MHz, C_6D_6) of **2-Y** at 298 K.

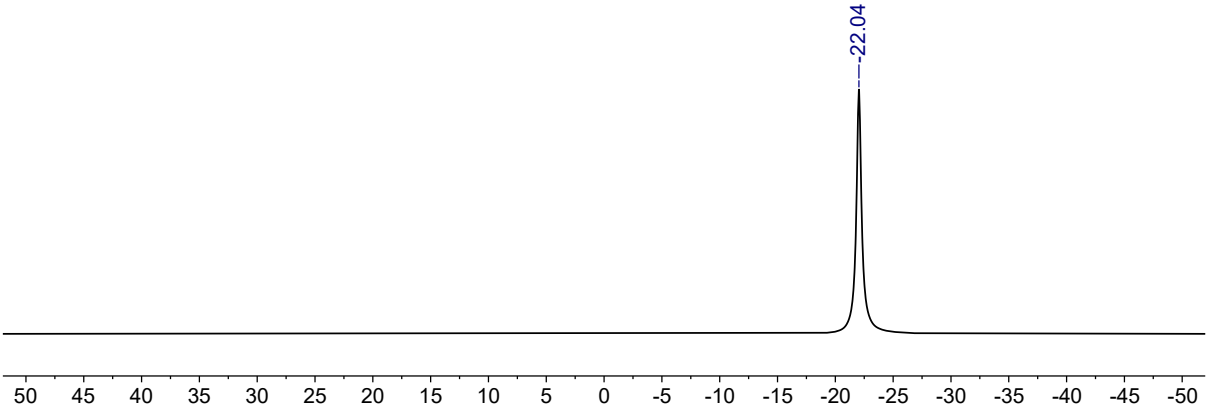

Figure S15. $^{11}B\{^{1}H\}$ NMR spectrum (128 MHz, C_6D_6) of **2-Y** at 298 K.

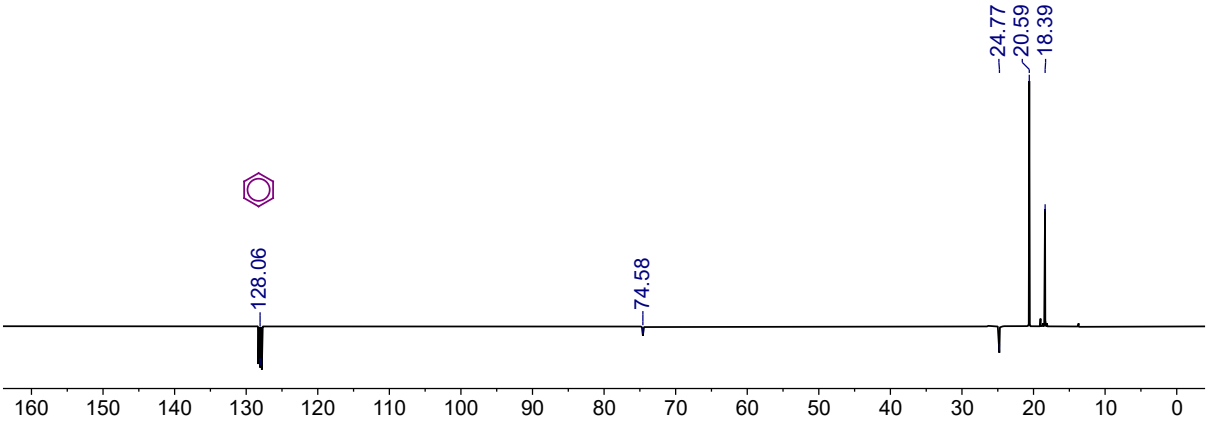

Figure S16. $^{13}C\{^{1}H\}$ DEPTQ NMR spectrum (100.60 MHz, C_6D_6) of **2-Y** at 298 K.

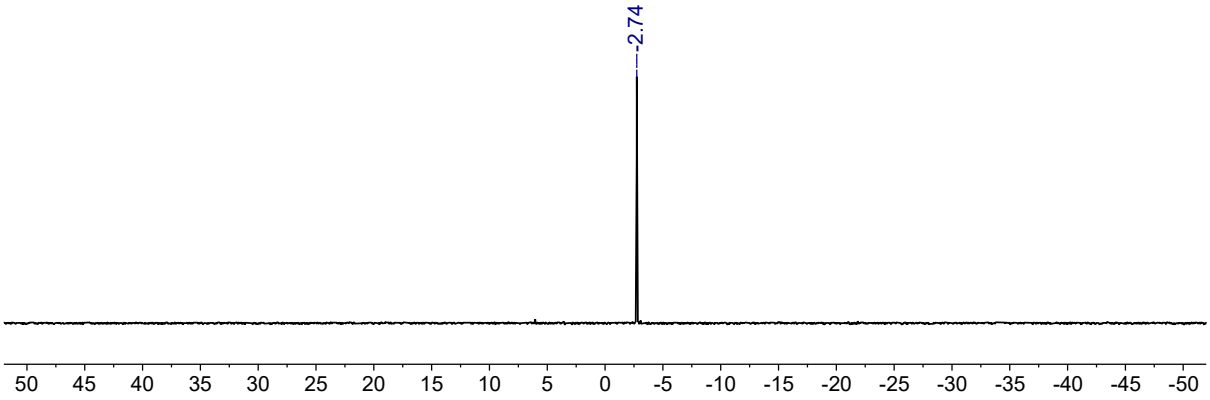

Figure S17. $^{29}Si\{^{1}H\}$ DEPT90 NMR spectrum (79.48 MHz, C_6D_6) of **2-Y** at 298 K.

2.6 [Dy{N(Si^{i}Pr$_3$)$_2$}(BH$_4$)$_2$(THF)] (2-Dy)

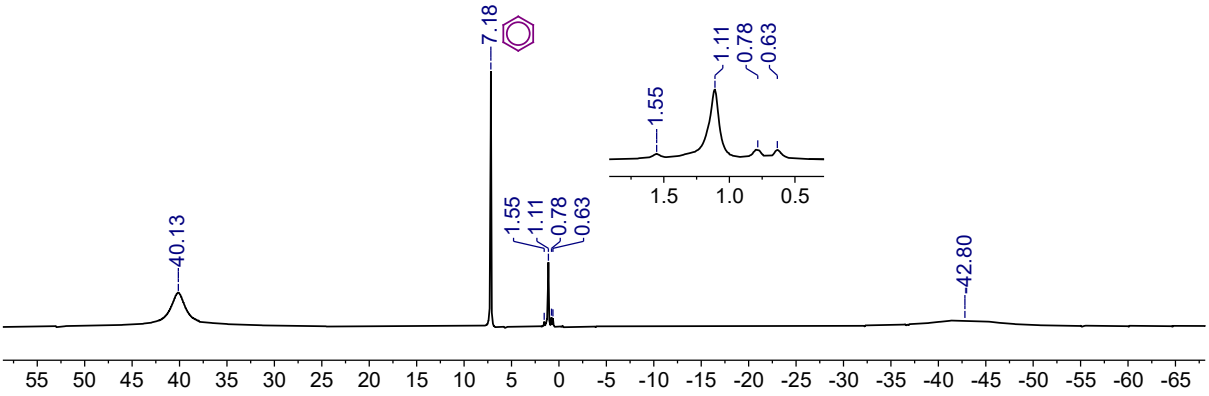

Figure S18. ^{1}H NMR spectrum (400.07 MHz, C_6D_6) of **2-Dy** at 298 K.

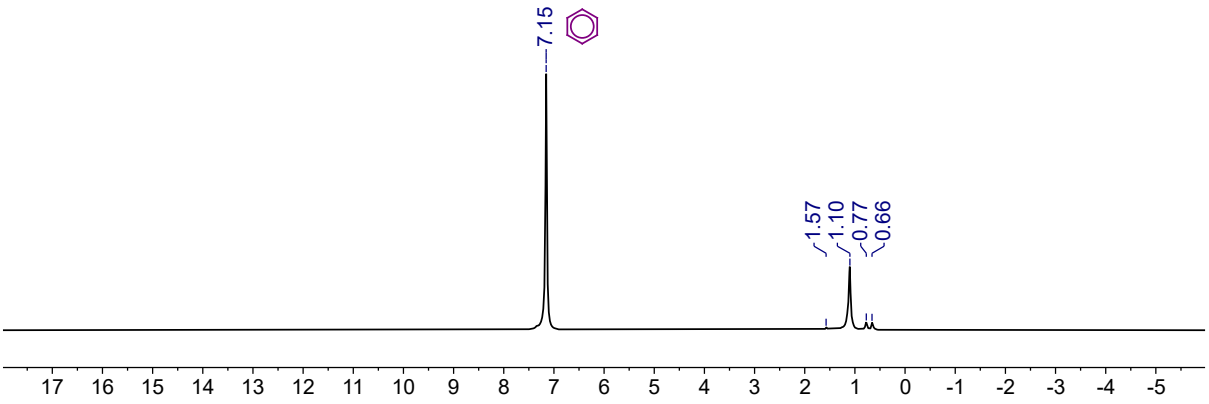

Figure S19. $^{1}H\{^{11}B\}$ NMR spectrum (400.07 MHz, C_6D_6) of **2-Dy** at 298 K.

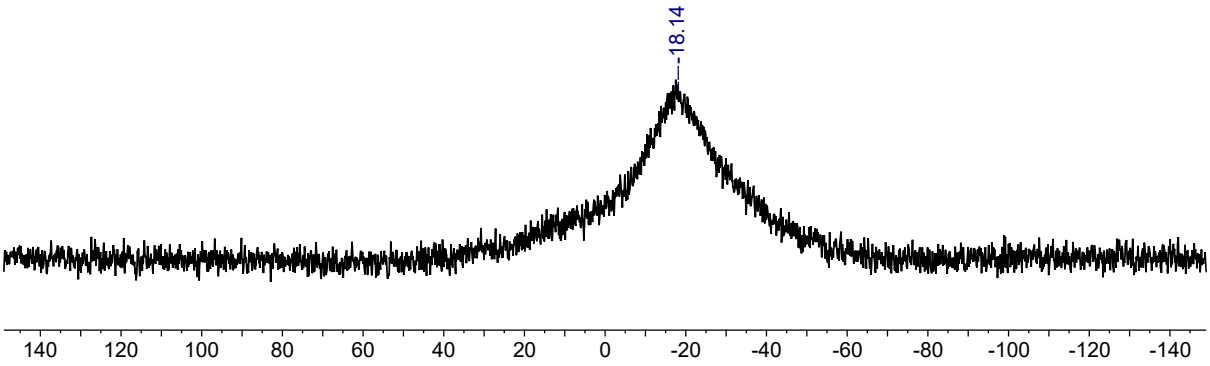

Figure S20. ^{11}B NMR spectrum (128 MHz, C_6D_6) of **2-Dy** at 298 K.

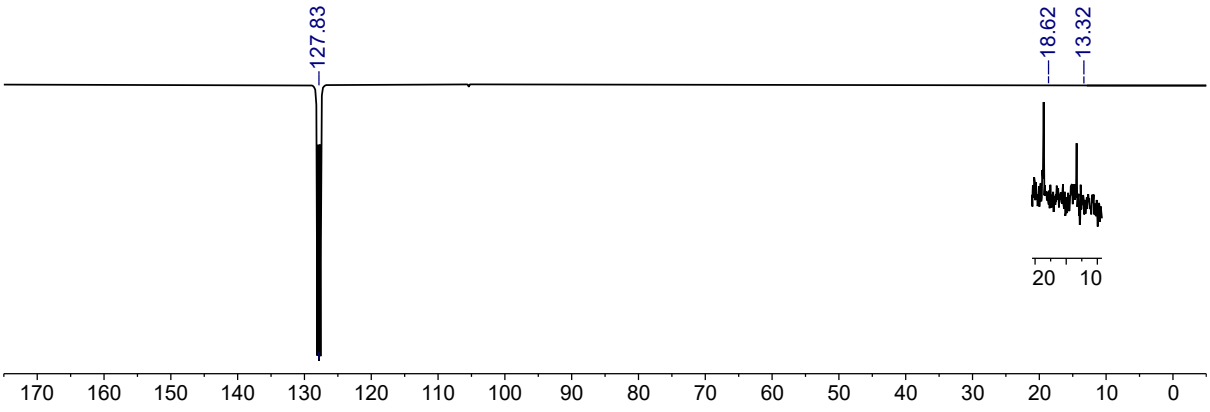

Figure S21. $^{13}C\{^{1}H\}$ DEPTQ NMR spectrum (100.60 MHz, C_6H_5F) of **2-Dy** at 298 K containing an internal sealed capillary of 1 : 1 C_6D_6 : C_6H_5F.

2.7 [Y{N(Si^{i}Pr$_3$)$_2$}(BH$_4$)(μ-BH$_4$)]$_4$ (3-Y)

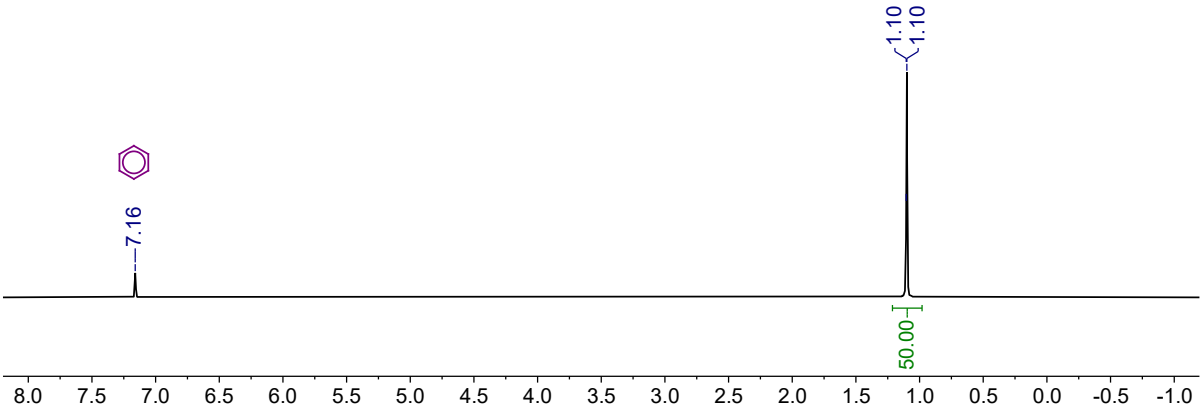

Figure S22. ^{1}H NMR spectrum (400.07 MHz, C_6D_6) of **3-Y** at 298 K.

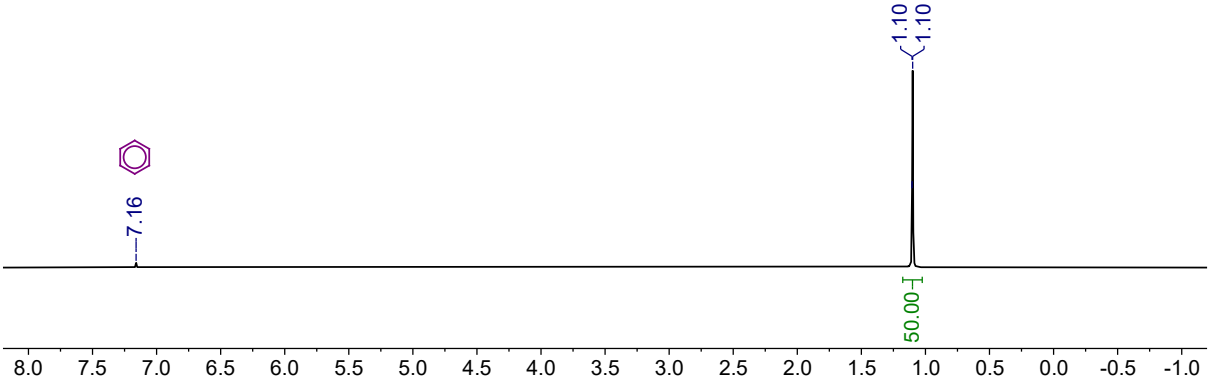

Figure S23. ^{1}H{^{11}B} NMR spectrum (400.07 MHz, C_6D_6) of **3-Y** at 298 K.

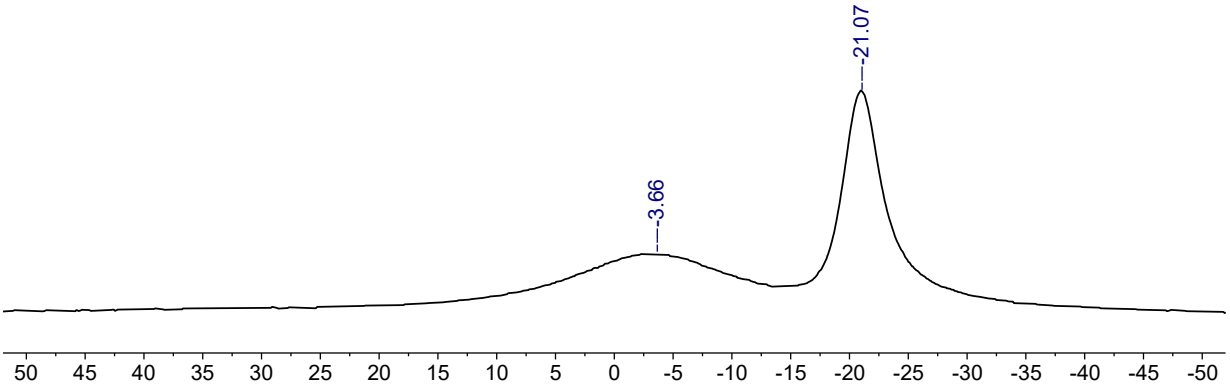

Figure S24. ^{11}B NMR spectrum (128 MHz, C_6D_6) of **3-Y** at 298 K.

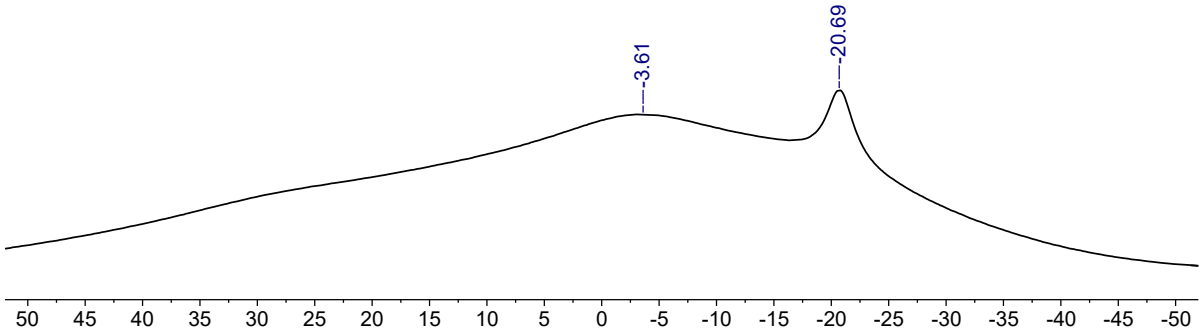

Figure S25. $^{11}B\{^{1}H\}$ NMR spectrum (128 MHz, C_6D_6) of **3-Y** at 298 K.

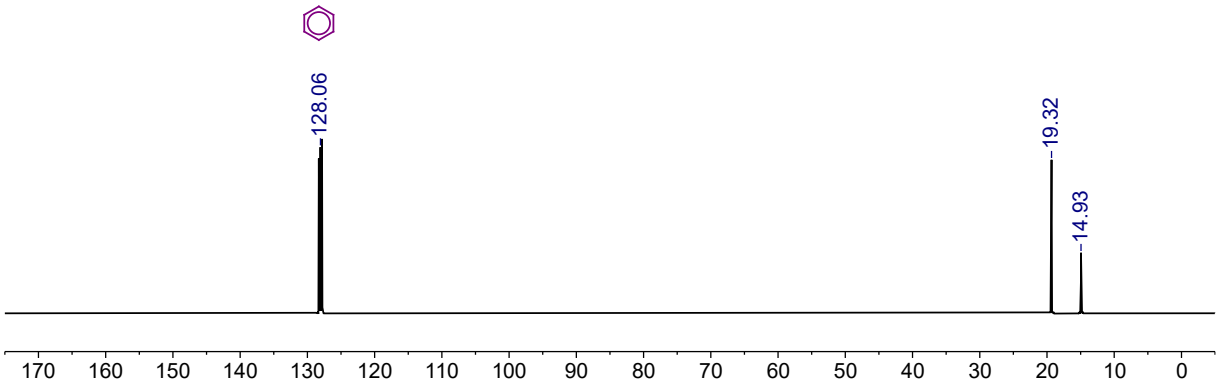

Figure S26. $^{13}C\{^{1}H\}$ DEPTQ NMR spectrum (100.60 MHz, C_6D_6) of **3-Y** at 298 K.

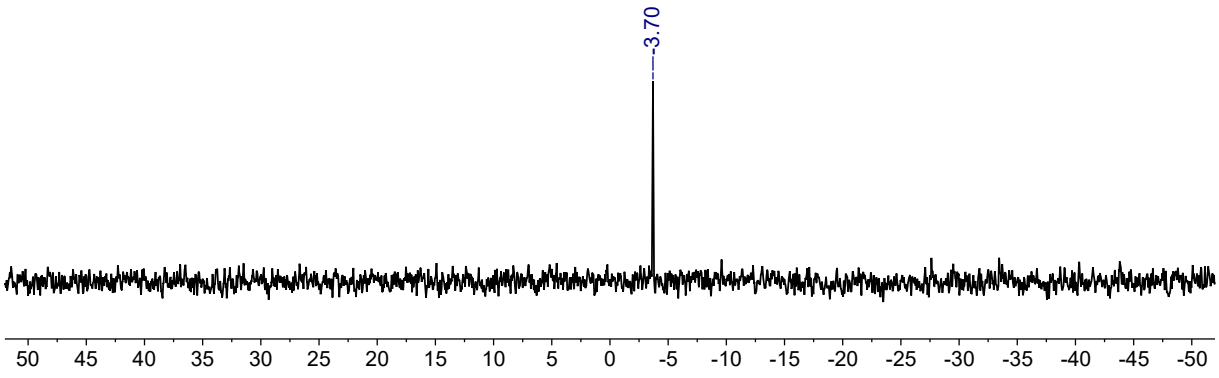

Figure S27. $^{29}Si\{^{1}H\}$ DEPT90 NMR spectrum (79.48 MHz, $C_6H_4F_2$) of **3-Y** at 298 K.

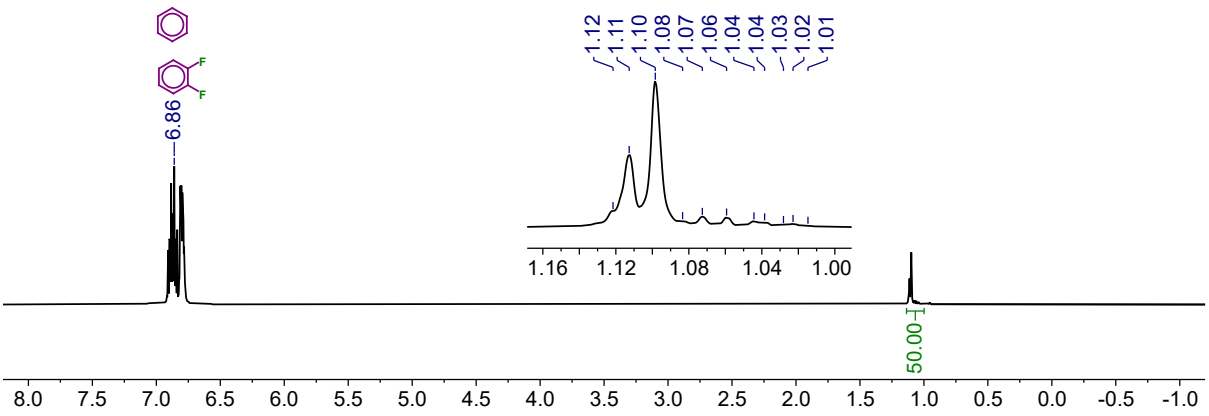

Figure S28. ^{1}H NMR spectrum (400.07 MHz, $C_6H_4F_2$) of **3-Y** at 298 K.

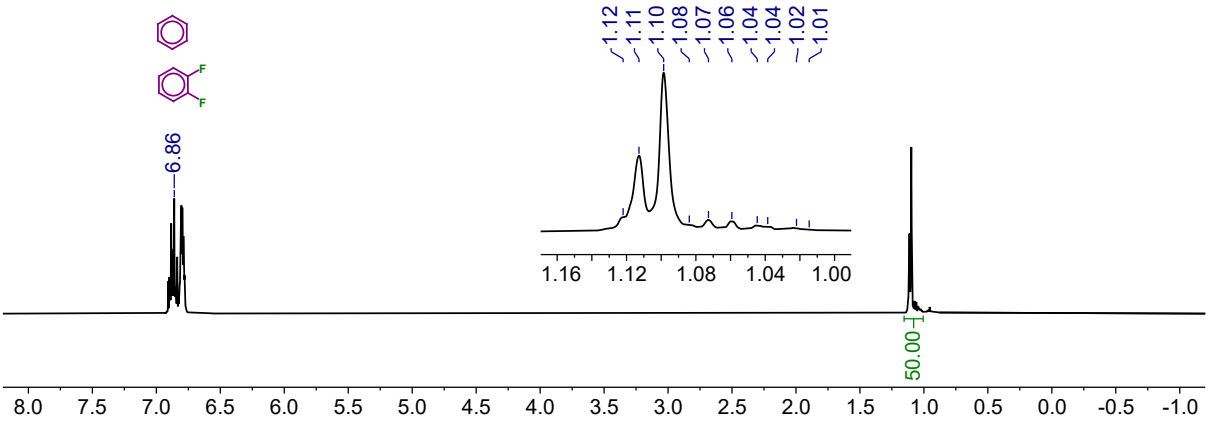

Figure S29. ^{1}H{^{11}B} NMR spectrum (400.07 MHz, $C_6H_4F_2$) of **3-Y** at 298 K.

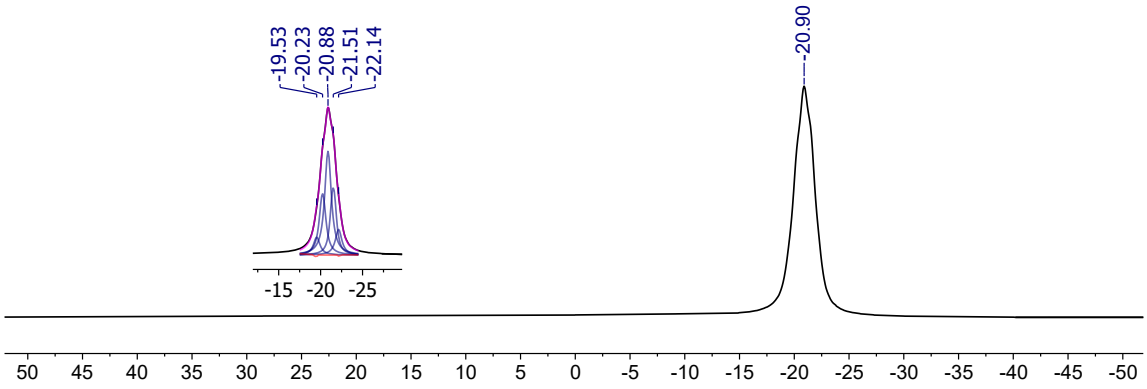

Figure S30. ^{11}B NMR spectrum (128 MHz, $C_6H_4F_2$) of **3-Y** at 298 K. Inset: line fitting of the resonance as a broad pentet, using a generalized-Lorentzian form with no additional constraints, as implemented in MestReNova version 14.3.

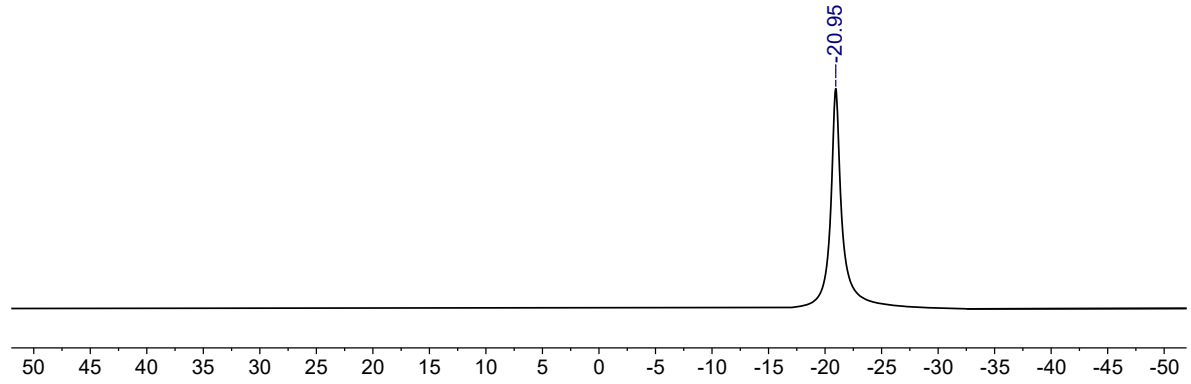

Figure S31. $^{11}B\{^{1}H\}$ NMR spectrum (128 MHz, $C_6H_4F_2$) of **3-Y** at 298 K.

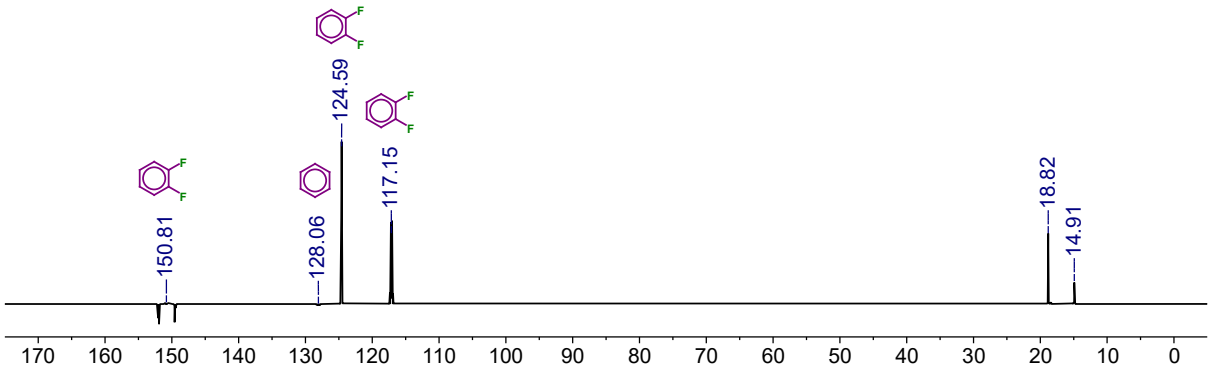

Figure S32. $^{13}C\{^{1}H\}$ DEPTQ NMR spectrum (100.60 MHz, $C_6H_4F_2$) of **3-Y** at 298 K.

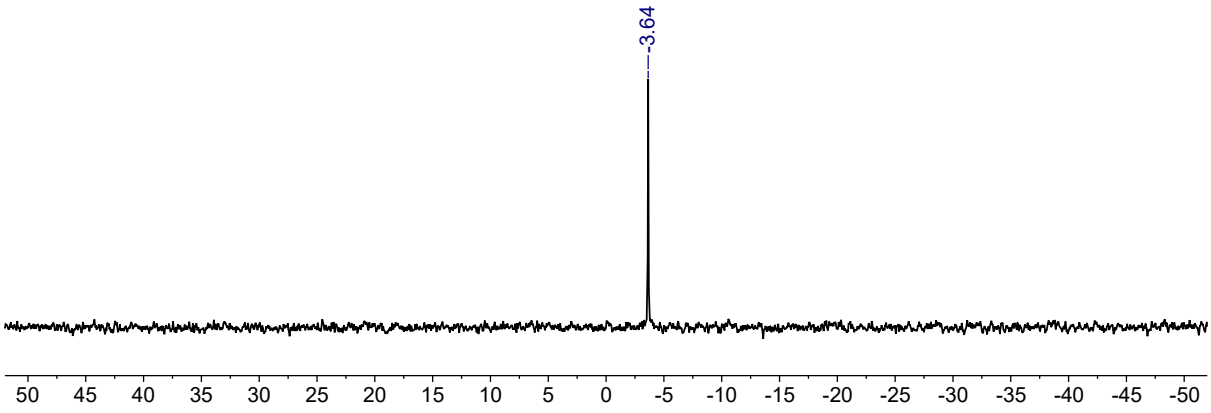

Figure S33. $^{29}Si\{^{1}H\}$ DEPT90 NMR spectrum (79.48 MHz, $C_6H_4F_2$) of **3-Y** at 298 K.

2.8 [Dy{N(Si^{i}Pr$_3$)$_2$}(BH$_4$)(μ-BH$_4$)]$_4$ (3-Dy)

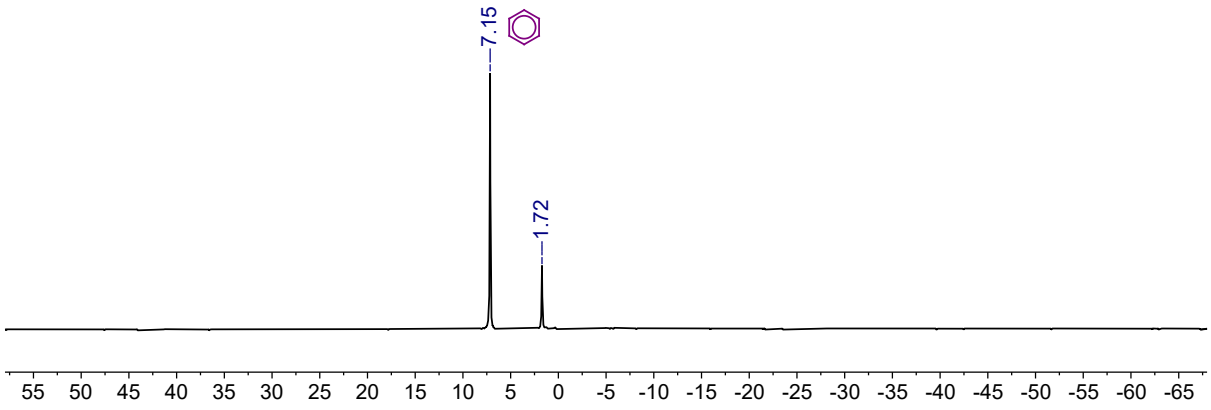

Figure S34. ^{1}H NMR spectrum (400.07 MHz, C_6D_6) of **3-Dy** at 298 K.

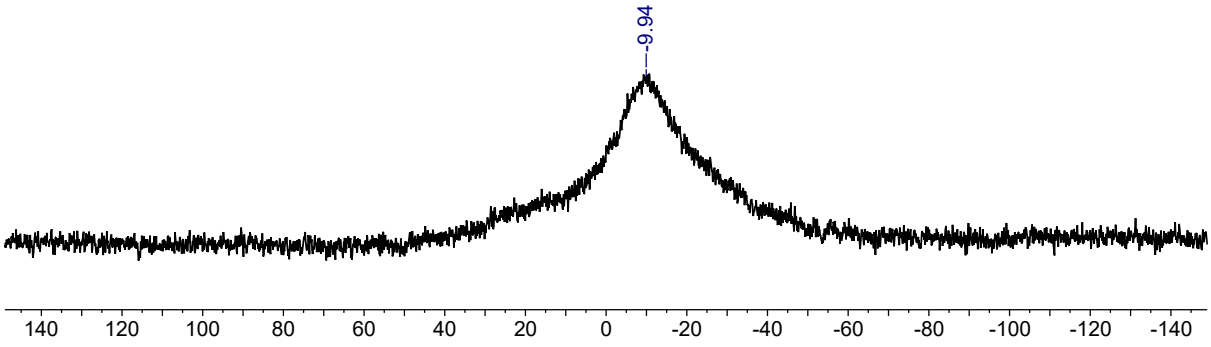

Figure S35. ^{11}B NMR spectrum (128 MHz, C_6D_6) of **3-Dy** at 298 K.

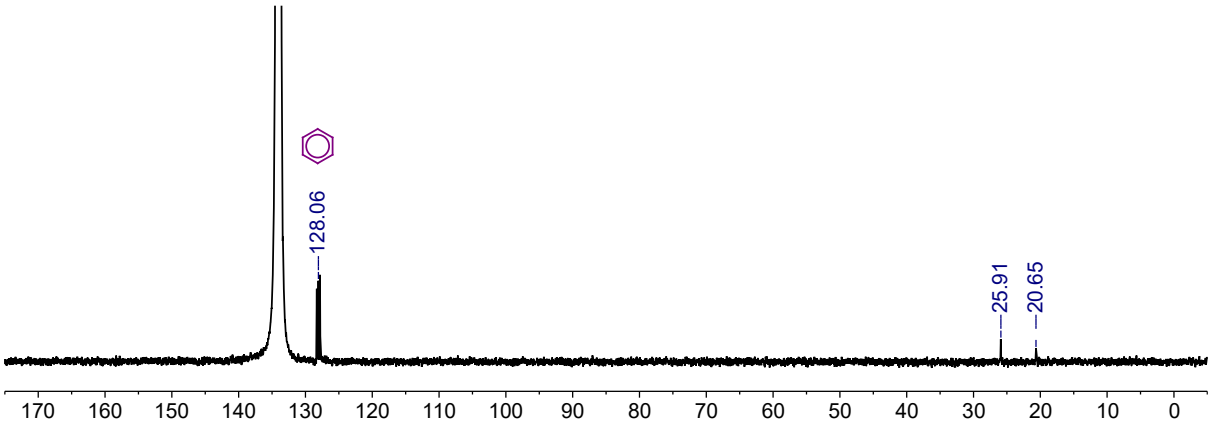

Figure S36. ^{13}C{^{1}H} DEPTQ NMR spectrum (100.60 MHz, C_6D_6) of **3-Dy** at 298 K.

2.9 [Y{N(Si^{i}Pr$_3$)$_2$}$_2$(BH$_4$)] (4-Y)

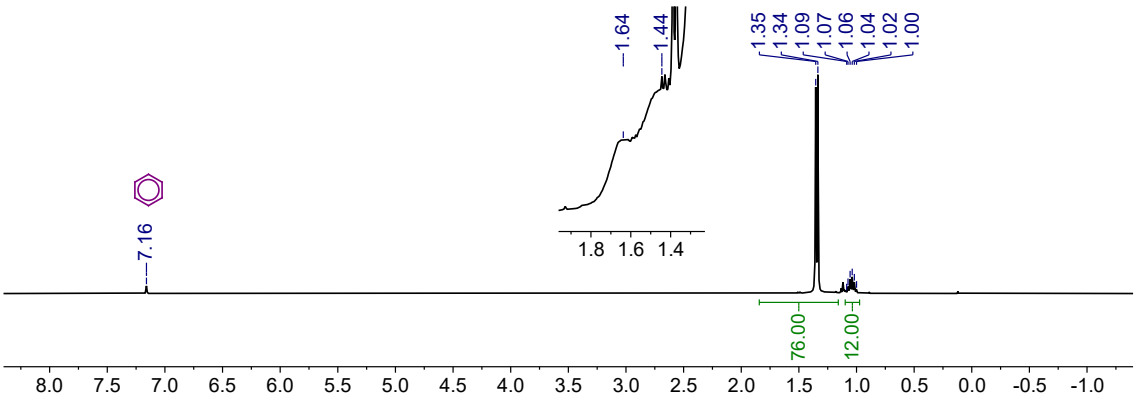

Figure S37. ^{1}H NMR spectrum (400.07 MHz, C_6D_6) of **4-Y** at 298 K.

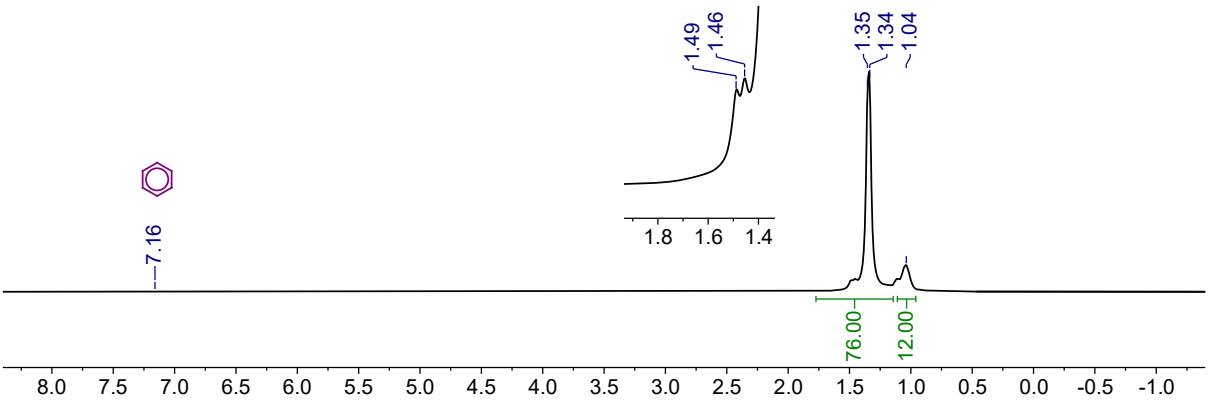

Figure S38. ^{1}H{^{11}B} NMR spectrum (400.07 MHz, C_6D_6) of **4-Y** at 298 K.

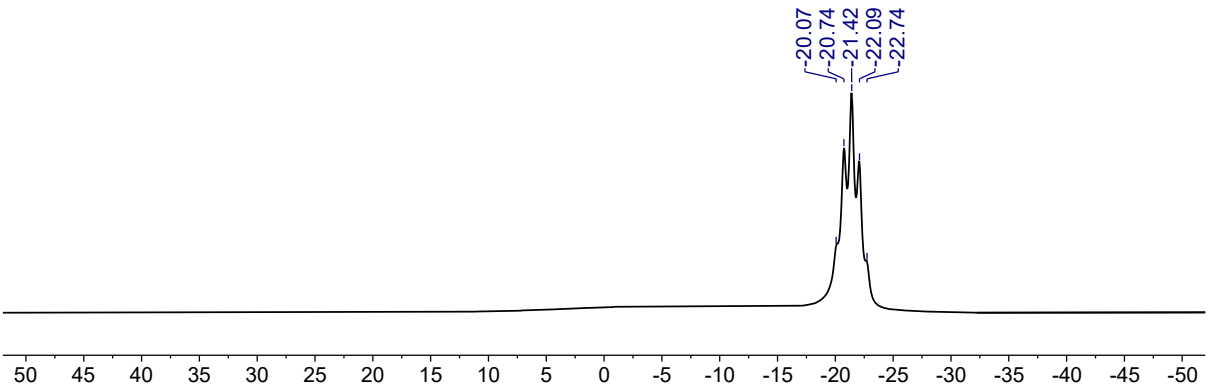

Figure S39. ^{11}B NMR spectrum (128 MHz, C_6D_6) of **4-Y** at 298 K.

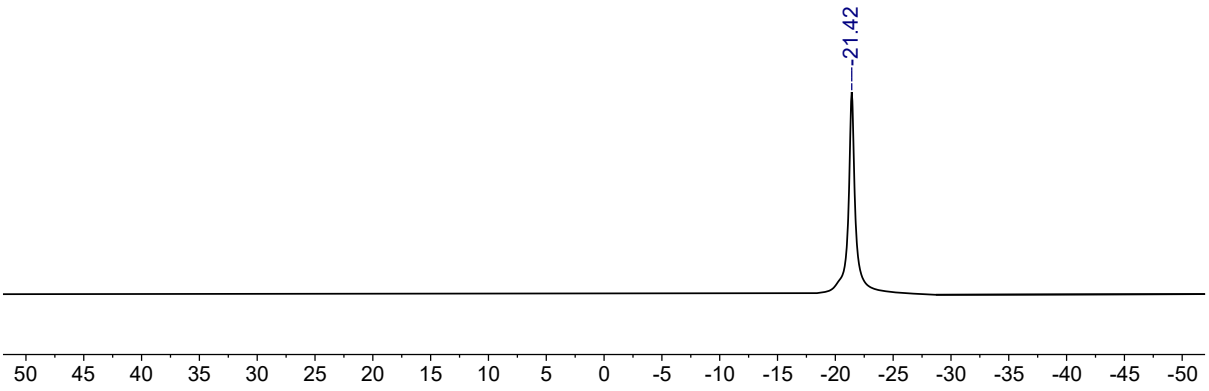

Figure S40. $^{11}B\{^{1}H\}$ NMR spectrum (128 MHz, C_6D_6) of **4-Y** at 298 K.

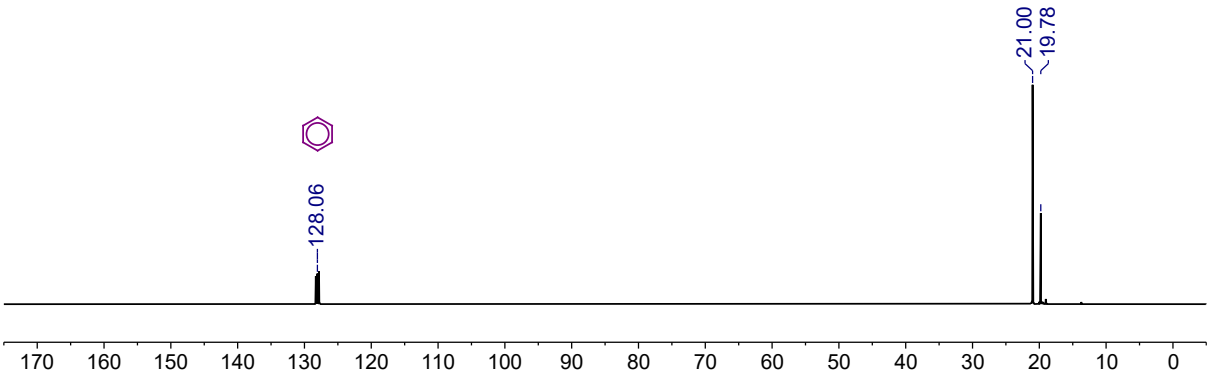

Figure S41. $^{13}C\{^{1}H\}$ DEPTQ NMR spectrum (100.60 MHz, C_6D_6) of **4-Y** at 298 K.

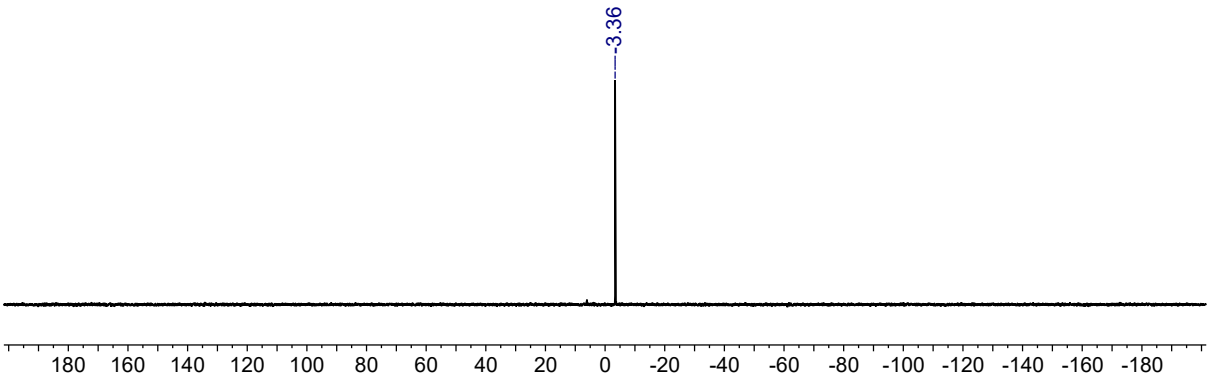

Figure S42. $^{29}Si\{^{1}H\}$ DEPT90 NMR spectrum (79.48 MHz, C_6D_6) of **4-Y** at 298 K.

2.10 [Dy{N(Si^{i}Pr$_3$)$_2$}$_2$(BH$_4$)] (4-Dy)

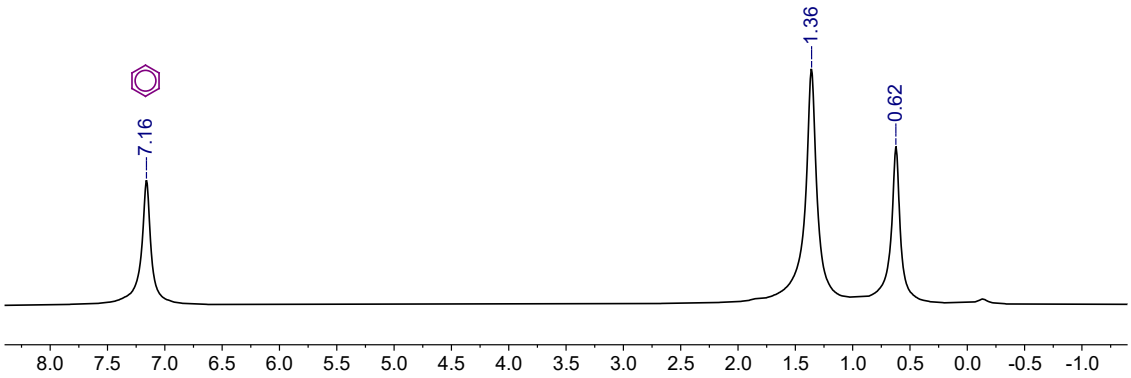

Figure S43. ^{1}H NMR spectrum (400.07 MHz, C_6D_6) of **4-Dy** at 298 K.

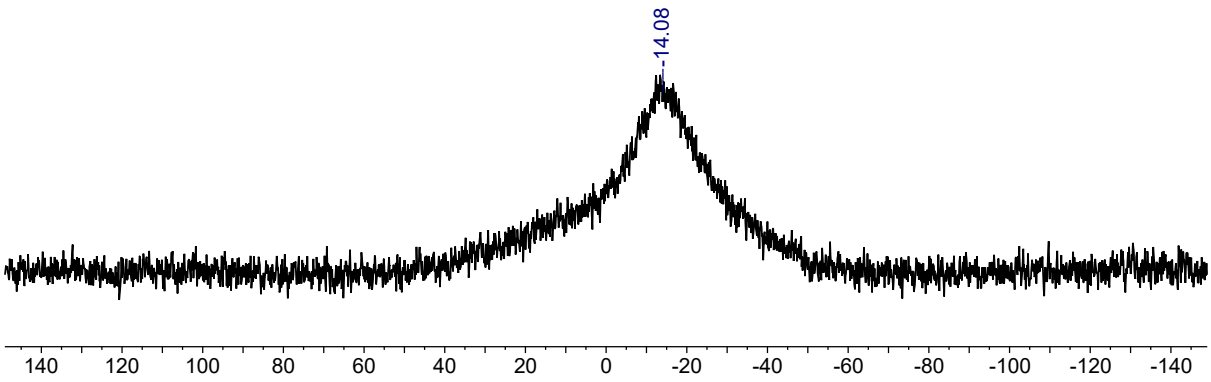

Figure S44. ^{11}B NMR spectrum (128 MHz, C_6D_6) of **4-Dy** at 298 K.

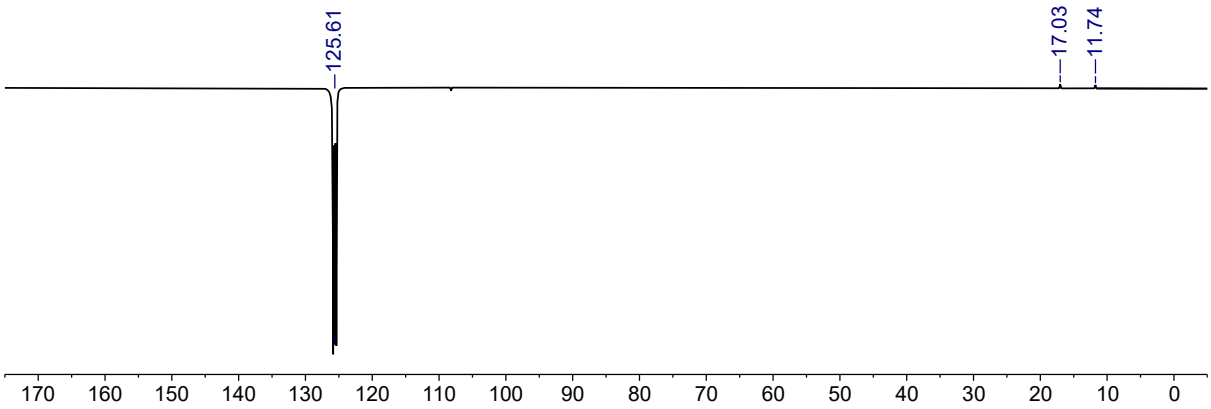

Figure S45. ^{13}C{^{1}H} DEPTQ NMR spectrum (100.60 MHz, C_6D_6) of **4-Dy** at 298 K.

2.11 [Y{N(Si^{i}Pr$_3$)$_2$}{N(Si^{i}Pr$_3$)[Si(^{i}Pr)$_2$}{CH(Me)CH$_2$}]-κ^2-N,C}] (5-Y)/HN(Si^{i}Pr$_3$)$_2$

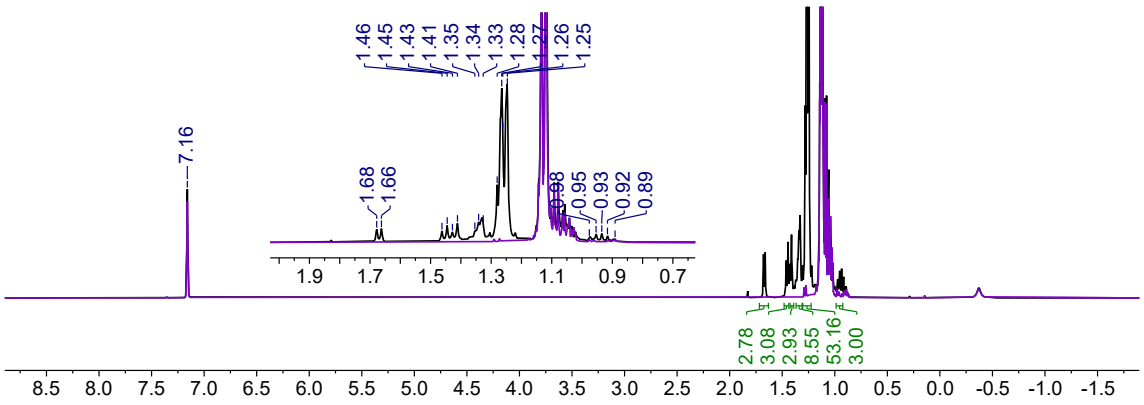

Figure S46. ^{1}H NMR spectrum (400.07 MHz, C_6D_6) of **5-Y** + HN(Si^{i}Pr$_3$)$_2$ at 298 K, overlaid with a spectrum of isolated HN(Si^{i}Pr$_3$)$_2$ (purple) under the same conditions.

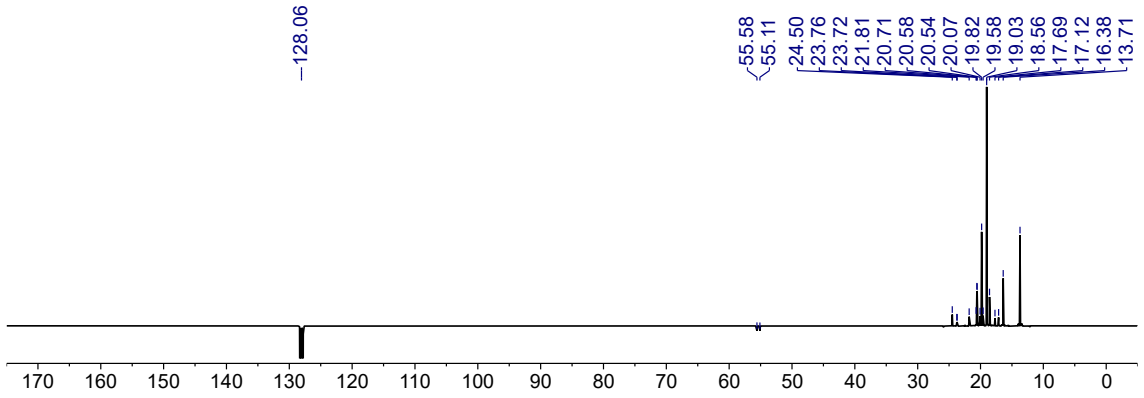

Figure S47. ^{13}C{^{1}H} DEPTQ NMR spectrum (100.60 MHz, C_6D_6) of **5-Y** + HN(Si^{i}Pr$_3$)$_2$ at 298 K.

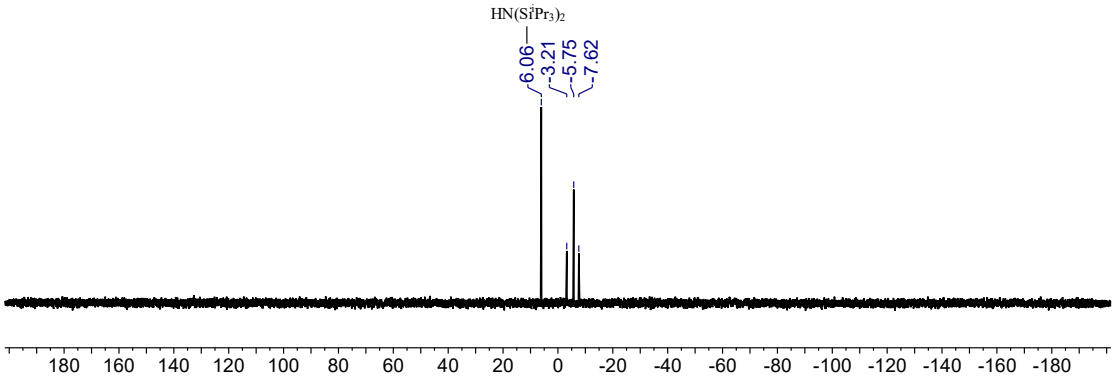

Figure S48. ^{29}Si{^{1}H} DEPT90 NMR spectrum (79.48 MHz, C_6D_6) of **5-Y** + HN(Si^{i}Pr$_3$)$_2$ at 298 K.

3. IR spectra

3.1 [Ln{N(Si^{i}Pr$_3$)$_2$}$_2$][Al{OC(CF$_3$)$_3$}$_4$] (1-Ln)

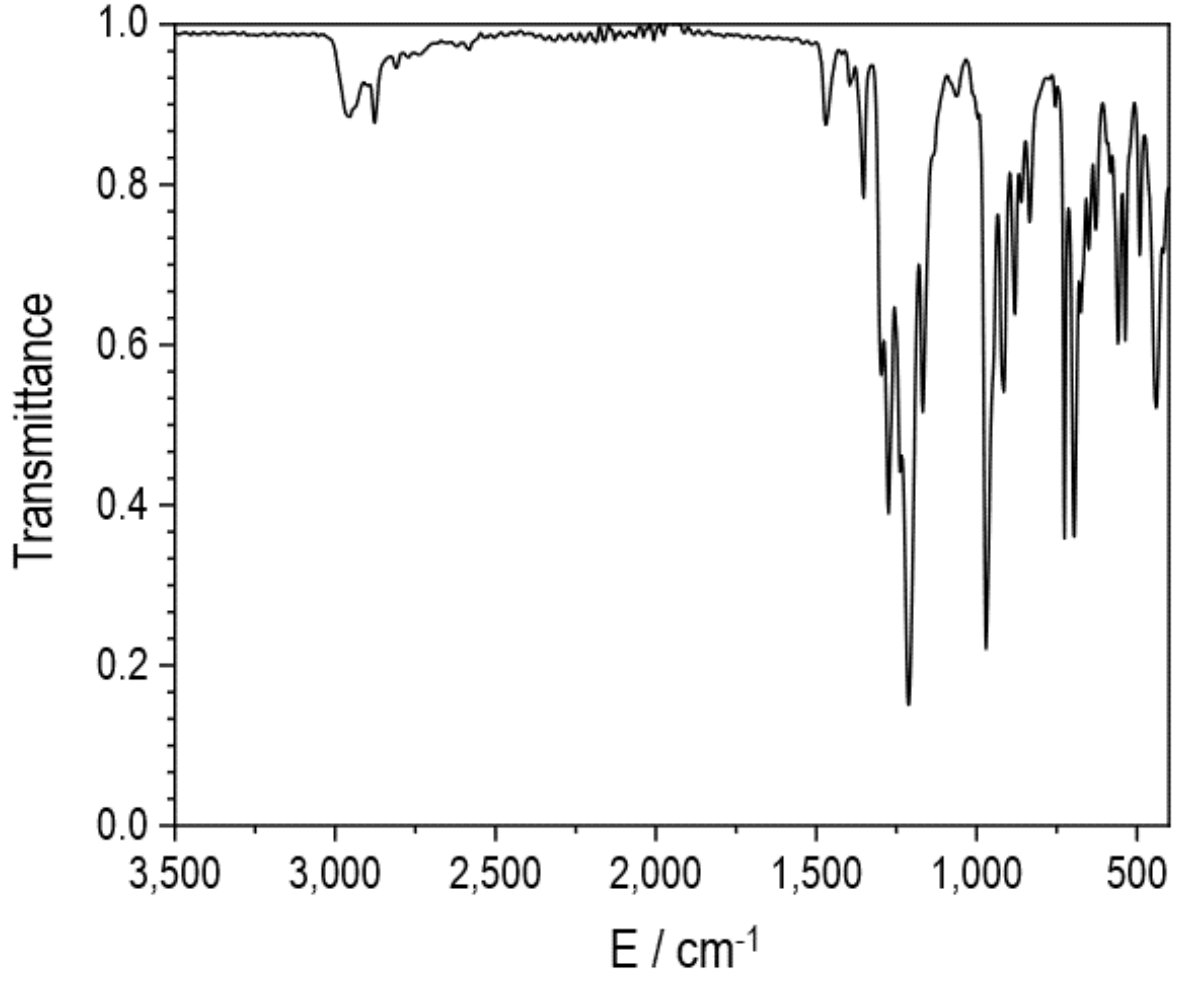

Figure S49. FT-IR (ATR, microcrystalline solid) spectrum of **1-Y** at ambient temperature.

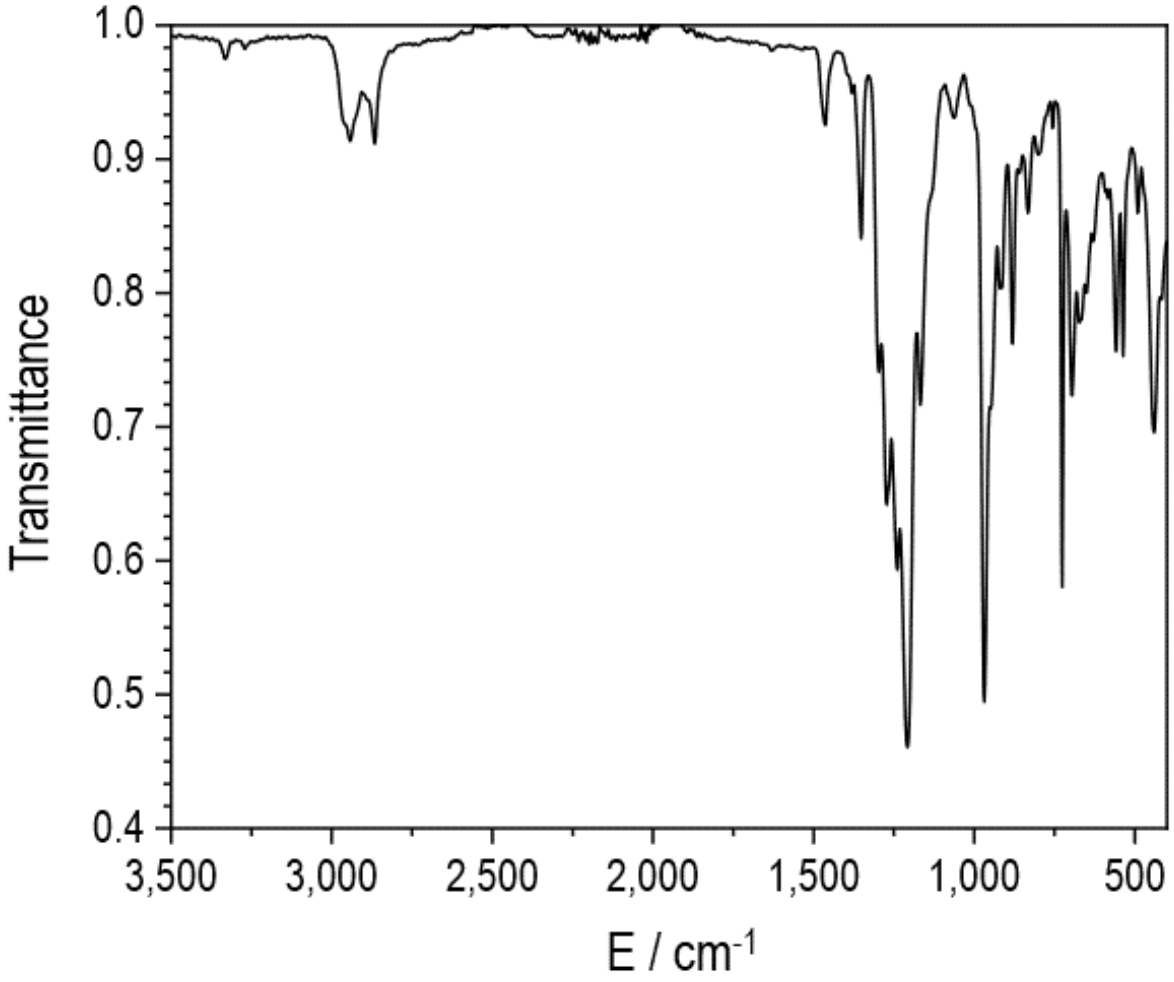

Figure S50. FT-IR (ATR, microcrystalline solid) spectrum of **1-Dy** at ambient temperature.

3.2 [Ln{N(Si^{i}Pr$_3$)$_2$}(BH$_4$)$_2$(THF)] (2-Ln)

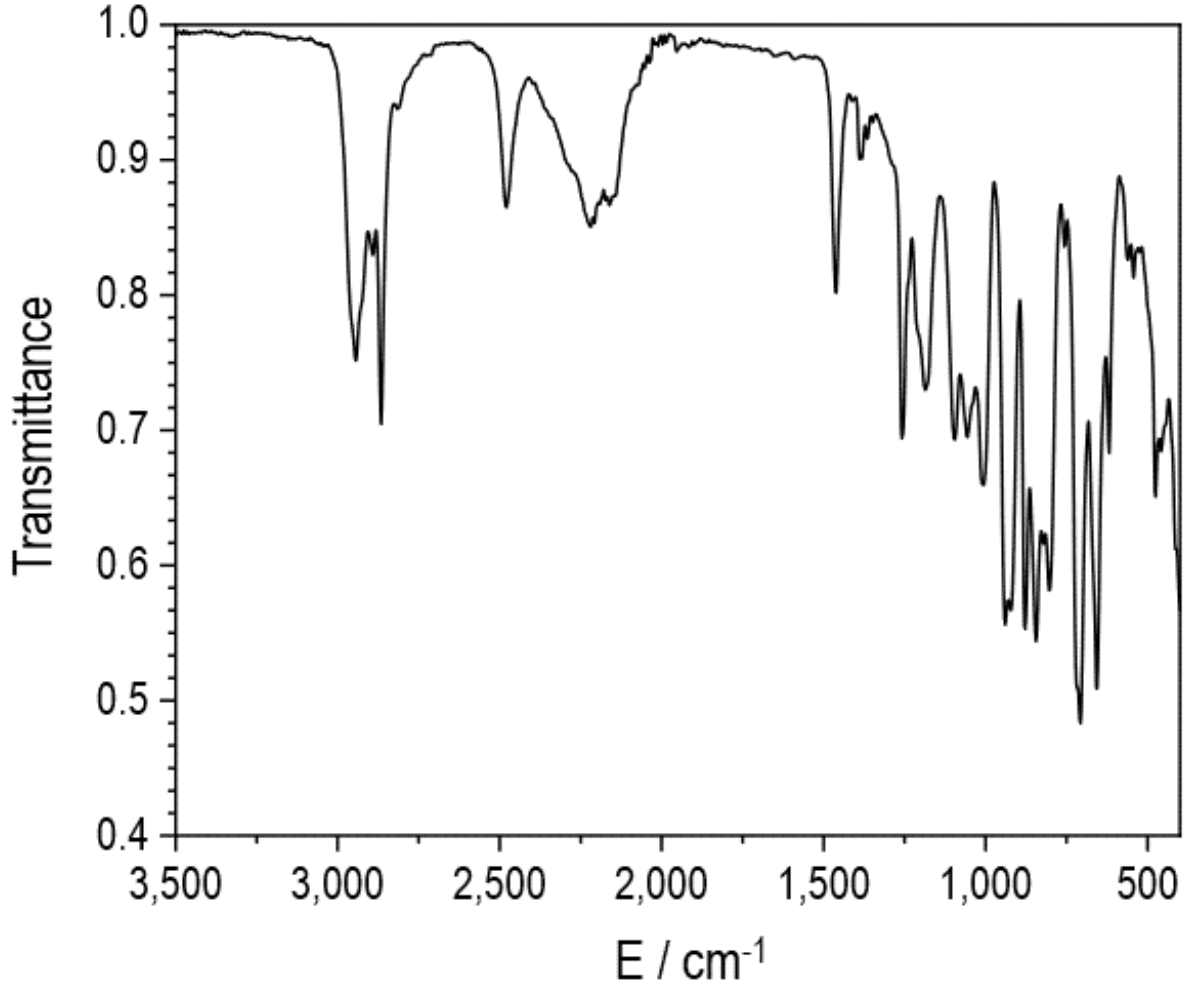

Figure S51. FT-IR (ATR, microcrystalline solid) spectrum of **2-Y** at ambient temperature.

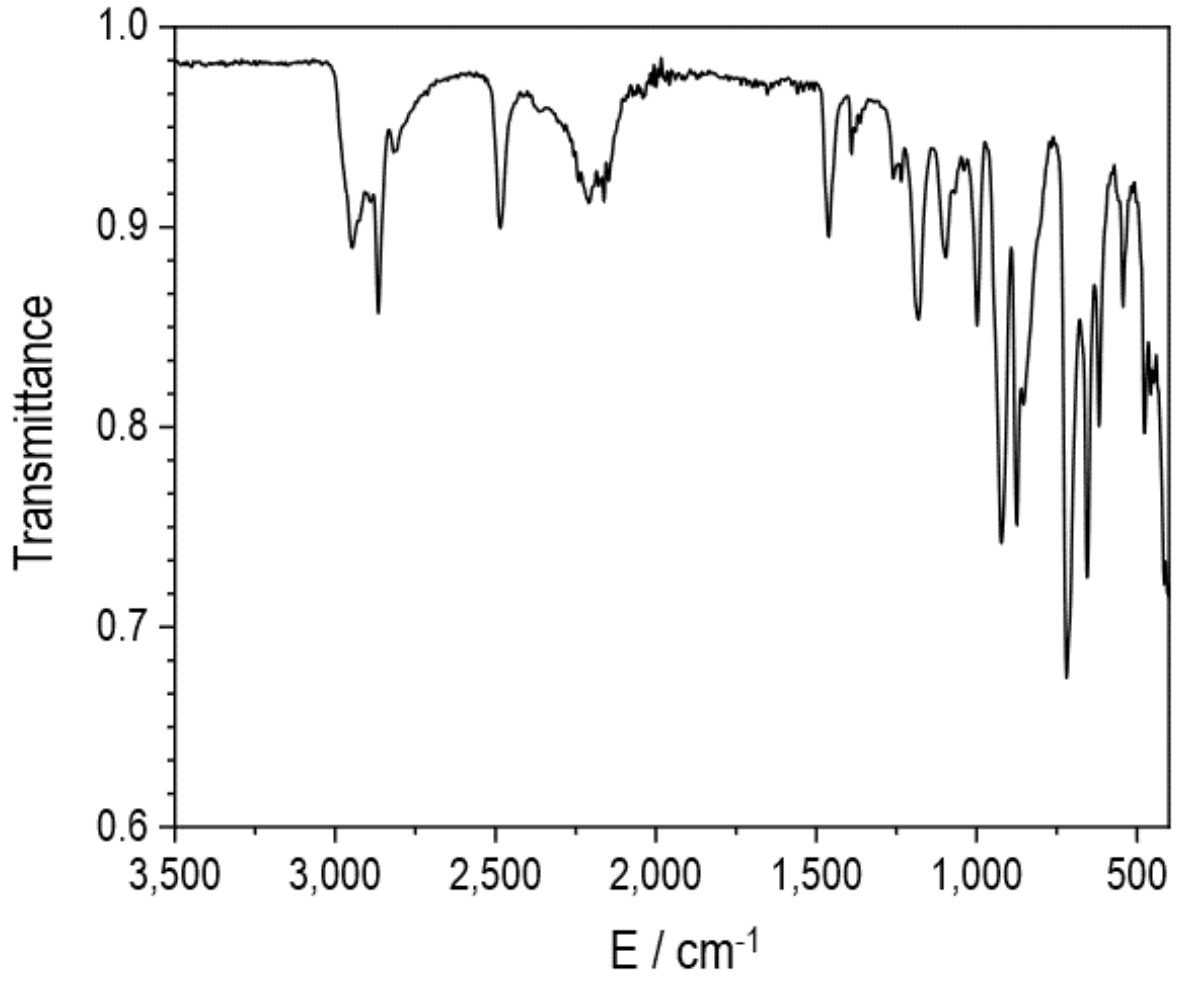

Figure S52. FT-IR (ATR, microcrystalline solid) spectrum of **2-Dy** at ambient temperature.

3.3 [Ln{N(Si^{i}Pr$_3$)$_2$}(BH$_4$)(μ-BH$_4$)]$_4$ (3-Ln)

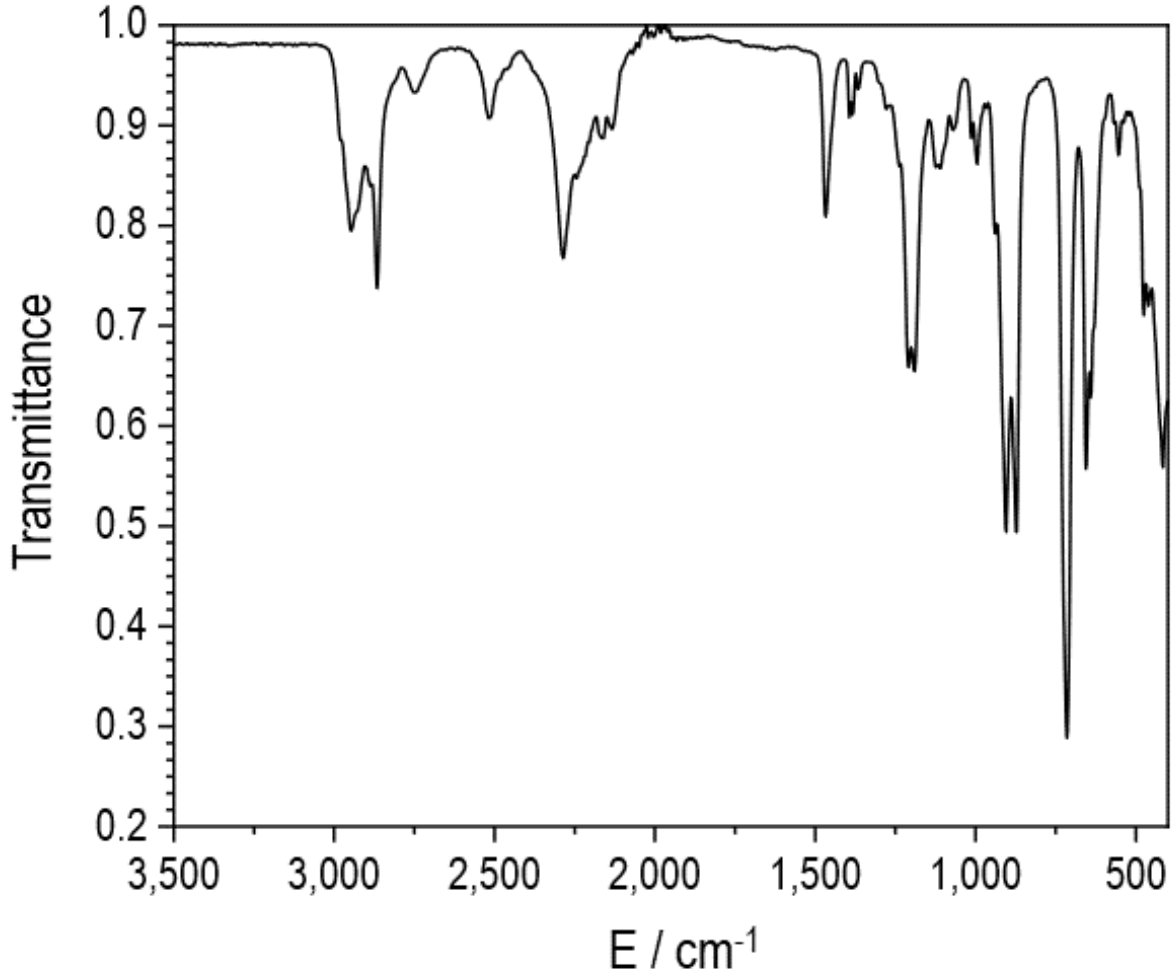

Figure S53. FT-IR (ATR, microcrystalline solid) spectrum of **3-Y** at ambient temperature.

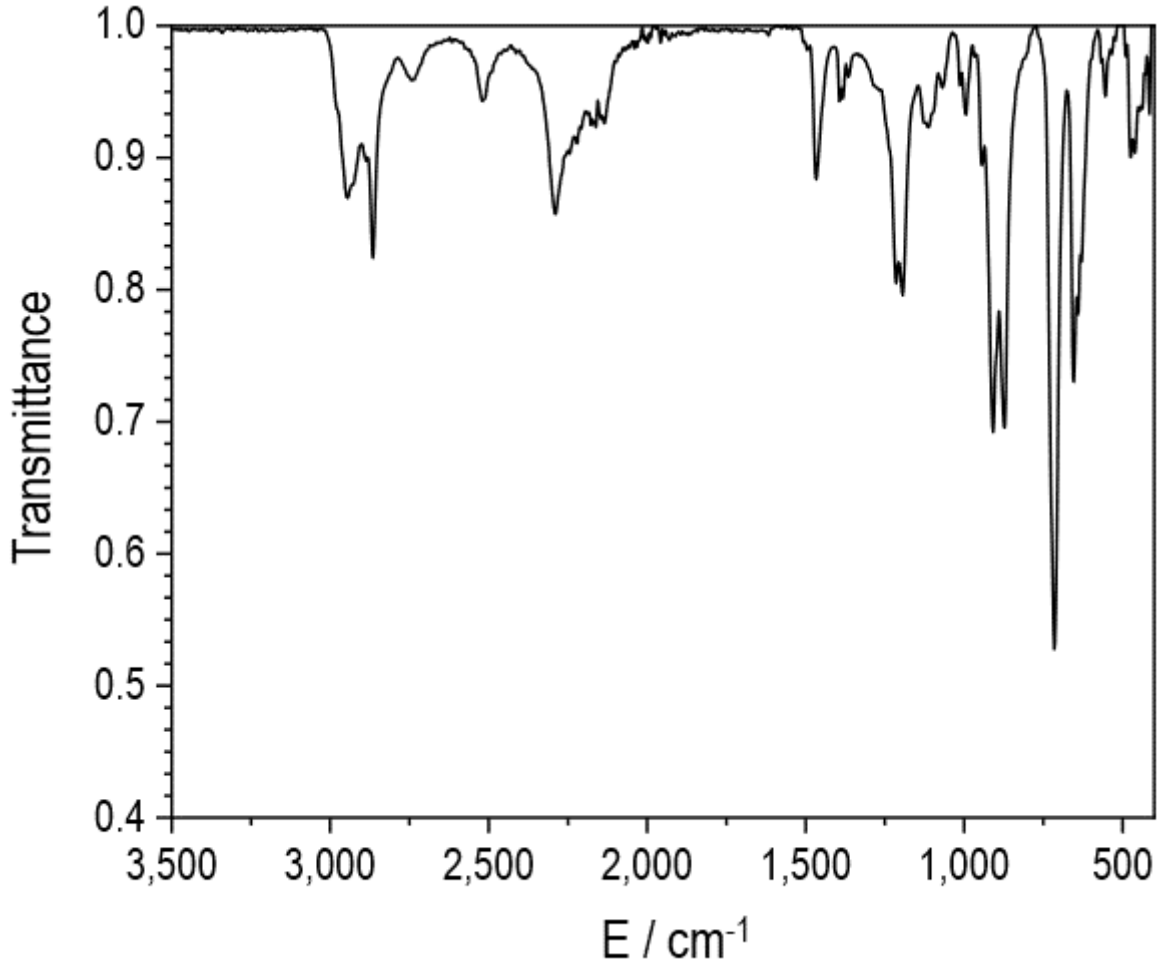

Figure S54. FT-IR (ATR, microcrystalline solid) spectrum of **3-Dy** at ambient temperature.

3.4 [Ln{N(Si^{i}Pr$_3$)$_2$}$_2$(BH$_4$)] (4-Ln)

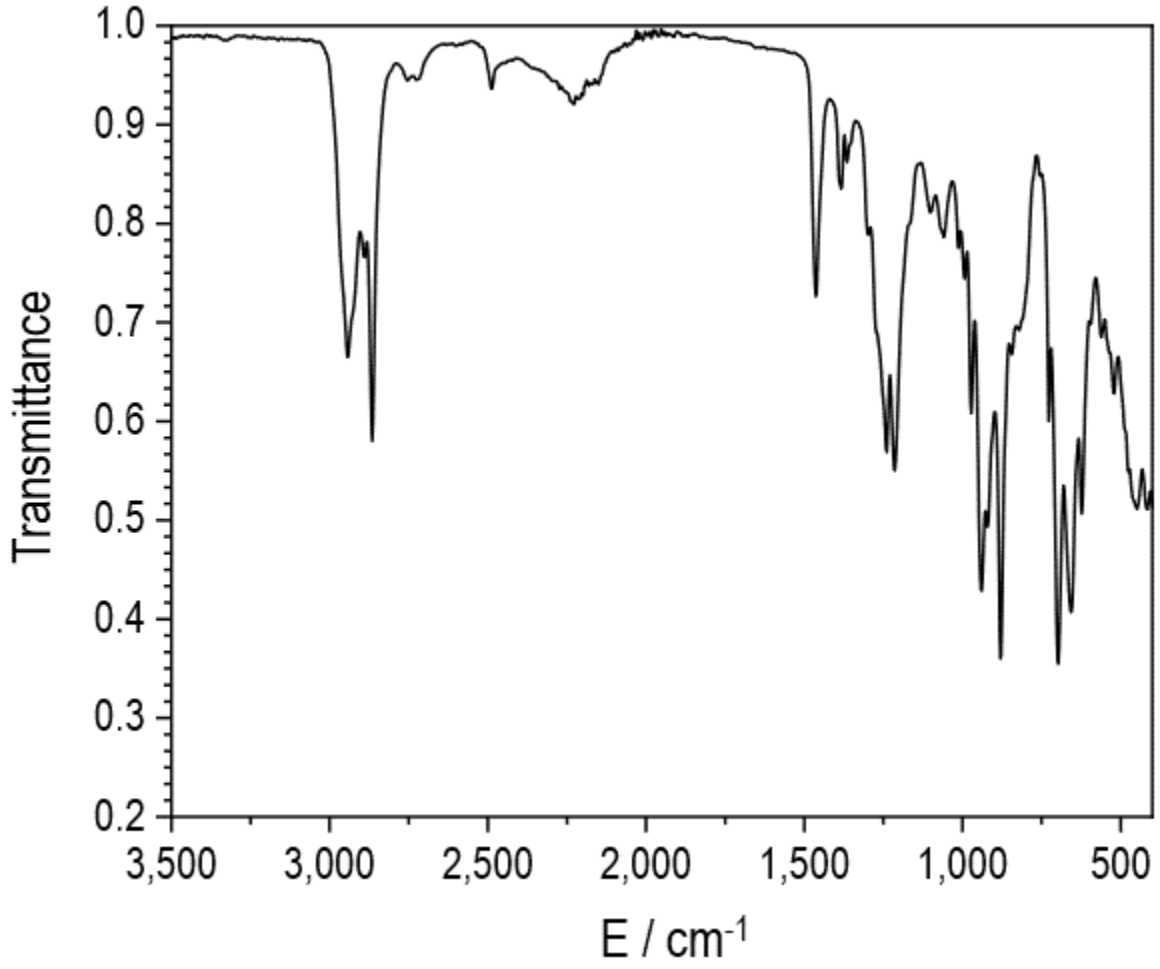

Figure S55. FT-IR (ATR, microcrystalline solid) spectrum of **4-Y** at ambient temperature.

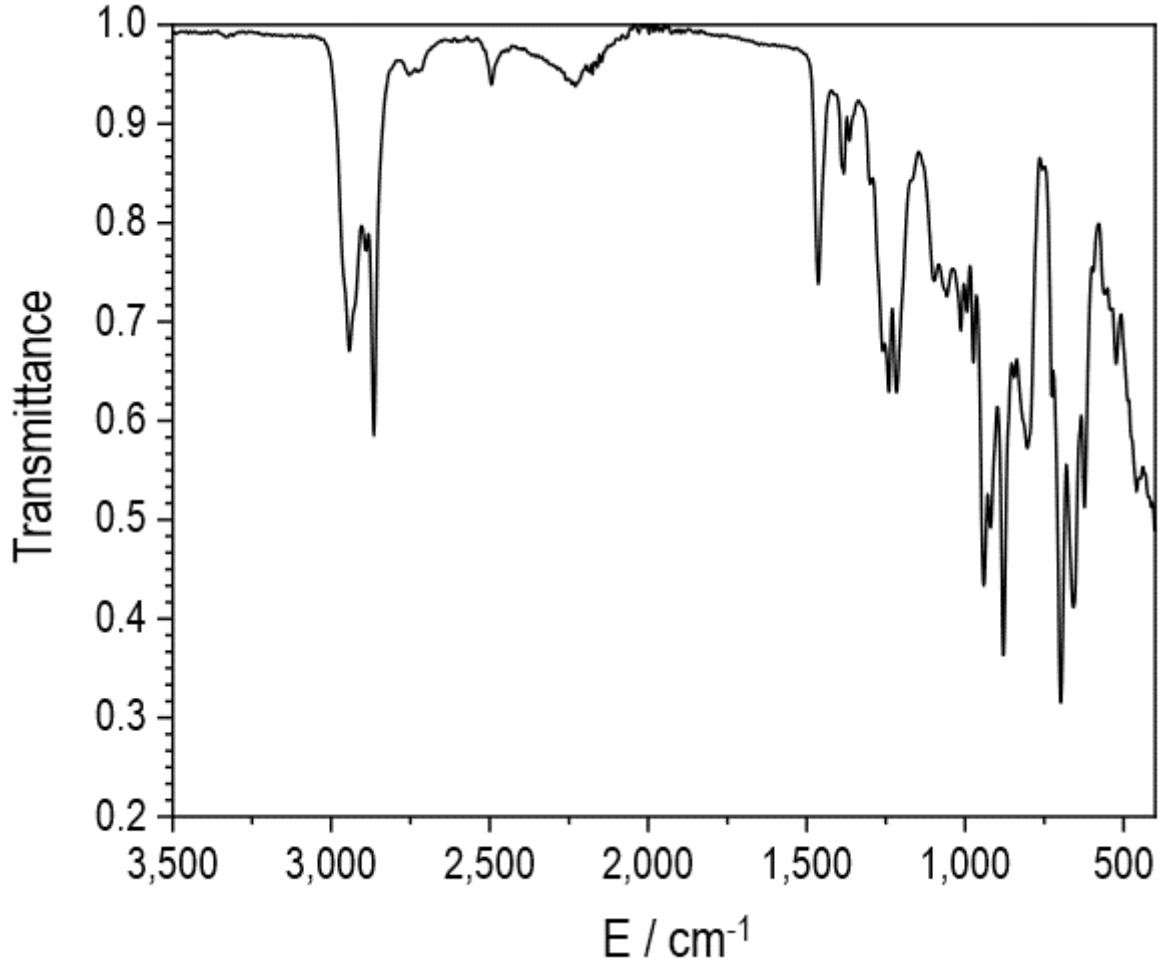

Figure S56. FT-IR (ATR, microcrystalline solid) spectrum of **4-Dy** at ambient temperature.

4. DFT calculated IR spectra

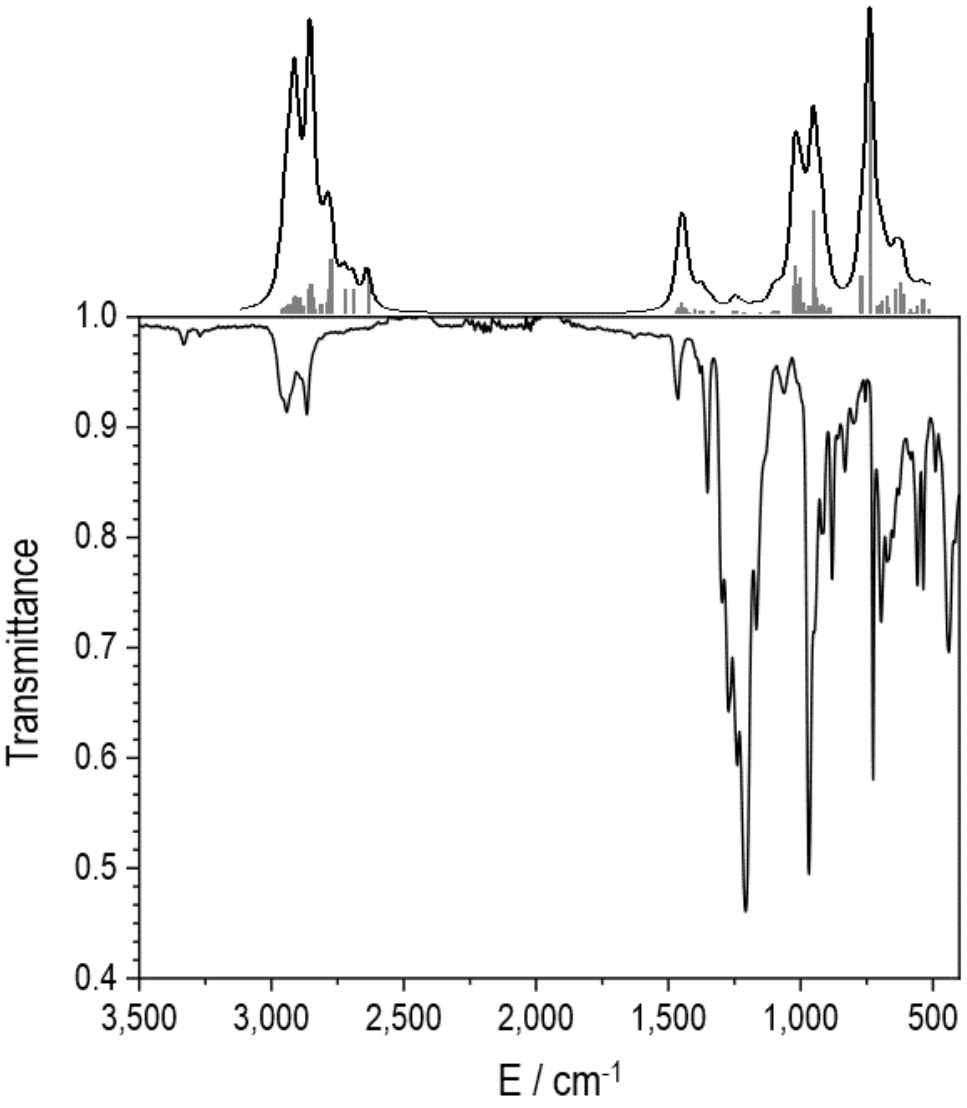

Figure S57. Comparison of the DFT-calculated IR spectrum of the cation of **1-Y** (top) with the experimentally derived spectra of **1-Y** at ambient temperature (bottom). A Lorentzian convolution (full width half maximum = 40 cm^{-1}) is applied to all calculated vibrational modes.

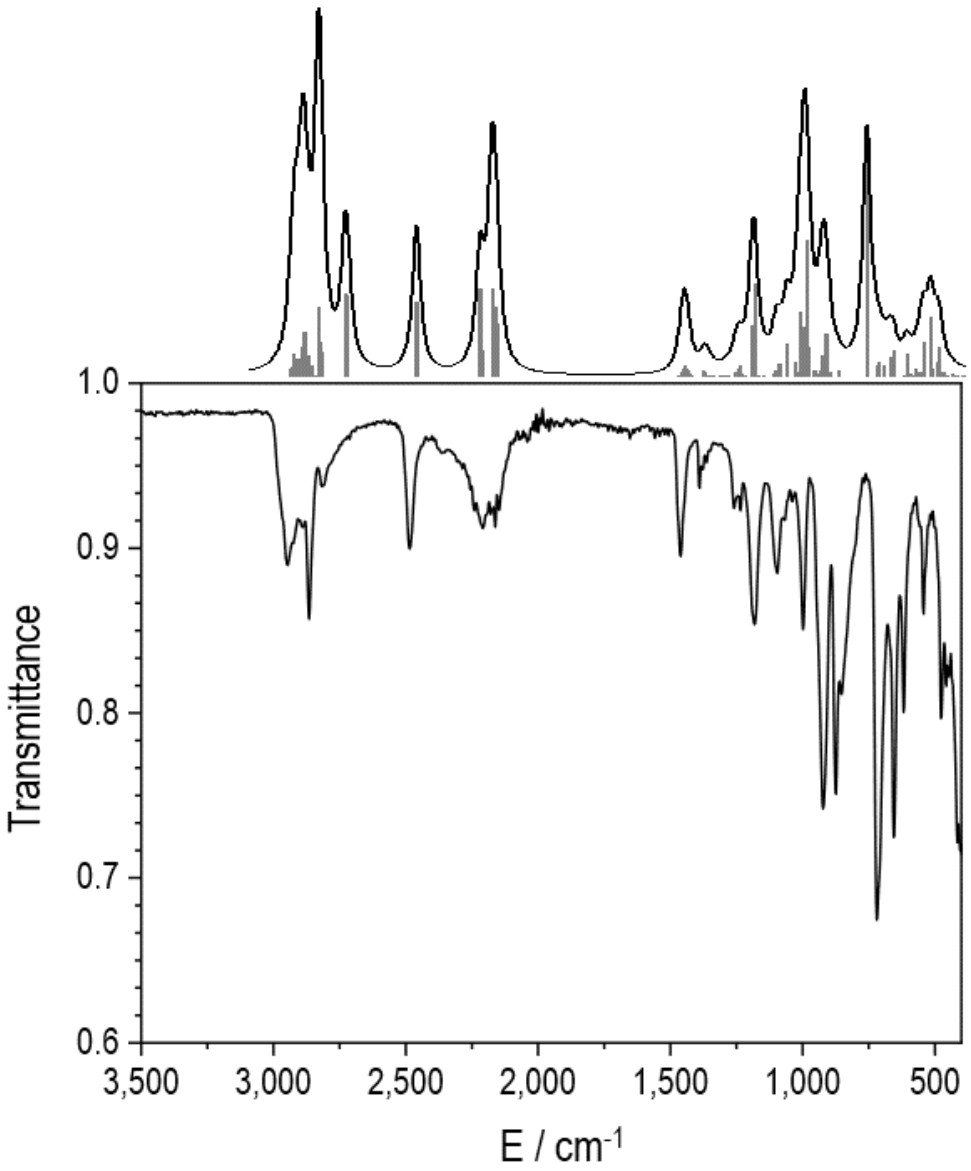

Figure S58. Comparison of the DFT-calculated IR spectrum of **2-Y** (top) with the experimentally derived spectra of **2-Y** at ambient temperature (bottom). A Lorentzian convolution (full width half maximum = 40 cm^{-1}) is applied to all calculated vibrational modes.

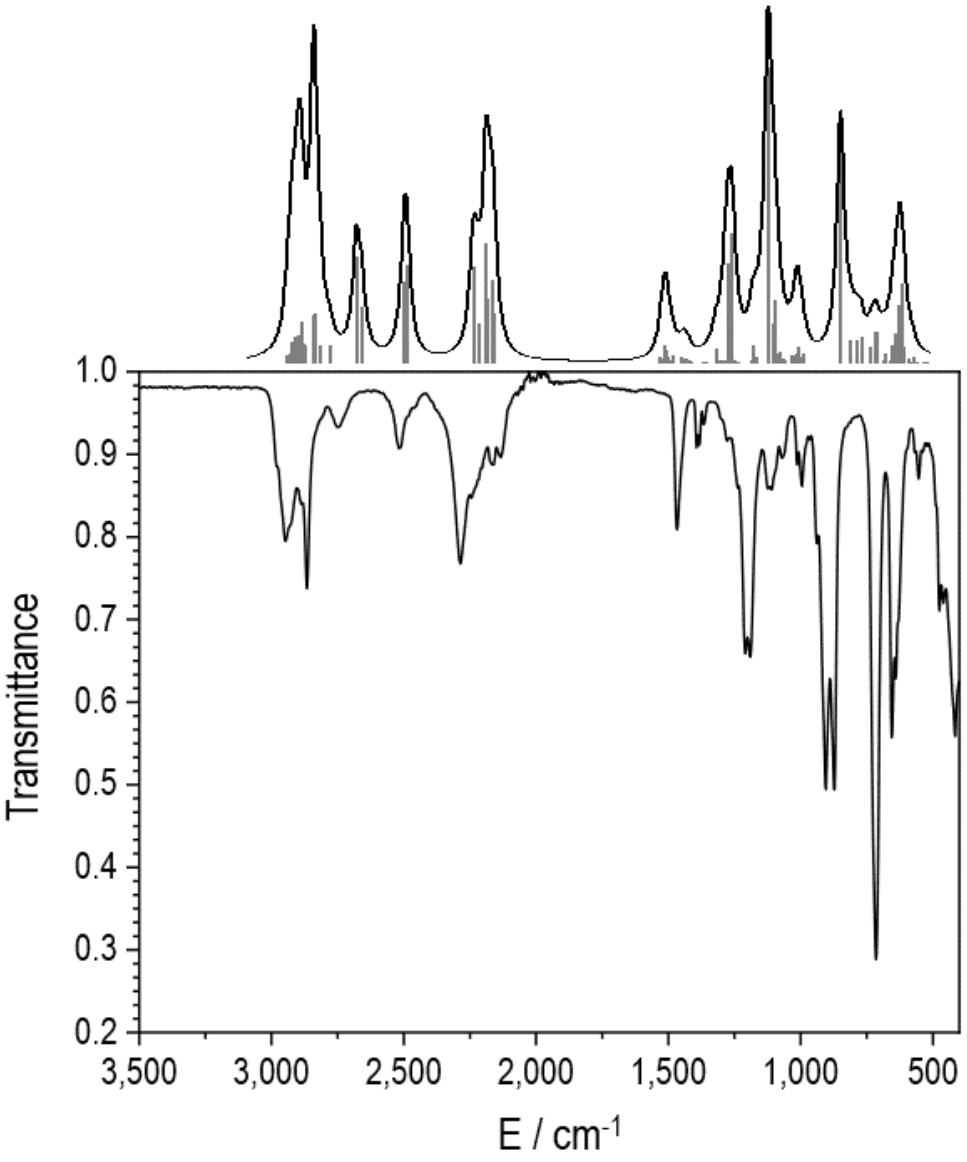

Figure S59. Comparison of the DFT-calculated IR spectrum of a monomer of **3-Y** (top) with the experimentally derived spectra of **3-Y** at ambient temperature (bottom). A Lorentzian convolution (full width half maximum = 40 cm^{-1}) is applied to all calculated vibrational modes.

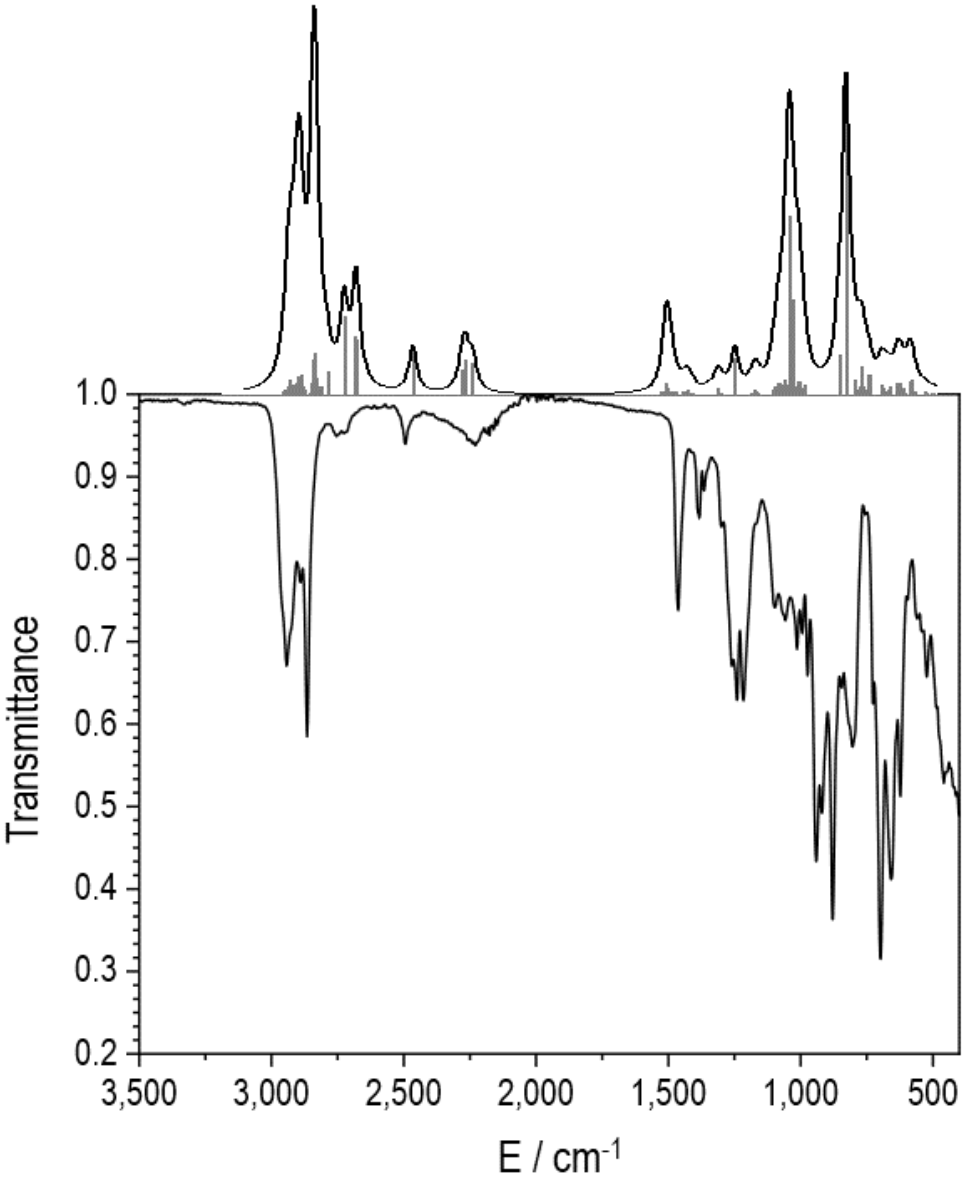

Figure S60. Comparison of the DFT-calculated IR spectrum of **4-Y** (top) with the experimentally derived spectra of **4-Y** at ambient temperature (bottom). A Lorentzian convolution (full width half maximum = 40 cm^{-1}) is applied to all calculated vibrational modes.

5. Single crystal X-ray diffraction

Table S1. Crystallographic data for **1-Ln** and **2-Ln**.

	1-Y	**1-Dy**	**2-Y**	**2-Dy**
Formula	$C_{52}H_{84}AlF_{36}N_2O_4Si_4Y$	$C_{52}H_{84}AlDyF_{36}N_2O_4Si_4$	$C_{22}H_{58}B_2NOSi_2Y$	$C_{22}H_{58}B_2DyNOSi_2$
Fw	1713.46	1787.05	519.40	592.99
Crystal size, mm	0.344 × 0.25 × 0.157	0.141 × 0.093 × 0.009	0.37 × 0.079 × 0.03	0.647 × 0.208 × 0.169
Crystal system	orthorhombic	orthorhombic	monoclinic	orthorhombic
Space group	*P*bca	*P*bca	$P2_1/c$	$P2_12_12_1$
Collection temperature, K	100(2)	100(2)	100(2)	100.00(10)
a, Å	19.4403(5)	19.4972(5)	8.8125(2)	13.0581(2)
b, Å	23.6130(9)	23.6772(8)	14.6779(3)	13.3893(2)
c, Å	31.6874(7)	31.7746(8)	23.0295(5)	16.8519(3)
α, °	90	90	90	90
β, °	90	90	92.139(2)	90
γ, °	90	90	90	90
V, Å^3	14545.9(8)	14668.4(7)	2976.77(11)	2946.37(8)
Z	8	8	4	4
ρ_{calcd}, g cm^{-3}	1.565	1.618	1.159	1.337
μ, mm^{-1}	1.014	7.418	3.603	2.630
No. of reflections made	76726	51591	18752	23774
No. of unique reflns, R_{int}	17384, 0.0982	9214, 0.0965	5985, 0.0323	6986, 0.0303
No. of reflns with $F^2 > 2\sigma(F^2)$	10292	7179	5517	6605
Transmn coeff range	0.08940-1.00000	0.462-1.000	0.737-1.000	0.648-1.000
R, R_w[a] ($F^2 > 2\sigma(F^2)$)	0.0579, 0.1020	0.0574, 0.1518	0.0339, 0.0990	0.0211, 0.0404
R, R_w[a] (all data)	0.1281, 0.1243	0.0743, 0.1647	0.0363, 0.1004	0.0239, 0.0417
S[a]	1.012	0.985	1.116	1.047
Parameters, Restraints	1289, 5001	1043, 1624	310, 0	317, 49
Max., min. diff map, e Å^{-3}	0.762, –0.499	1.143, –1.806	0.550, –1.365	0.557, –0.431

[a] Conventional $R = \Sigma||F_o| - |F_c||/\Sigma|F_o|$; $R_w = [\Sigma w(F_o^2 - F_c^2)^2/\Sigma w(F_o^2)^2]^{1/2}$; $S = [\Sigma w(F_o^2 - F_c^2)^2/\text{no. data} - \text{no. params})]^{1/2}$ for all data.

Table S2. Crystallographic data for **3-Ln** and **3-Ln·0.5KBH$_4$**.

	3-Y	**3-Dy**	**3-Y·0.5KBH$_4$·C$_6$H$_6$**	**3-Dy·0.5KBH$_4$·1,2-C$_6$H$_4$F$_2$**
Formula	$C_{72}H_{200}B_8N_4Si_8Y_4$	$C_{72}H_{200}B_8Dy_4N_4Si_8$	$C_{39}H_{107}B_5KN_2Si_4Y_2$	$C_{39}H_{105}B_5Dy_2FKN_2Si_4$
Fw	1789.19	2083.55	987.59	1151.75
Crystal size, mm	0.118 × 0.088 × 0.029	0.048 × 0.029 × 0.018	0.195 × 0.087 × 0.041	0.227 × 0.113 × 0.102
Crystal system	monoclinic	monoclinic	triclinic	Triclinic
Space group	$P2_1/c$	$P2_1/c$	P-1	P-1
Collection temperature, K	100(2)	100.01(15)	100(2)	100(2)
a, Å	18.0513(2)	17.9951(16)	8.56937(5)	8.5475(2)
b, Å	28.9661(3)	28.790(3)	18.02045(9)	18.0650(5)
c, Å	21.0674(2)	20.982(3)	18.50778(7)	18.4576(7)
α, °	90	90	89.5896(4)	91.009(3)
β, °	109.8967(13)	109.999(13)	82.7373(4)	98.027(3)
γ, °	90	90	86.5114(4)	93.085(2)
V, Å^3	10358.1(2)	10214(2)	2829.86(2)	2817.12(15)
Z	4	4	2	2
ρ_{calcd}, g cm^{-3}	1.147	1.355	1.159	1.358
μ, mm^{-1}	4.039	16.533	4.383	2.820
No. of reflections made	136906	16460	46757	24819
No. of unique reflns, R_{int}	21445, 0.0558	8302, 0.0972	11540, 0.0251	12813, 0.0347
No. of reflns with $F^2 > 2\sigma(F^2)$	18368	4715	10918	9853
Transmn coeff range	0.887-1.000	0.04783-1.00000	0.608-1.000	0.622-1.000
R, R_w[a] ($F^2 > 2\sigma(F^2)$)	0.0520, 0.1375	0.0738, 0.1793	0.0234, 0.0615	0.0338, 0.0603
R, R_w[a] (all data)	0.0590, 0.1419	0.1453, 0.2084	0.0248, 0.0622	0.0557, 0.0674
S[a]	1.078	0.898	1.075	0.983
Parameters, Restraints	1119, 412	961, 1616	682, 363	699, 1049
Max., min. diff map, e Å^{-3}	0.935, –1.908	1.728, –0.722	0.403, –0.474	1.427, –0.954

[a] Conventional $R = \Sigma||F_o| - |F_c||/\Sigma|F_o|$; $R_w = [\Sigma w(F_o^2 - F_c^2)^2/\Sigma w(F_o^2)^2]^{1/2}$; $S = [\Sigma w(F_o^2 - F_c^2)^2/\text{no. data} - \text{no. params})]^{1/2}$ for all data.

Table S3. Crystallographic data for **4-Ln**.

	4-Y[b]	**4-Y**[c]	**4-Dy**
Formula	$C_{36}H_{88}BN_2Si_4Y$	$C_{36}H_{88}BN_2Si_4Y$	$C_{36}H_{88}BDyN_2Si_4$
Fw	761.16	761.16	834.75
Crystal size, mm	0.205 × 0.184 × 0.103	0.086 × 0.071 × 0.022	0.171 × 0.127 × 0.054
Crystal system	monoclinic	orthorhombic	orthorhombic
Space group	$P2_1/c$	*P*bca	*P*bca
Collection temperature, K	100(2)	100(2)	100(2)
a, Å	15.9332(13)	20.3776(3)	20.3179(5)
b, Å	13.1915(8)	20.0917(4)	19.9900(5)
c, Å	22.5401(14)	21.6614(4)	21.7278(4)
α, °	90	90	90
β, °	108.911(8)	90	90
γ, °	90	90	90
V, Å^3	4481.8(6)	8868.6(3)	8824.9(3)
Z	4	8	8
ρ_{calcd}, g cm^{-3}	1.128	1.140	1.257
μ, mm^{-1}	1.433	3.055	10.268
No. of reflections made	22250	47249	51634
No. of unique reflns, R_{int}	9146, 0.0578	9116, 0.0566	7995, 0.0790
No. of reflns with $F^2 > 2\sigma(F^2)$	6307	7675	6169
Transmn coeff range	0.719-1.000	0.912-1.000	0.69935-1.00000
R, R_w[a] ($F^2 > 2\sigma(F^2)$)	0.0496, 0.0845	0.0389, 0.0997	0.0474, 0.1084
R, R_w[a] (all data)	0.0928, 0.0974	0.0473, 0.1041	0.0677, 0.1169
S[a]	1.004	0.999	1.031
Parameters, Restraints	473, 164	516, 1314	492, 329
Max., min. diff map, e Å^{-3}	0.442, –0.434	0.591, –1.147	2.149, –1.182

[a] Conventional $R = \Sigma||F_o| - |F_c||/\Sigma|F_o|$; $R_w = [\Sigma w(F_o^2 - F_c^2)^2/\Sigma w(F_o^2)^2]^{1/2}$; $S = [\Sigma w(F_o^2 - F_c^2)^2/\text{no. data} - \text{no. params})]^{1/2}$ for all data. [b] Polymorph in $P2_1/c$. [c] Polymorph in *P*bca.

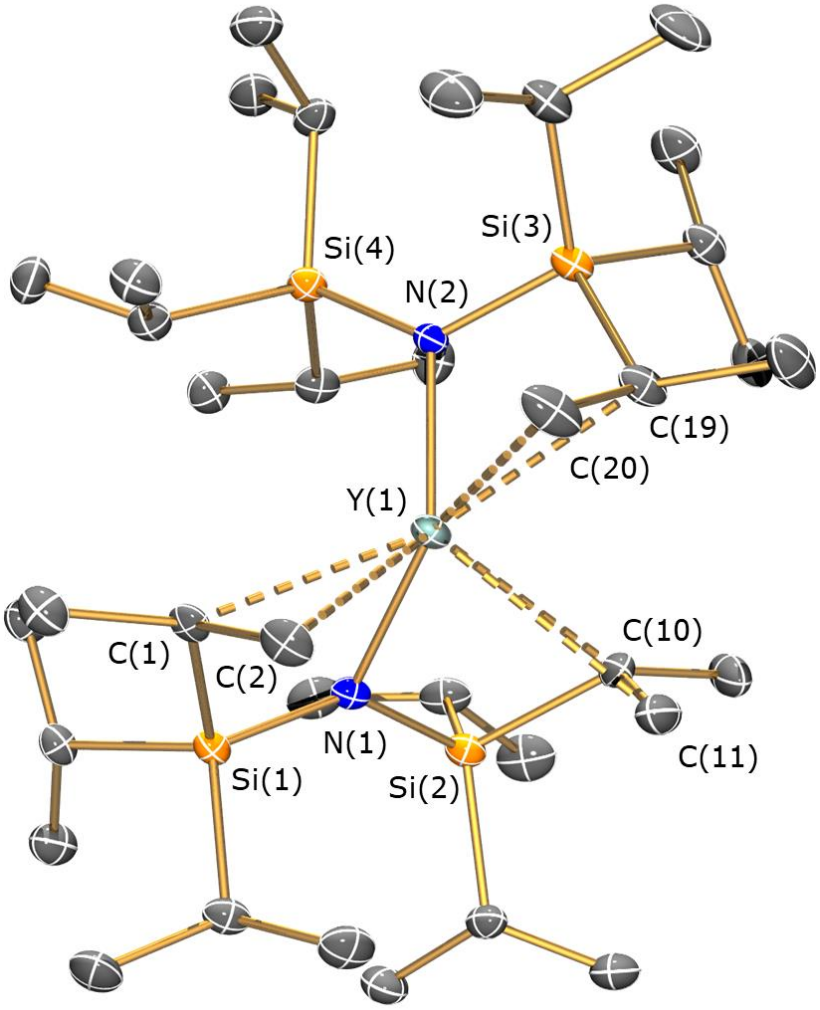

Figure S61. Solid-state crystal structure of the cation of **1-Y** at 100(2) K. Displacement ellipsoids set at 50% probability level. Hydrogen atoms and $[Al\{OC(CF_3)_3\}_4]^-$ counter-anion omitted for clarity. Selected bond distances (Å) and angles (°): Y(1)–N(1): 2.194(2); Y(1)–N(2): 2.182(3); Y(1)···C(1): 2.838(3); Y(1)···C(2): 2.962(3); Y(1)···C(10): 2.852(4); Y(1)···C(11): 3.010(4); Y(1)···C(19): 2.826(3); Y(1)···C(20): 2.872(3); Y(1)···Si(1): 3.2023(9); Y(1)···Si(2): 3.2108(11); Y(1)···Si(3): 3.1822(9); N(1)–Y(1)–N(2): 126.70(9).

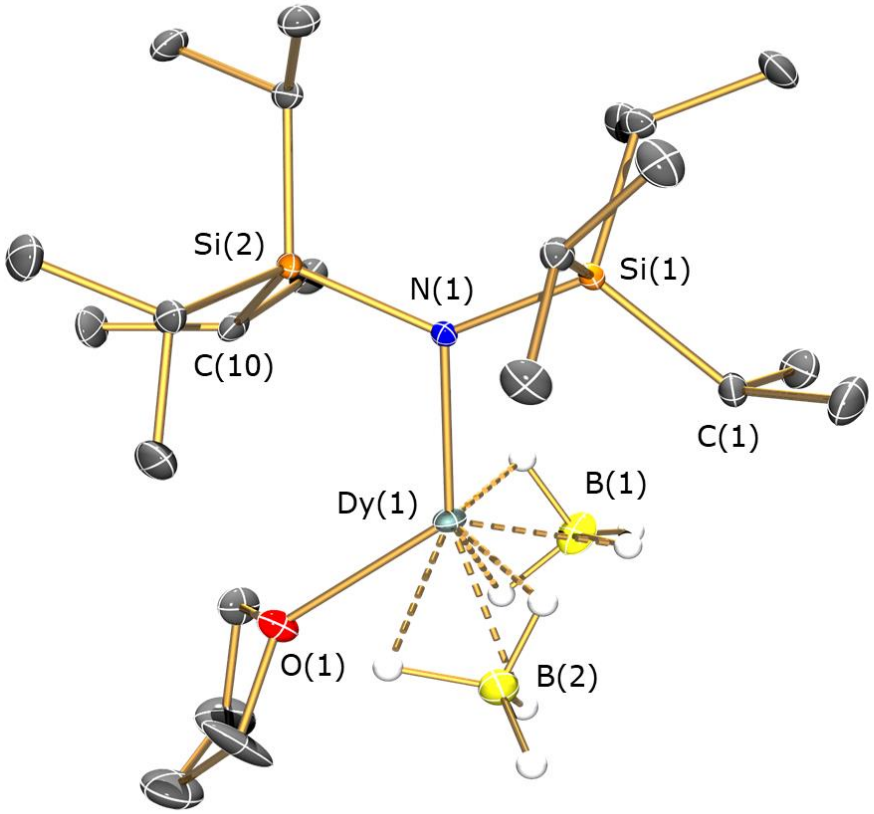

Figure S62. Solid-state crystal structure of [Dy{N(Si^{i}Pr$_3$)$_2$}(BH$_4$)$_2$(THF)] (**2-Dy**) at 100(2) K. Displacement ellipsoids set at 50% probability level. Non-borohydride hydrogen atoms omitted for clarity. Selected bond distances (Å) and angles (°): Dy(1)–N(1): 2.211(2); Dy(1)···B(1): 2.498(5); Dy(1)···B(2): 2.516(5); Dy(1)–O(1): 2.367(2); Dy(1)···C(1): 3.370(3); Dy(1)···C(10): 3.341(3); Dy(1)···Si(1): 3.3768(8); Dy(1)···Si(2): 3.3404(8); N(1)–Dy(1)···B(1): 112.00(16); N(1)–Dy(1)···B(2): 115.64(16); N(1)–Dy(1)–O(1): 127.22(8); B(1)···Dy(1)···B(2): 113.82(14); B(1)···Dy(1)–O(1): 93.68(15); B(2)···Dy(1)–O(1): 91.85(15).

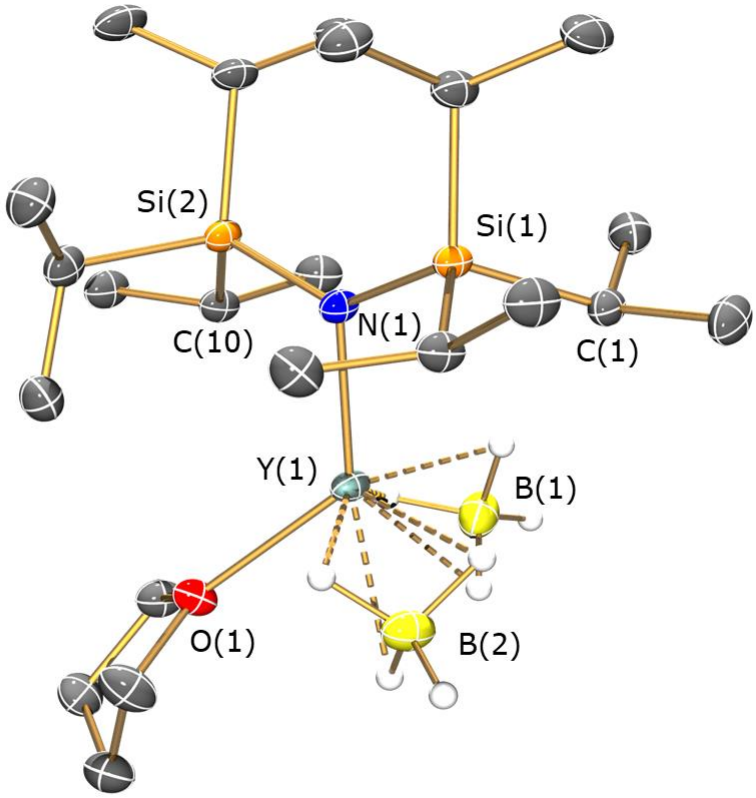

Figure S63. Solid-state crystal structure of [Y{N(Si^{i}Pr$_3$)$_2$}(BH$_4$)$_2$(THF)] (**2-Y**) at 100(2) K. Displacement ellipsoids set at 50% probability level. Non-borohydride hydrogen atoms and minor disordered THF component omitted for clarity. Selected bond distances (Å) and angles (°): Y(1)–N(1): 2.254(2); Y(1)···B(1): 2.484(3); Y(1)···B(2): 2.484(3); Y(1)–O(1): 2.3449(13); Y(1)···C(1): 3.6506(19); Y(1)···C(10): 3.1241(19); Y(1)···Si(1): 3.4356(5); Y(1)···Si(2): 3.2404(5); N(1)–Y(1)···B(1): 118.95(8); N(1)–Y(1)···B(2): 107.89(7); N(1)–Y(1)–O(1): 128.21(6); B(1)···Y(1)···B(2): 109.13(9); B(1)···Y(1)–O(1): 95.31(8); B(2)···Y(1)–O(1): 94.02(7).

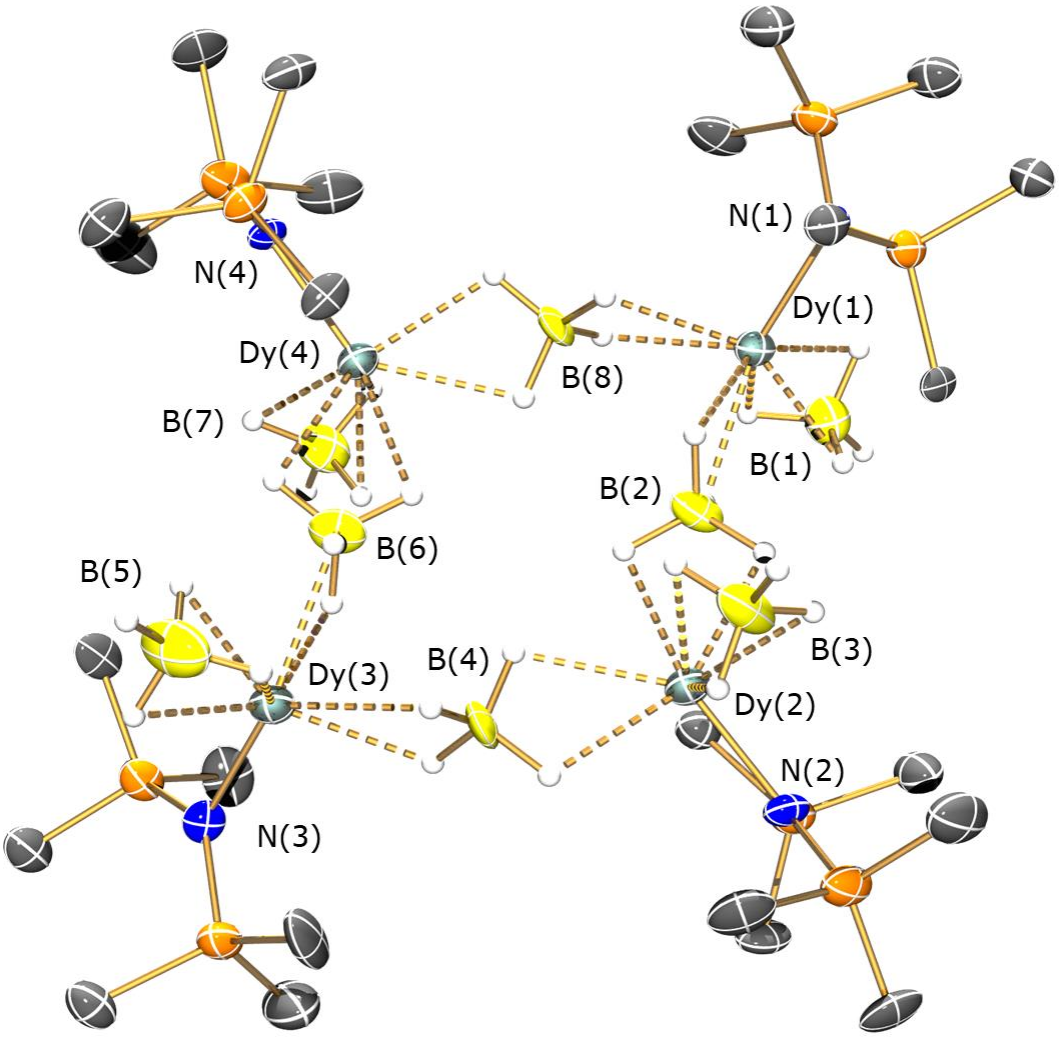

Figure S64. Solid-state crystal structure of $[Dy\{N(Si^iPr_3)_2\}(BH_4)_2]_4$ (**3-Dy**) at 100(2) K. Displacement ellipsoids set at 30% probability level. Non-borohydride hydrogen atoms and ^{i}Pr CH_3 carbon atoms omitted for clarity. Selected bond distances (Å) and angles (°): Dy(1)–N(1): 2.187(11); Dy(1)···B(1): 2.41(2); Dy(1)···B(2): 2.72(2); Dy(1)···B(8): 2.77(2); N(1)–Dy(1)···B(1): 116.6(6); N(1)–Dy(1)···B(2): 112.0(5); N(1)–Dy(1)···B(8): 126.0(5); B(1)···Dy(1)···B(2): 119.1(7); B(1)···Dy(1)···B(8): 99.1(8); B(2)···Dy(1)···B(8): 79.1(6).

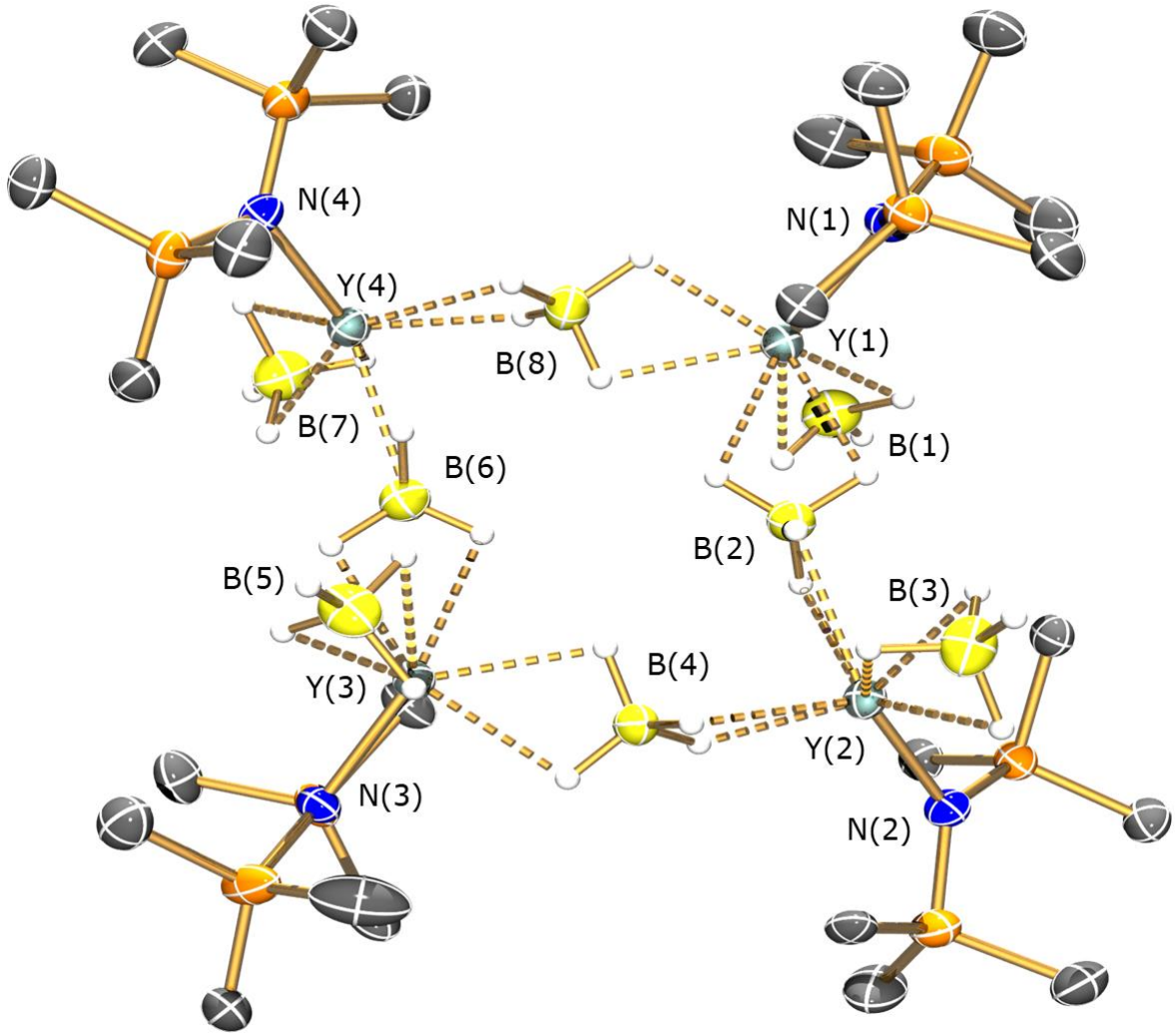

Figure S65. Solid-state crystal structure of $[Y\{N(Si^iPr_3)_2\}(BH_4)_2]_4$ (**3-Y**) at 100(2) K. Displacement ellipsoids set at 50% probability level. Non-borohydride hydrogen atoms and ^{i}Pr CH_3 carbon atoms omitted for clarity. Selected bond distances (Å) and angles (°): Y(1)–N(1): 2.183(3); Y(1)···B(1): 2.458(6); Y(1)···B(2): 2.785(5); Y(1)···B(8): 2.737(4); N(1)–Y(1)···B(1): 116.1(2); N(1)–Y(1)···B(2): 126.44(11); N(1)–Y(1)···B(8): 112.04(12); B(1)···Y(1)···B(2): 99.3(2); B(1)···Y(1)···B(8): 119.2(2); B(2)···Y(1)···B(8): 79.02(11).

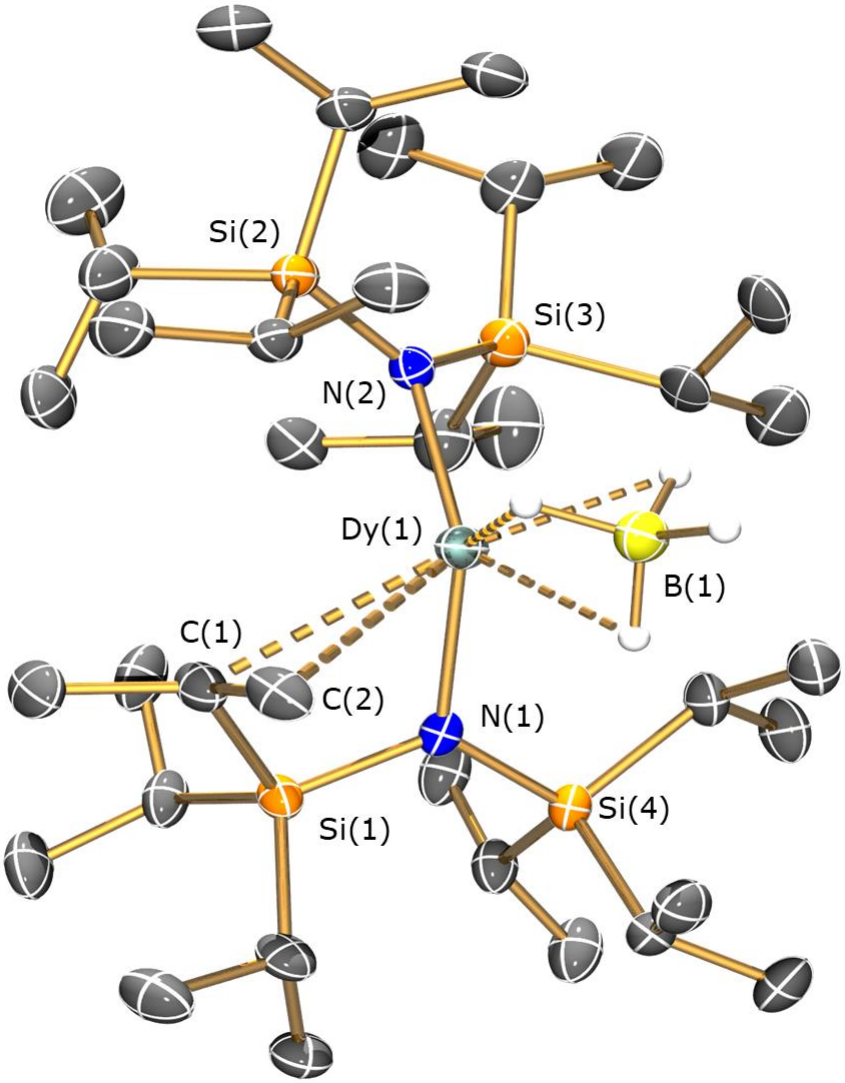

Figure S66. Solid-state crystal structure of [Dy{N(Si^{i}Pr$_3$)$_2$}$_2$(BH$_4$)] (**4-Dy**) at 100(2) K. Displacement ellipsoids set at 50% probability level. Non-borohydride hydrogen atoms and minor ^{i}Pr disordered components omitted for clarity. Selected bond distances (Å) and angles (°): Dy(1)–N(1): 2.266(4); Dy(1)–N(2): 2.288(4); Dy(1)···B(1): 2.483(6); Dy(1)–C(1): 2.989(4); Dy(1)–C(1): 3.128(4); Dy(1)–Si(1): 3.3152(11); Dy(1)–Si(2): 3.4092(12); Dy(1)–Si(3): 3.4072(13); Dy(1)–Si(4): 3.5734(11); N(1)–Dy(1)–N(2): 130.41(13); N(1)–Dy(1)···B(1): 112.40(15); N(2)–Dy(1)···B(1): 113.93(15).

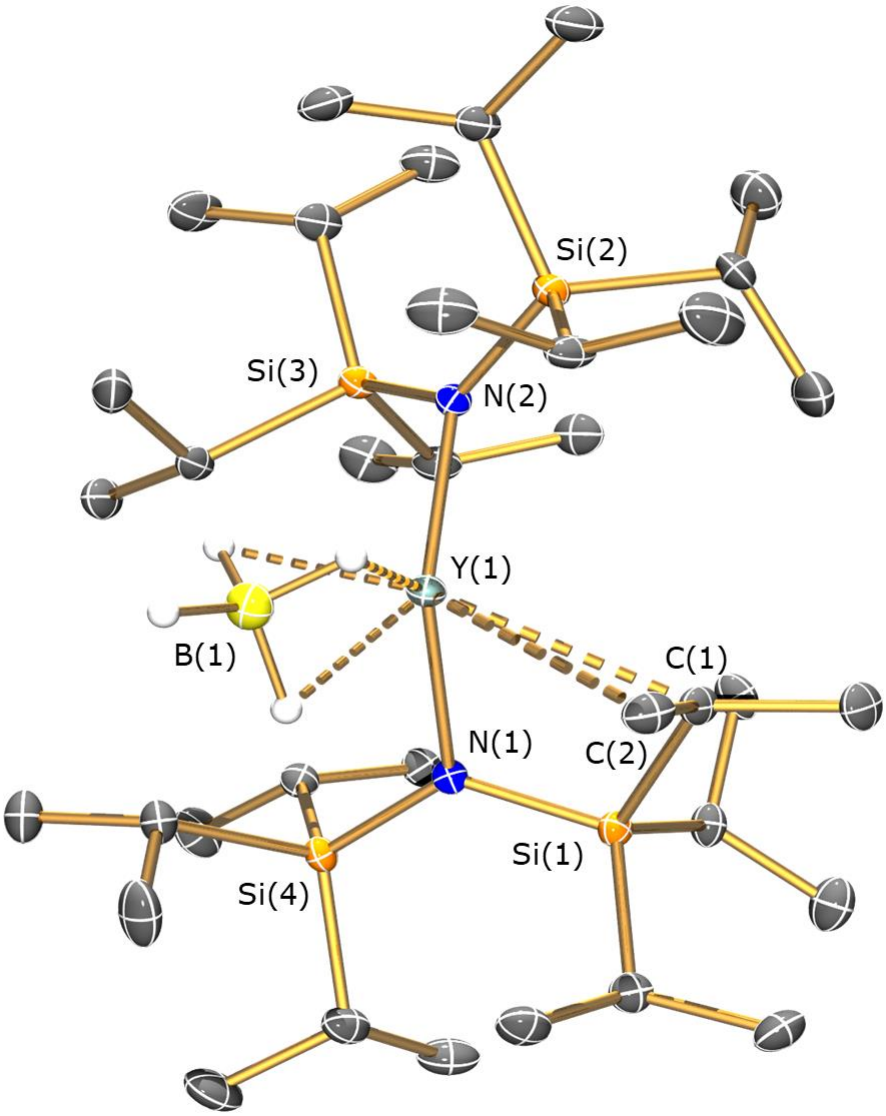

Figure S67. Solid-state crystal structure of the $P2_1/c$ polymorph of [Y{N(Si^{i}Pr$_3$)$_2$}$_2$(BH$_4$)] (**4-Y**) at 100(2) K. Displacement ellipsoids set at 50% probability level. Non-borohydride hydrogen atoms and minor ^{i}Pr disordered components omitted for clarity. Selected bond distances (Å) and angles (°): Y(1)–N(1): 2.251(2); Y(1)–N(2): 2.283(2); Y(1)···B(1): 2.483(5); Y(1)–C(1): 2.907(3); Y(1)–C(2): 3.078(3); Y(1)–Si(1): 3.2238(10); Y(1)–Si(2): 3.4025(9); Y(1)–Si(3): 3.4013(10); Y(1)–Si(4): 3.5618(9); N(1)–Y(1)–N(2): 127.36(8); N(1)–Y(1)···B(1): 110.02(11); N(2)–Y(1)···B(1): 116.58(11).

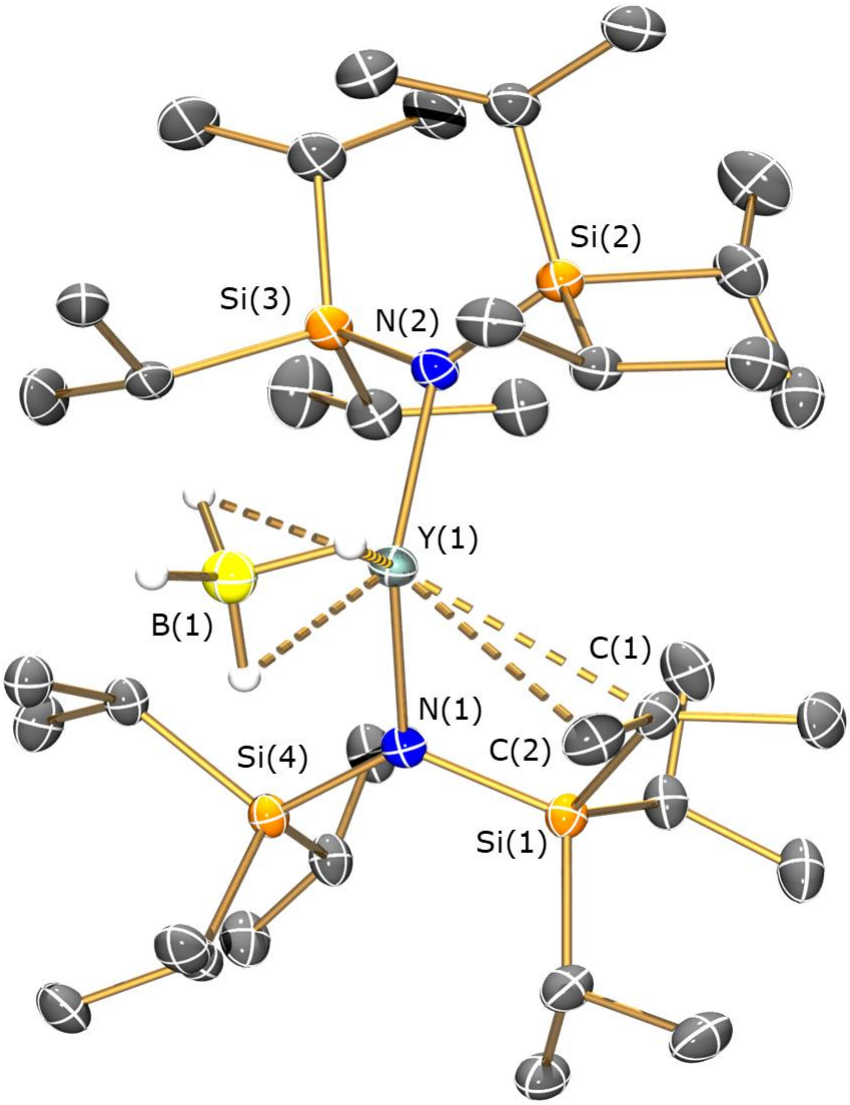

Figure S68. Solid-state crystal structure of the *P*bca polymorph of [Y{N(Si^{i}Pr$_3$)$_2$}$_2$(BH$_4$)] (**4-Y**) at 100(2) K. Displacement ellipsoids set at 50% probability level. Non-borohydride hydrogen atoms and minor ^{i}Pr disordered components omitted for clarity. Selected bond distances (Å) and angles (°): Y(1)–N(1): 2.288(2); Y(1)–N(2): 2.268(2); Y(1)···B(1): 2.493(3); Y(1)–C(1): 2.968(2); Y(1)–C(2): 3.104(2); Y(1)–Si(1): 3.3109(7); Y(1)–Si(2): 3.5865(7); Y(1)–Si(3): 3.4046(7); Y(1)–Si(4): 3.4206(6); N(1)–Y(1)–N(2): 128.20(7); N(1)–Y(1)···B(1): 113.15(8); N(2)–Y(1)···B(1): 114.72(8).

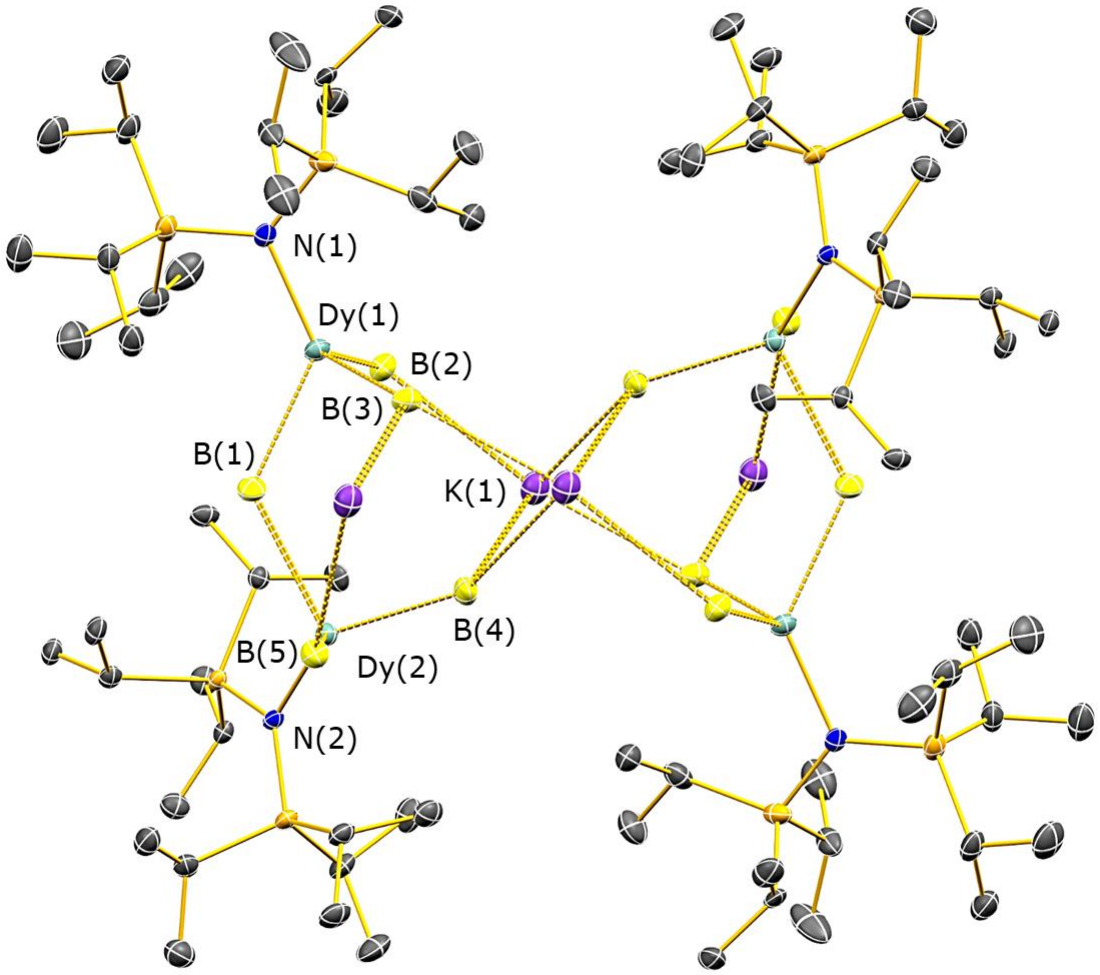

Figure S69. Solid-state crystal structure of a dimeric unit of polymeric $[\{Dy\{N(Si^iPr_3)_2\}(BH_4)(\mu\text{-}BH_4)\}_2\{K(\mu\text{-}BH_4)\}]_\infty \cdot 1,2\text{-}C_6H_4F_2$ (**3-Dy·0.5KBH$_4$·1,2-C$_6$H$_4$F$_2$**) at 100(2) K, viewed along the principal axis of the extended 1D coordination polymer. Displacement ellipsoids set at 50% probability level. All hydrogen atoms and co-crystallized $1,2\text{-}C_6H_4F_2$ omitted for clarity. Selected bond distances (Å): Dy(1)–N(1): 2.185(3); Dy(2)–N(2): 2.185(3); Dy(1)···B(1): 2.656(5); Dy(1)···B(2): 2.739(5); Dy(1)···B(3): 2.516(5); Dy(2)···B(1): 2.842(5); Dy(2)···B(4): 2.509(5); Dy(2)···B(5): 2.558(5); K(1)···B(2): 3.252(5); K(1)···B(4): 3.576(5).

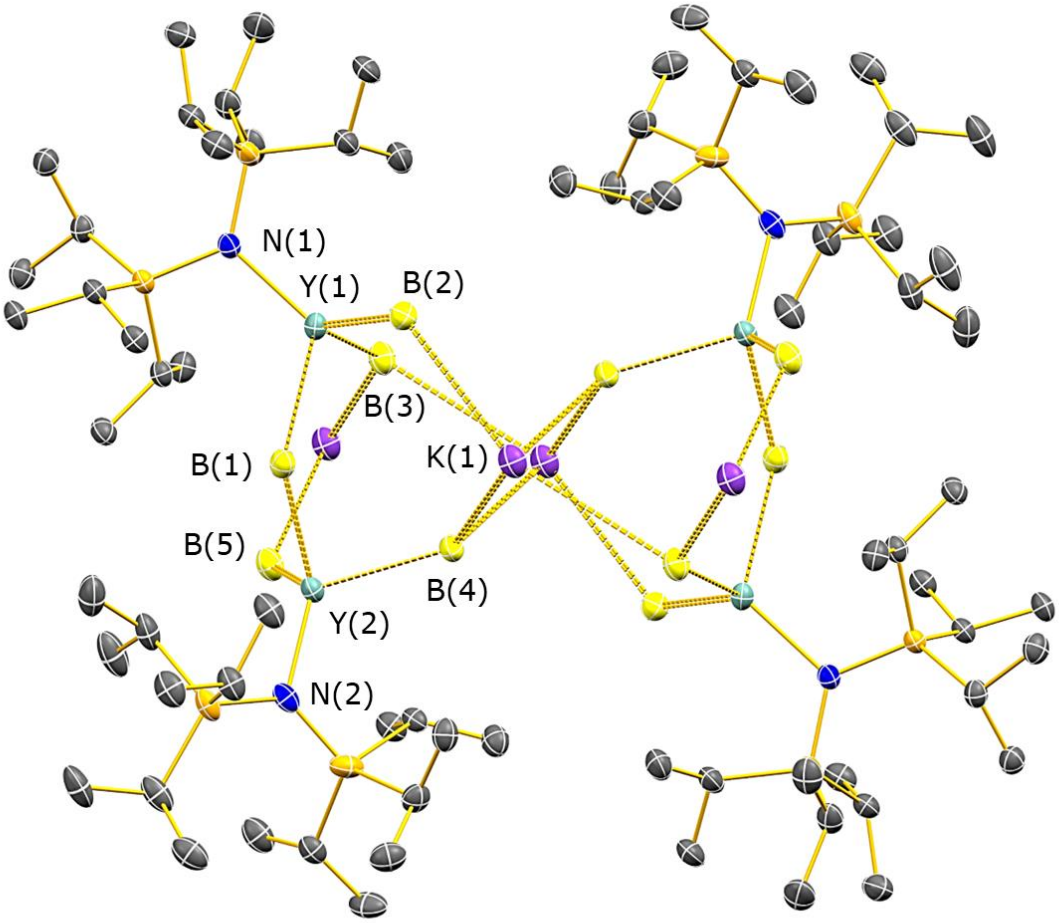

Figure S70. Solid-state crystal structure of a dimeric unit of polymeric $[\{Y\{N(Si^iPr_3)_2\}(BH_4)(\mu\text{-}BH_4)\}_2\{K(\mu\text{-}BH_4)\}]_\infty \cdot C_6H_6$ (**3-Y·0.5KBH$_4$·C$_6$H$_6$**) at 100(2) K, viewed along the principal axis of the extended 1D coordination polymer. Displacement ellipsoids set at 50% probability level. All hydrogen atoms and co-crystallized C_6H_6 omitted for clarity. Selected bond distances (Å): Y(1)–N(1): 2.1952(13); Y(2)–N(2): 2.2060(13); Y(1)···B(1): 2.650(2); Y(1)···B(2): 2.732(2); Y(1)···B(3): 2.506(2); Y(2)···B(1): 2.824(2); Y(2)···B(4): 2.550(2); Y(2)···B(5): 2.495(2); K(1)···B(2): 3.138(2); K(1)···B(2): 3.617(2).

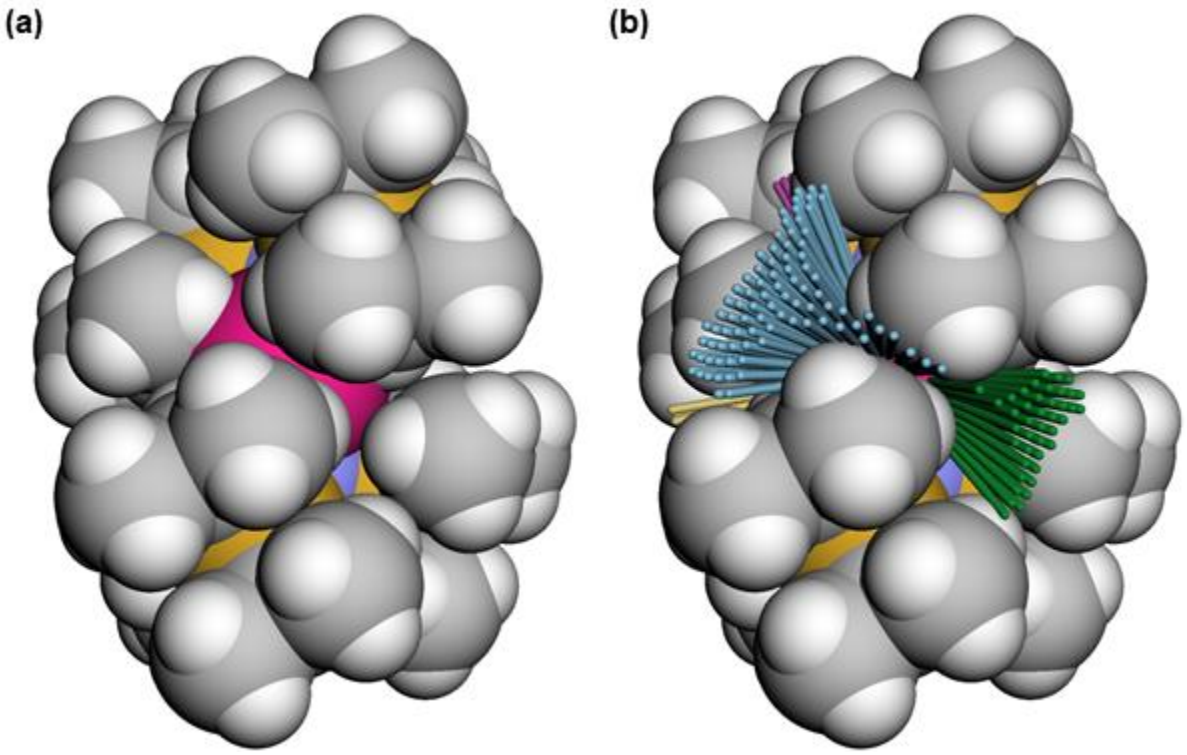

Figure S71. (a) Space-filling model of the cation of **1-Dy**. Color code: Dy (pink), silicon (gold), nitrogen (violet), carbon (grey) and hydrogen (white). (b) Using the *AtomAccess* program,[2] the accessibility of the Dy atom in the cation of **1-Dy** is determined by ray-tracing, and the unblocked rays are grouped into adjacent clusters (light blue, green, yellow, magenta). At the Dy atom, a total of 6.5% of the solid angle is exposed, with the largest cluster (light blue) comprising of 3.4% of the solid angle.

6. Powder X-ray diffraction

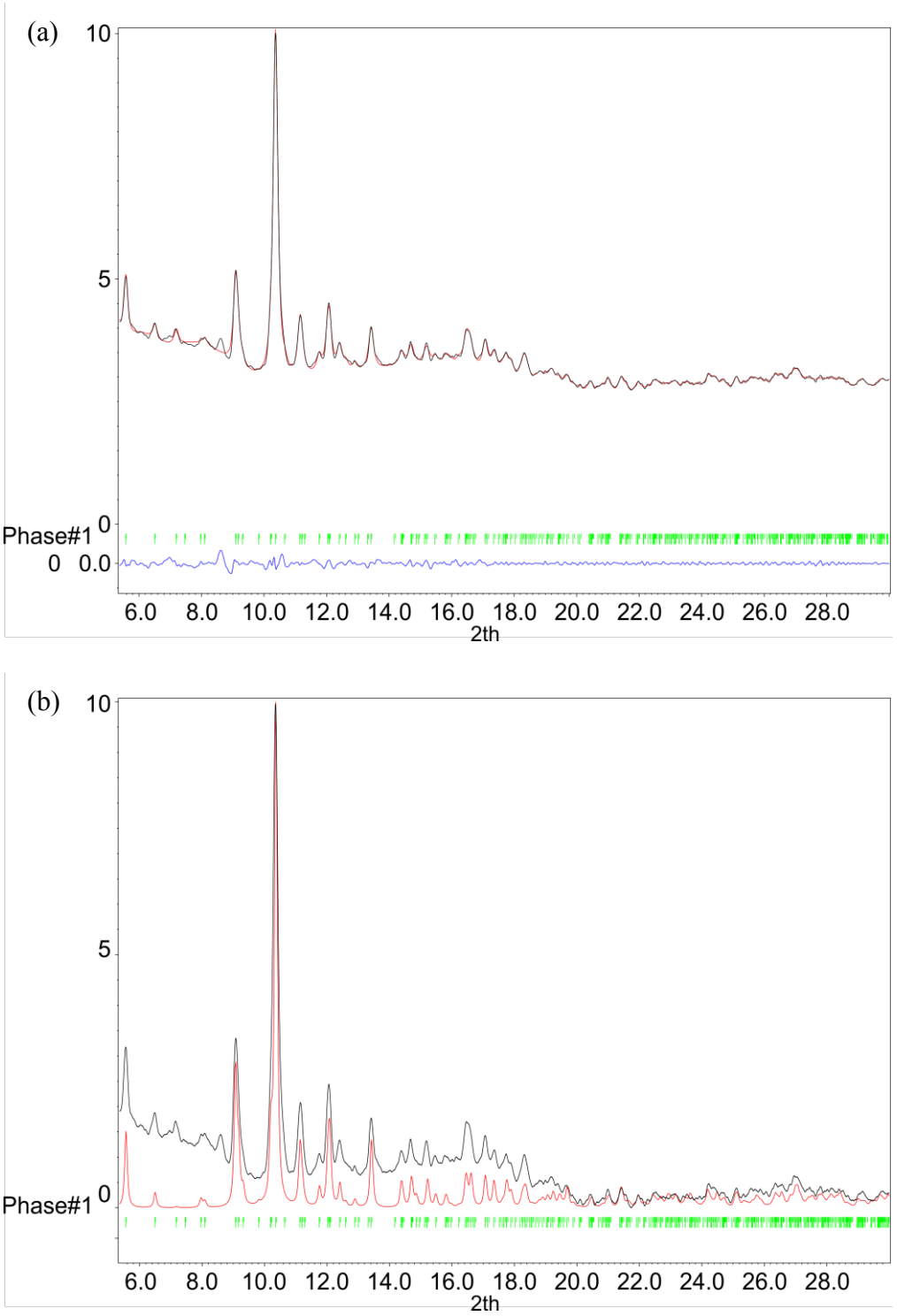

Figure S72. (a) Le Bail refinement analysis of **1-Dy** at 100 K. Experimental powder X-ray diffraction pattern (black), modelled data (red) and difference (blue). (b) Theoretical powder X-ray diffraction pattern simulated from single crystal X-ray diffraction at 100 K (red) compared to experimental pattern at 100 K (black).

Table S4. Unit cell values obtained from Le Bail refinement results for **1-Dy**.

Rwp	**Rwp′**	***a***	***b***	***c***	***α***	***β***	***γ***
2.222	11.385	19.53(3)	23.74(4)	31.80(5)	90	90	90

7. Magnetic measurements

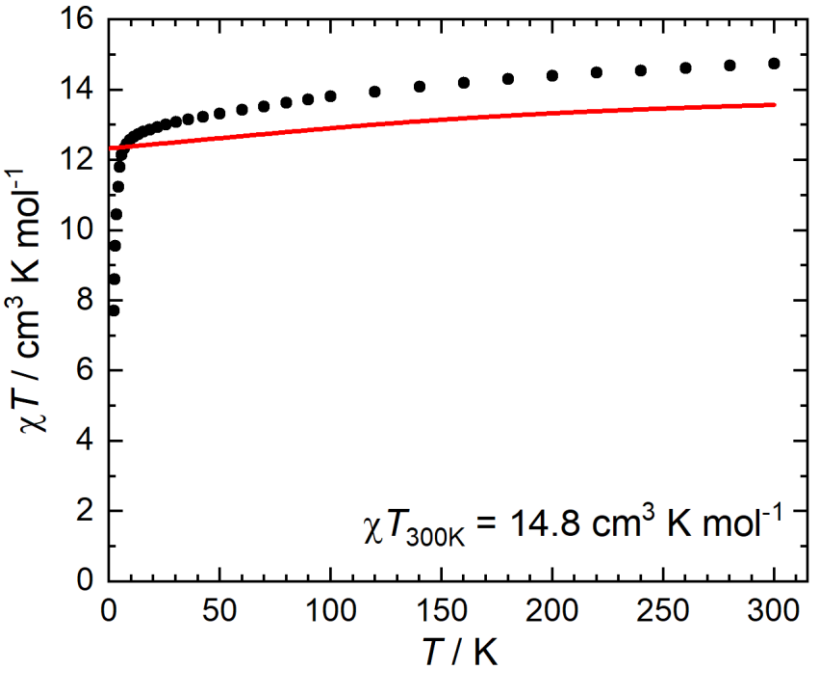

Figure S73. Temperature dependence of the molar magnetic susceptibility product (χT) for **1-Dy** suspended in eicosane (black circles) measured under a 0.1 T dc magnetic field and calculated CASSCF susceptibility (red line).

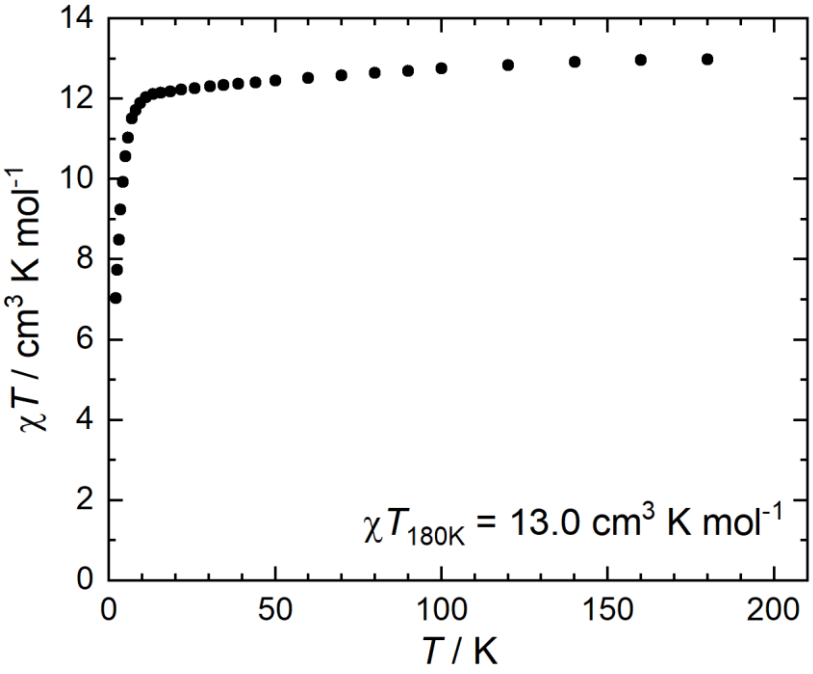

Figure S74. Temperature dependence of the molar magnetic susceptibility product (χT) for frozen solution of 200 mM **1-Dy** in fluorobenzene measured under a 0.1 T dc magnetic field.

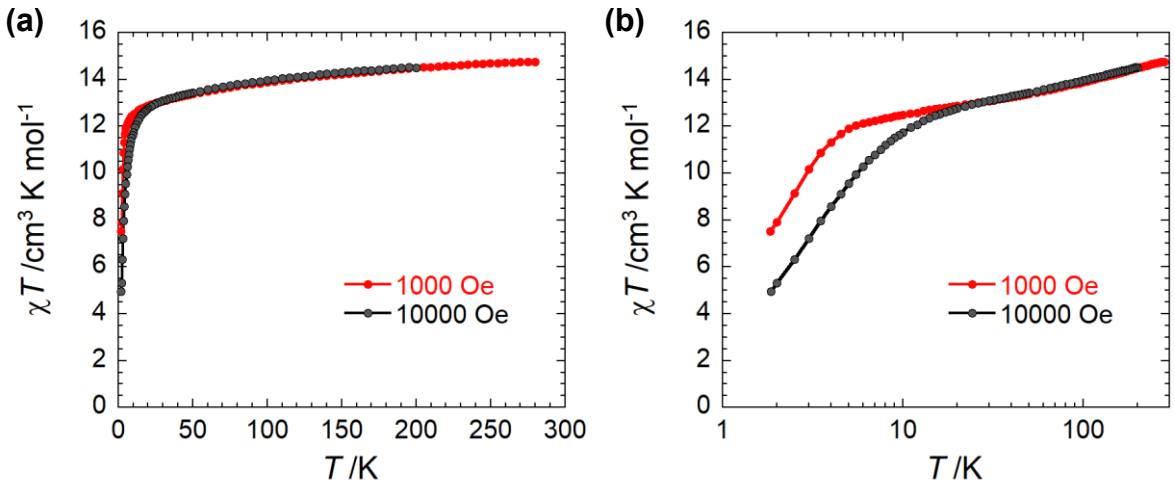

Figure S75. Temperature dependence of the molar magnetic susceptibility product (χT) for **1-Dy** suspended in mineral oil in a polypropylene bag measured under a 0.1 T (red) or 1 T (black) applied dc magnetic field, on (a) linear or (b) semi-logarithmic scale.

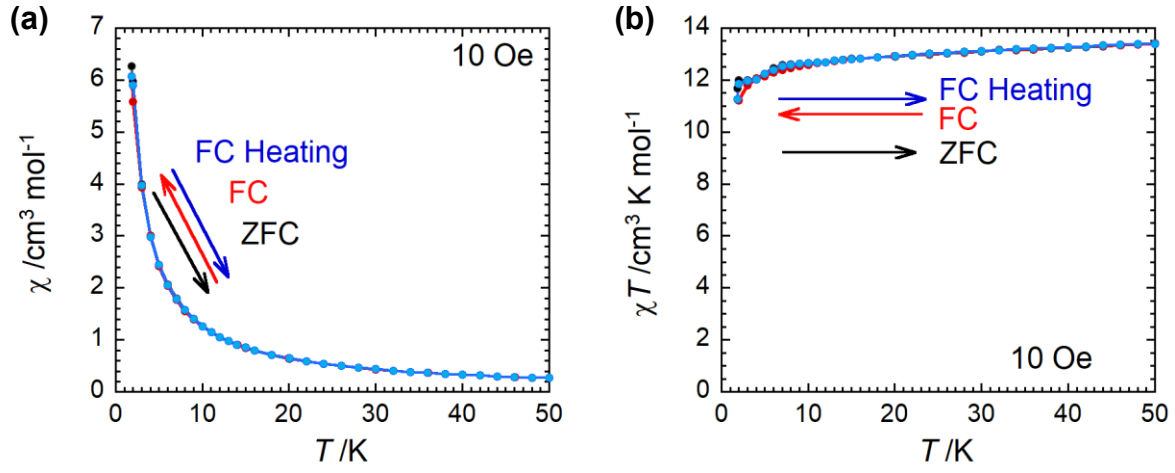

Figure S76. (a) Magnetic susceptibility (χ) and (b) molar magnetic susceptibility product (χT) *vs.* temperature (T) for **1-Dy** suspended in mineral oil in a polypropylene bag, under an applied dc field of 0.001 T, measured on warming after cooling in zero field (ZFC, black), on cooling in field (FC cool, red) and on warming in field (FC warm, blue).

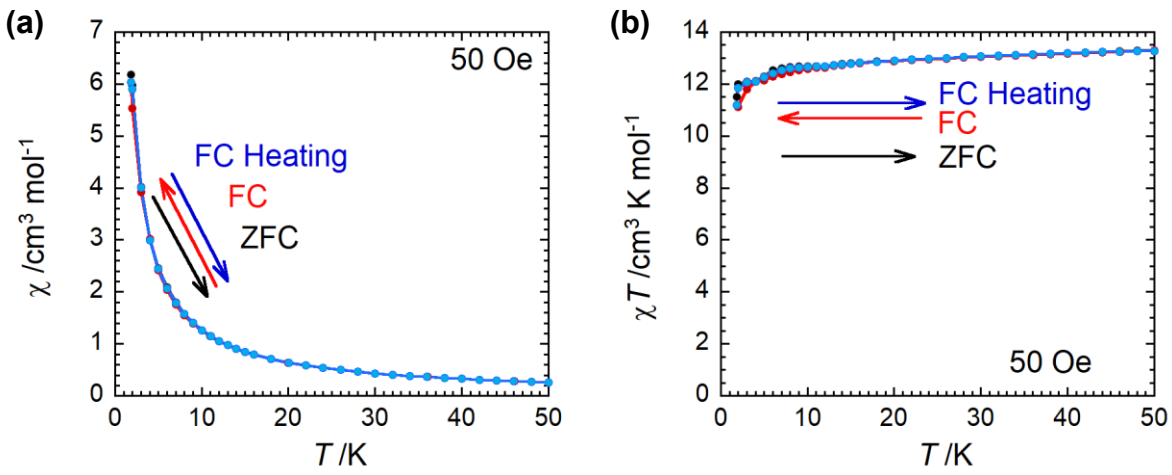

Figure S77. (a) Magnetic susceptibility (χ) and (b) molar magnetic susceptibility product (χT) *vs.* temperature (T) for **1-Dy** suspended in mineral oil in a polypropylene bag, under an applied dc field of 0.005 T, measured on warming after cooling in zero field (ZFC, black), on cooling in field (FC cool, red) and on warming in field (FC warm, blue).

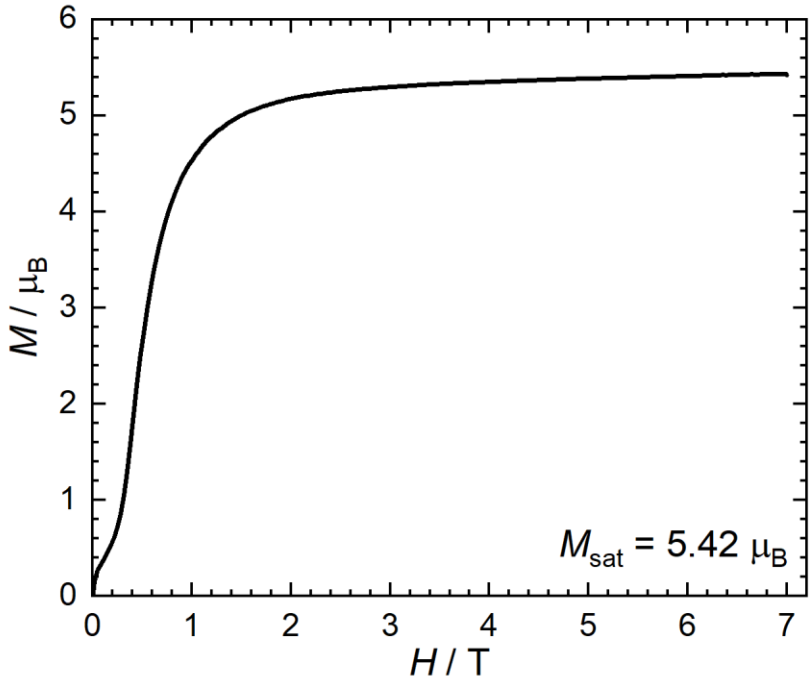

Figure S78. Field (H) dependence of the magnetization (M) (0–7 T) of **1-Dy** suspended in eicosane at 2 K after cooling in zero field. Sweep rate is 22 Oe s^{-1} (0.132 T min^{-1}).

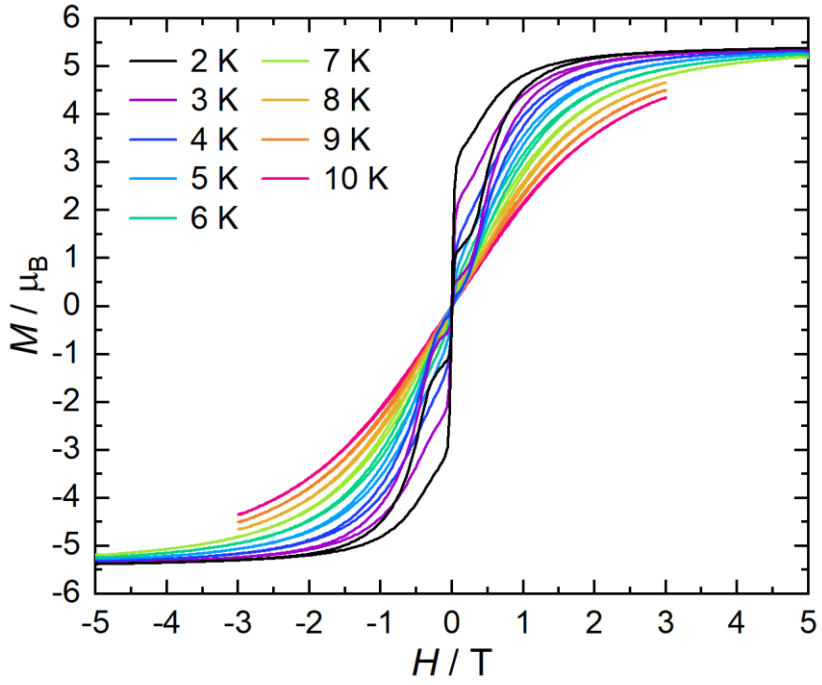

Figure S79. *M vs*. *H* hysteresis loops of **1-Dy** suspended in eicosane from 2 to 7 K in between –5 T to +5 T and from 8 to 10 K in between –3 T to +3 T. Sweep rate is 22 Oe s^{-1} (0.132 T min^{-1}).

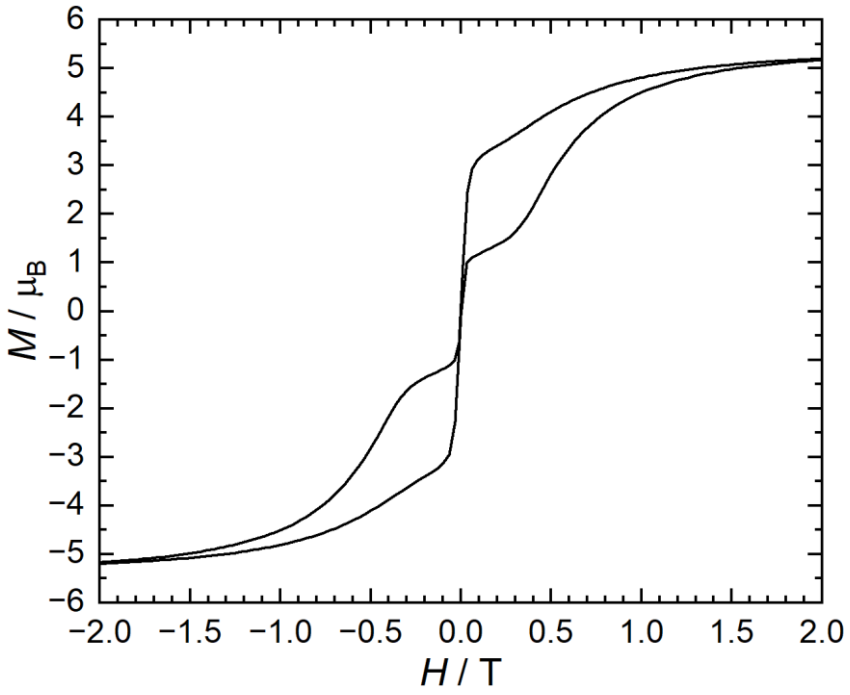

Figure S80. *M vs*. *H* hysteresis loop of **1-Dy** suspended in eicosane at 2 K, zoomed in between –2 T and 2 T. Sweep rate is 22 Oe s^{-1} (0.132 T min^{-1}).

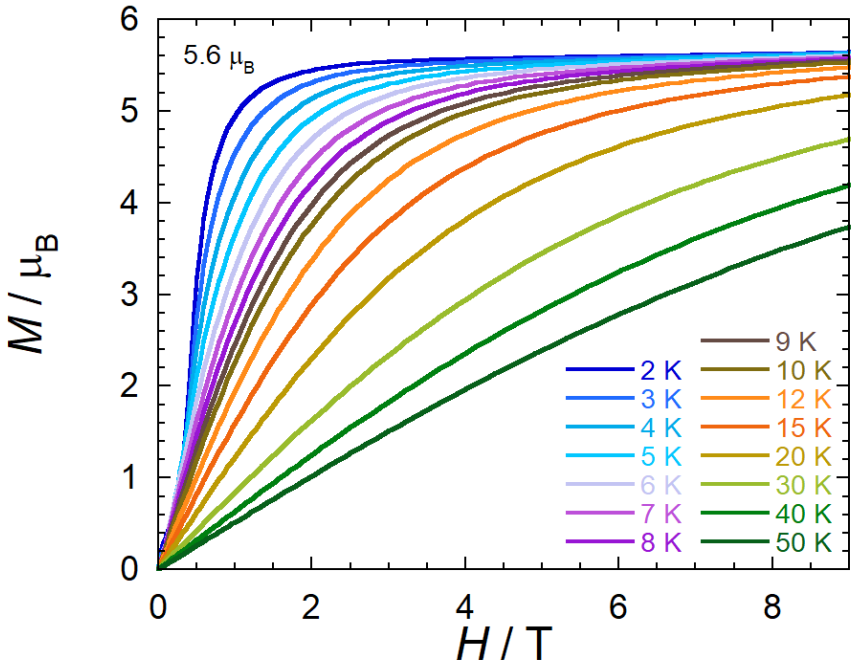

Figure S81. Field (*H*) dependence of the magnetization (*M*) (0–9 T) of **1-Dy** suspended in mineral oil in a polypropylene bag at 2–50 K after cooling in zero field. Sweep rate is 20 Oe s^{-1} (0.12 T min^{-1}).

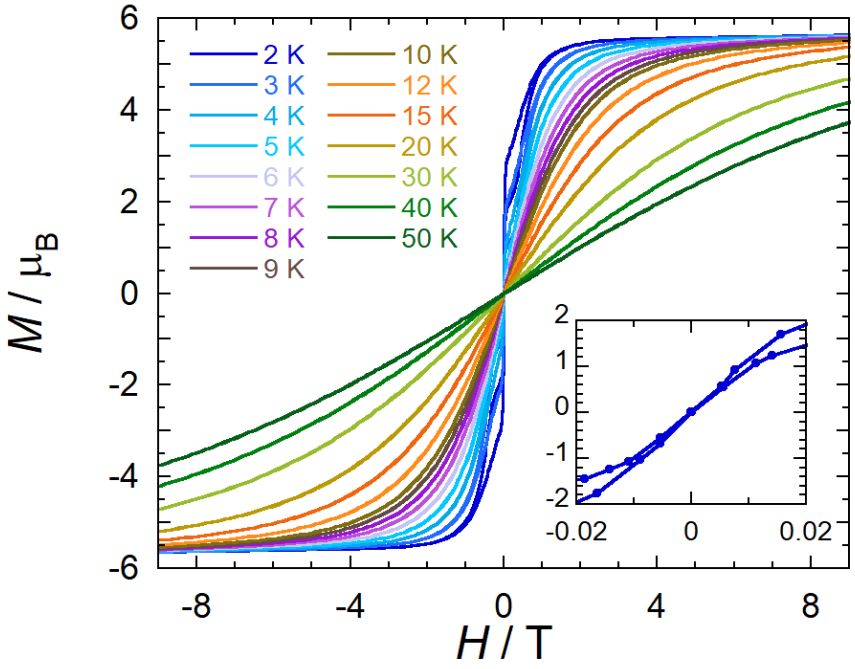

Figure S82. *M vs*. *H* hysteresis loops of **1-Dy** suspended in mineral oil in a polypropylene bag from 2 to 50 K in between –9 T to +9 T. Inset shows 2 K hysteresis closing at zero field. Sweep rate is 20 Oe s^{-1} (0.12 T min^{-1}).

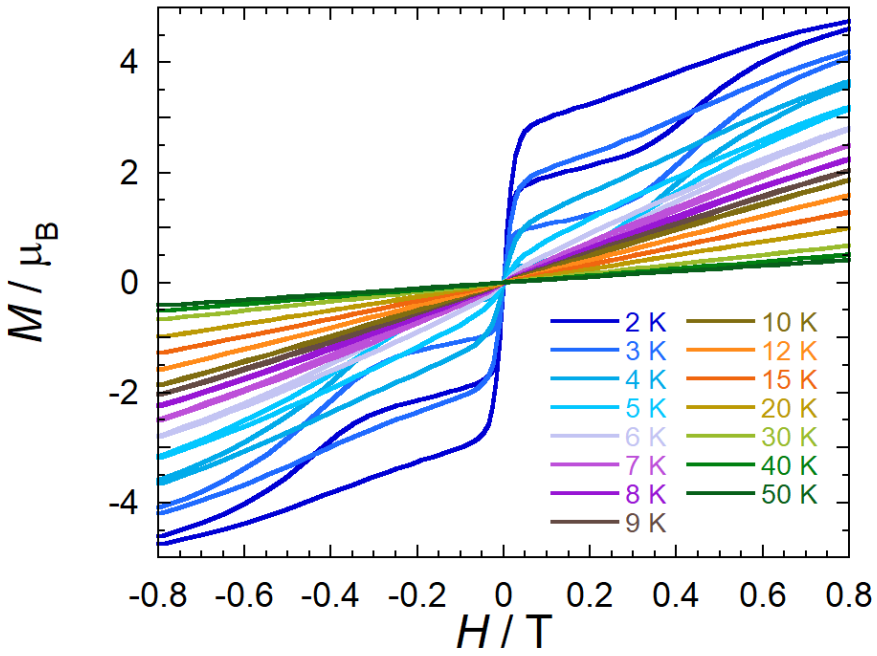

Figure S83. *M vs. H* hysteresis loops of **1-Dy** suspended in mineral oil in a polypropylene bag from 2 to 50 K, zoomed in to –0.8 T to +0.8 T. Sweep rate is 20 Oe s^{-1} (0.12 T min^{-1}).

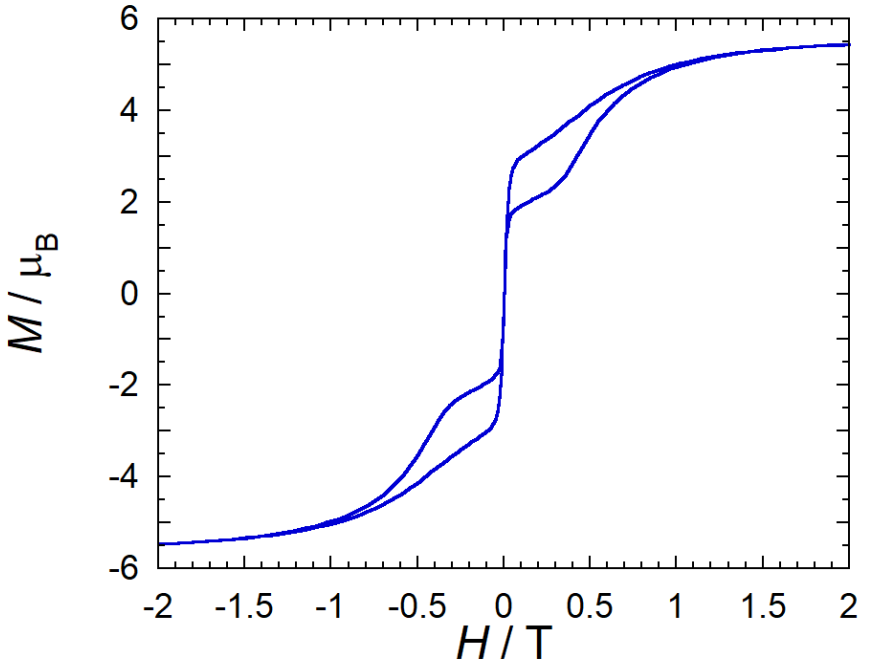

Figure S84. *M vs. H* hysteresis loops of **1-Dy** suspended in mineral oil in a polypropylene bag at 2 K, zoomed in to –2 T to +2 T. Sweep rate is 20 Oe s^{-1} (0.12 T min^{-1}).

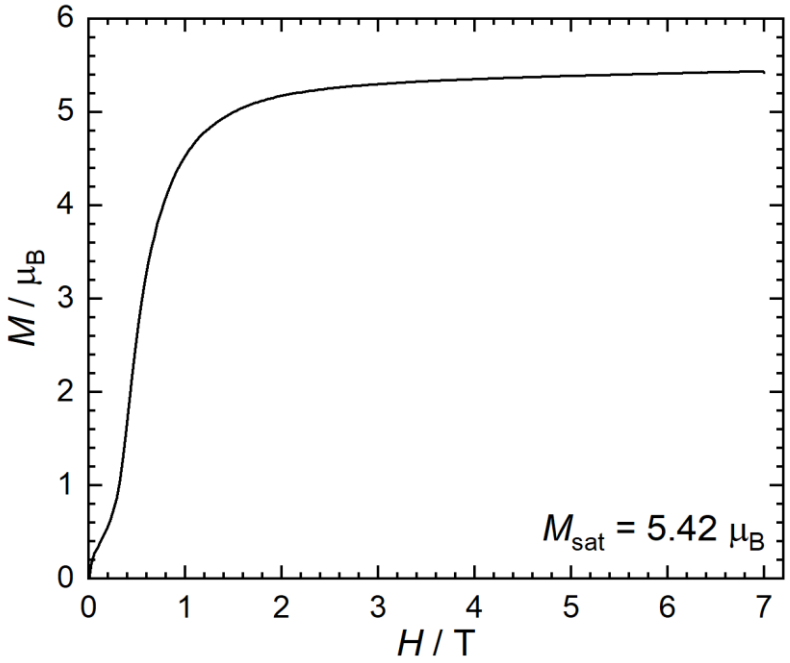

Figure S85. Field (*H*) dependence of the magnetization (0–7 T) of a 200 mM frozen solution of **1-Dy** in fluorobenzene at 2 K after cooling in zero field. Sweep rate is 22 Oe s^{-1} (0.132 T min^{-1}).

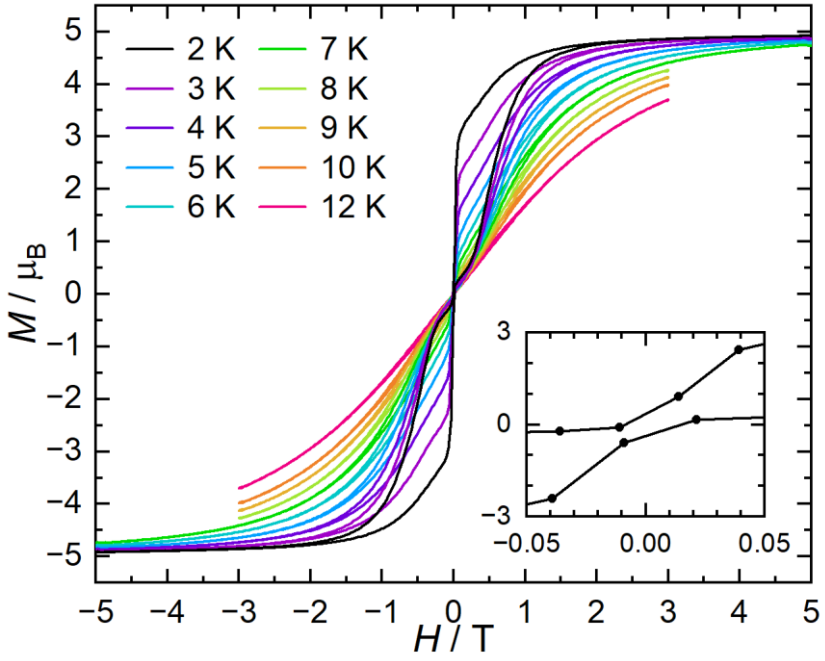

Figure S86. *M vs. H* hysteresis loops of a 200 mM frozen solution of **1-Dy** in fluorobenzene from 2 to 7 K in between –5 T to +5 T and from 8 to 12 K in between –3 T to +3 T. Inset shows 2 K hysteresis at low field. Sweep rate is 22 Oe s^{-1} (0.132 T min^{-1}).

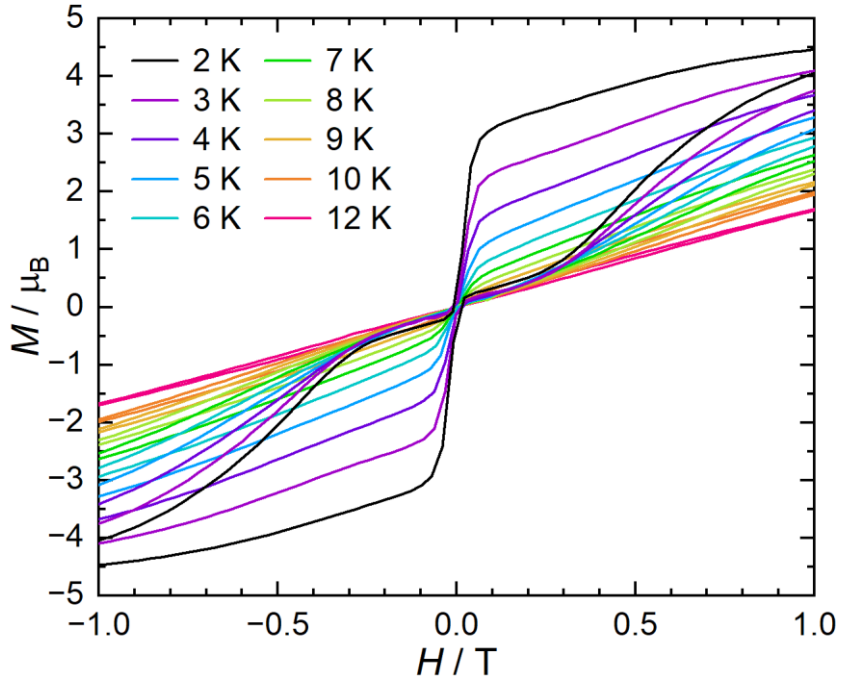

Figure S87. *M vs*. *H* hysteresis loops of a 200 mM frozen solution of **1-Dy** in fluorobenzene from 2–12 K, zoomed in to –1 T to +1 T. Sweep rate is 22 Oe s^{-1} (0.132 T min^{-1}).

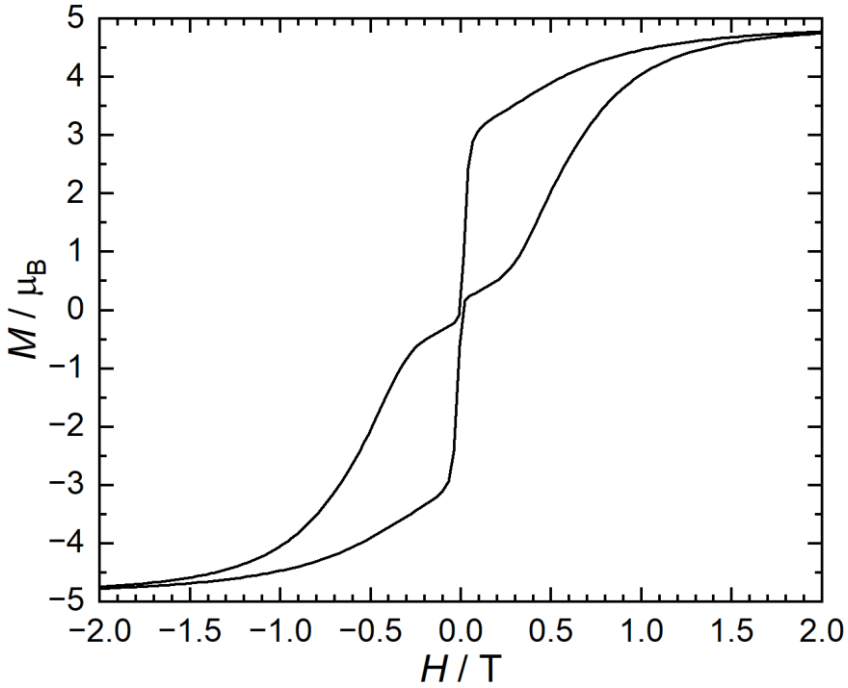

Figure S88. *M vs*. *H* hysteresis loop a 200 mM frozen solution of **1-Dy** in fluorobenzene at 2 K, zoomed in between –2 and +2 T. Sweep rate is 22 Oe s^{-1} (0.132 T min^{-1}).

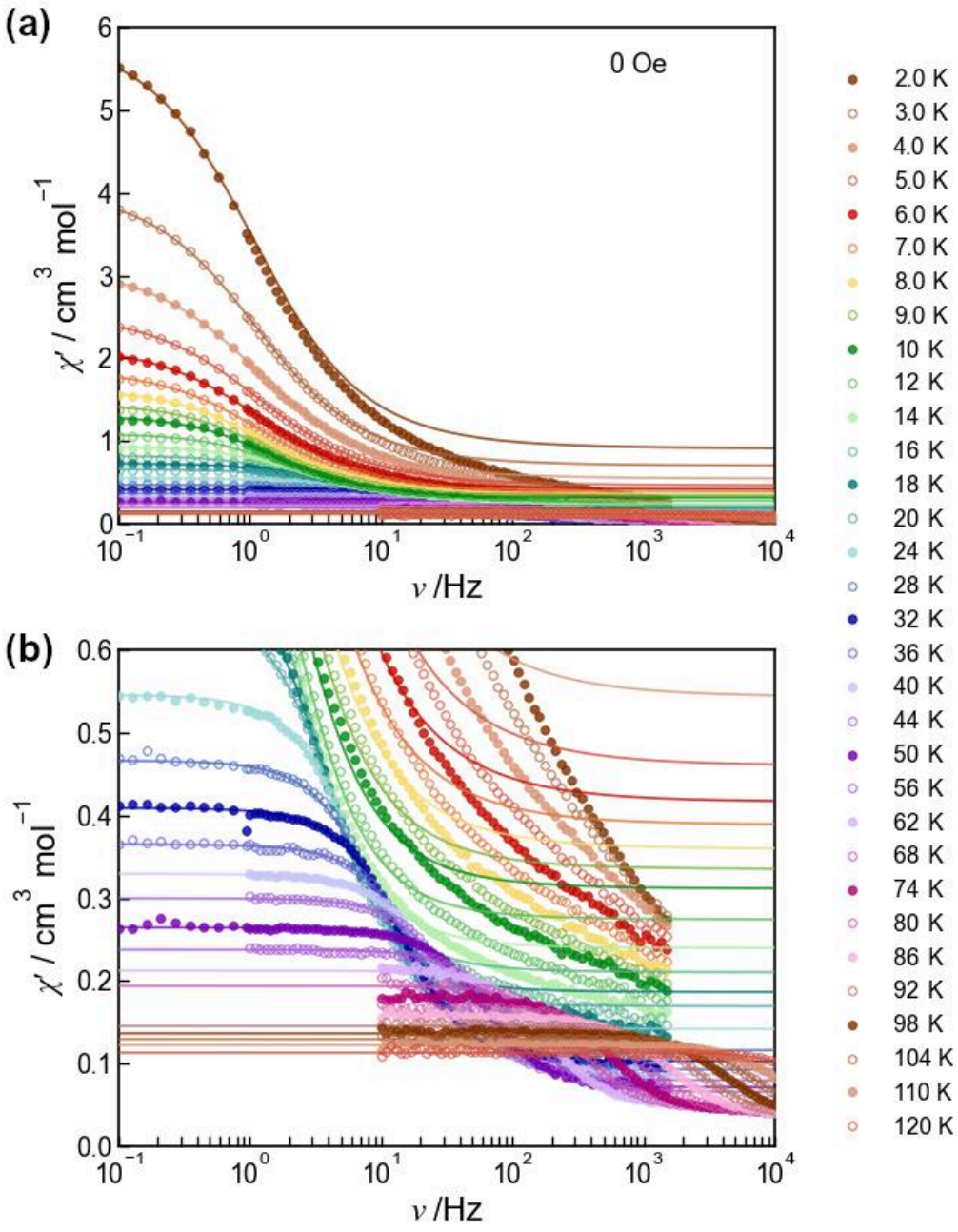

Figure S89. Fitting of the ac frequency dependence of the in-phase component of the ac susceptibility (χ′) for **1-Dy** suspended in mineral oil in a polypropylene bag in zero dc field to the generalized Debye model; (a) all data, (b) zoomed in to the high temperature region.

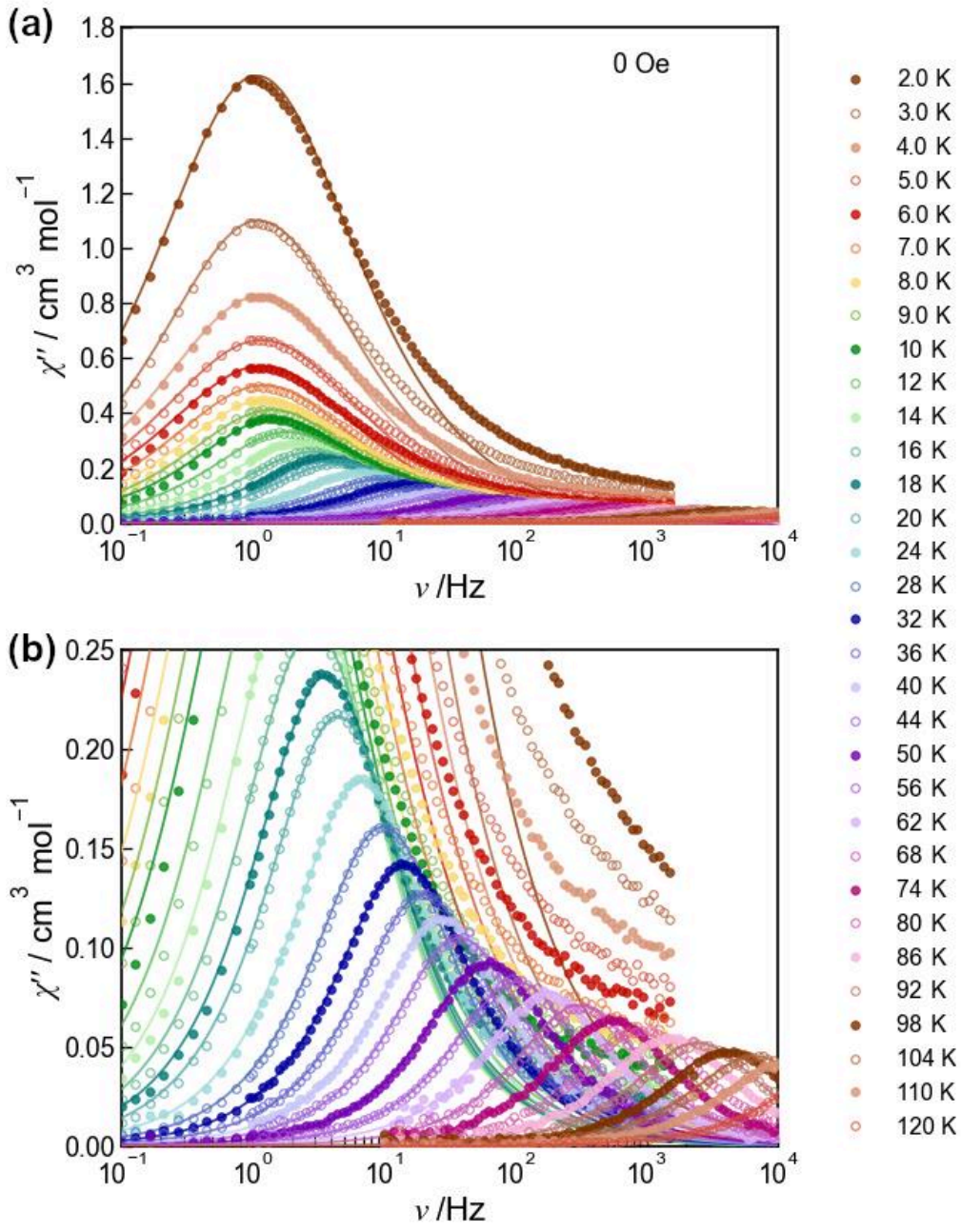

Figure S90. Fitting of the ac frequency dependence of the out-of-phase component of the ac susceptibility (χ′′) for **1-Dy** suspended in mineral oil in a polypropylene bag in zero dc field to the generalized Debye model; (a) all data, (b) zoomed in to the high temperature region.

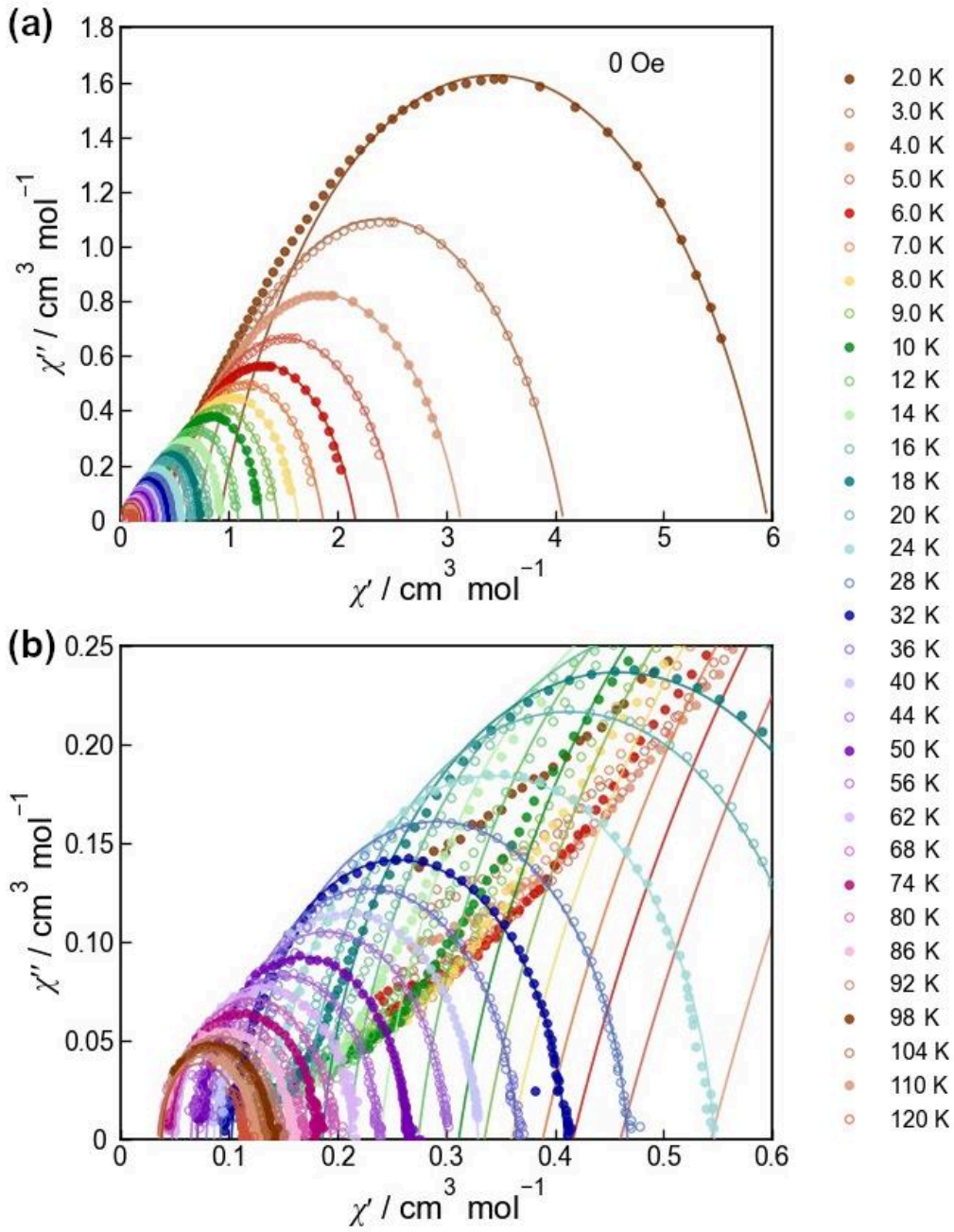

Figure S91. Cole-Cole plot showing fitting of ac data for **1-Dy** suspended in mineral oil in a polypropylene bag in zero dc field to the generalized Debye model; (a) all data, (b) zoomed-in to the high temperature region.

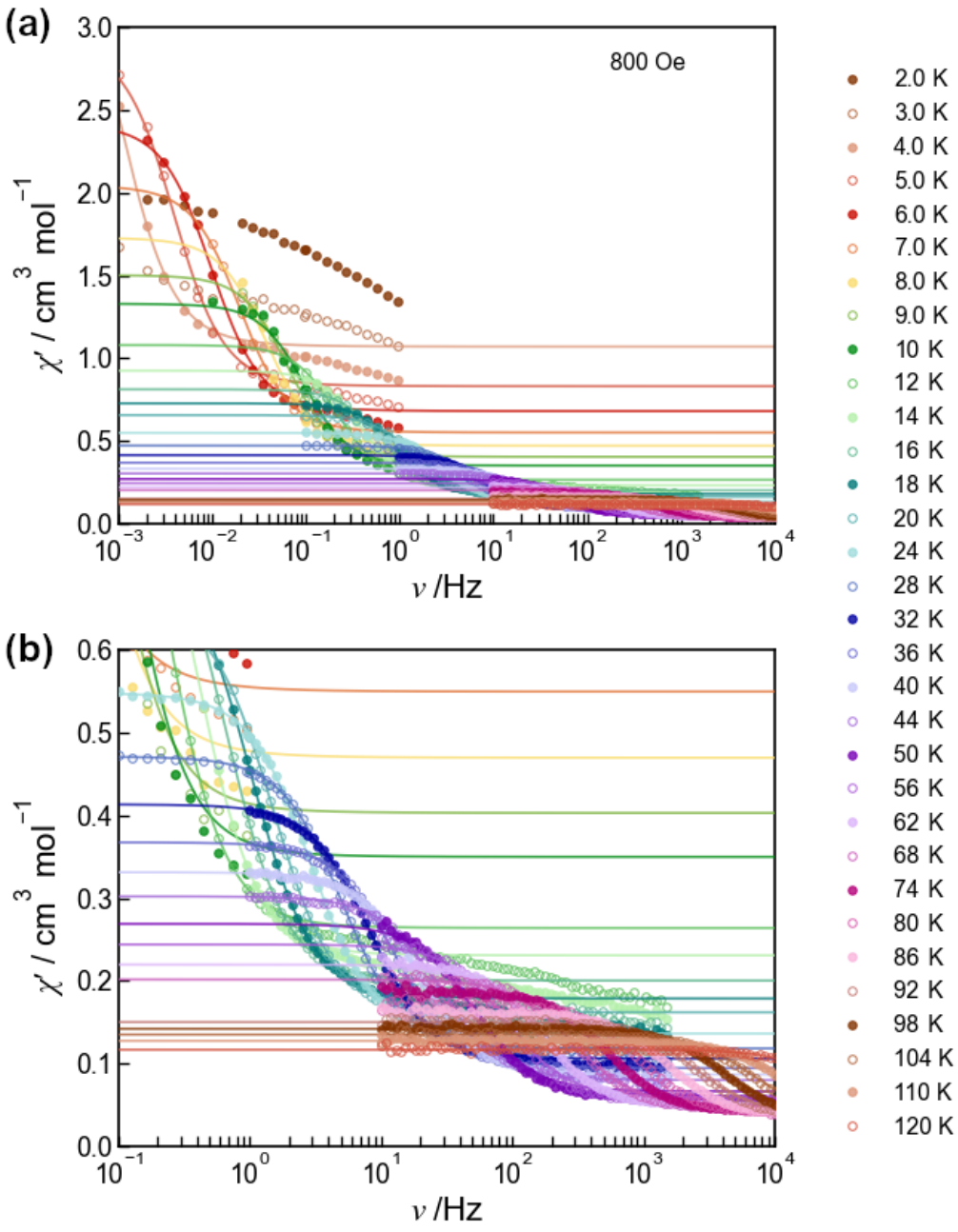

Figure S92. Fitting of the ac frequency dependence of the in-phase component of the ac susceptibility (χ′) for **1-Dy** suspended in mineral oil in a polypropylene bag in a 0.08 T dc field to the generalized Debye model; (a) all data, (b) zoomed in to the high temperature region.

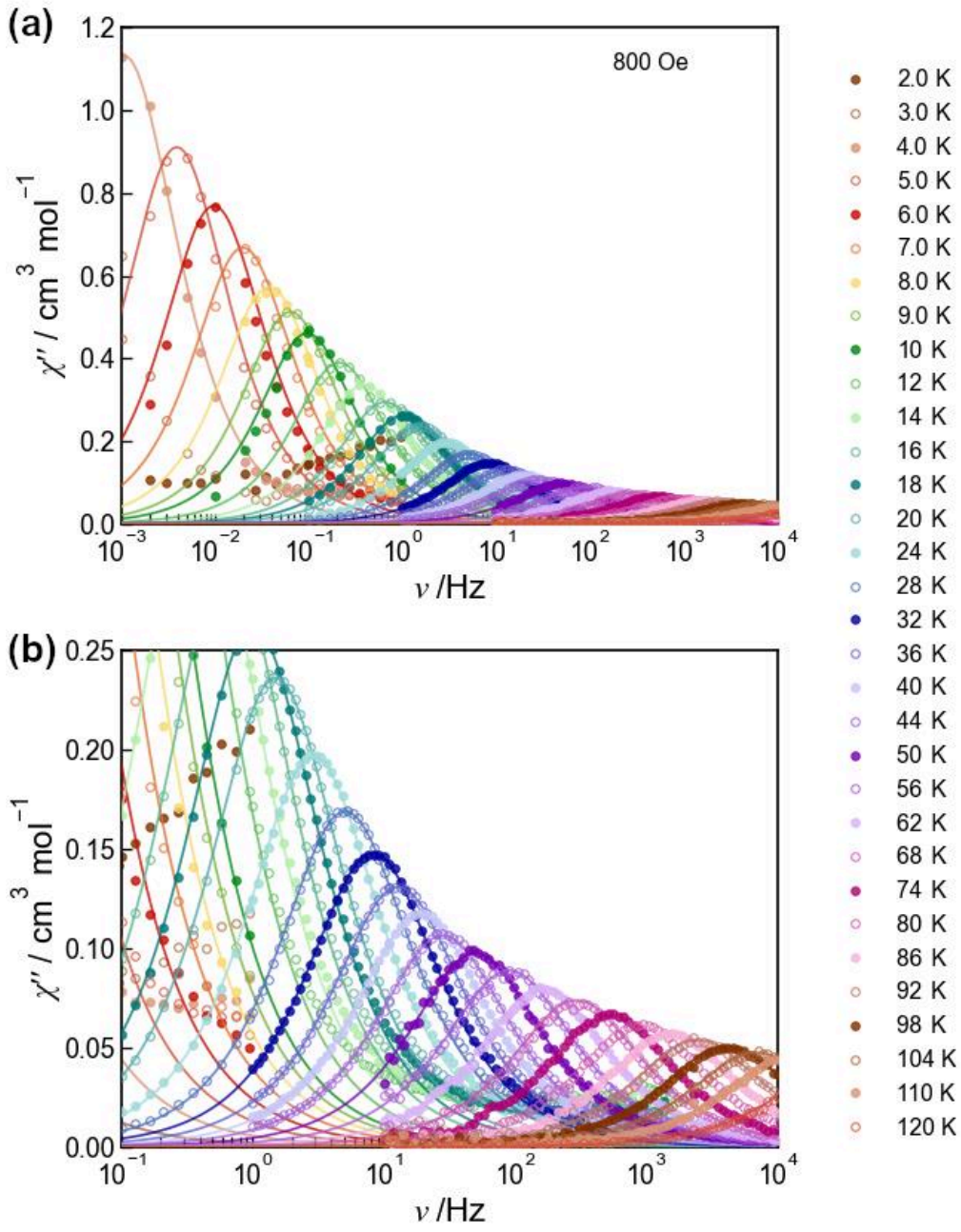

Figure S93. Fitting of the ac frequency dependence of the out-of-phase component of the ac susceptibility (χ′′) for **1-Dy** suspended in mineral oil in a polypropylene bag in a 0.08 T dc field to the generalized Debye model; (a) all data, (b) zoomed in to the high temperature region.

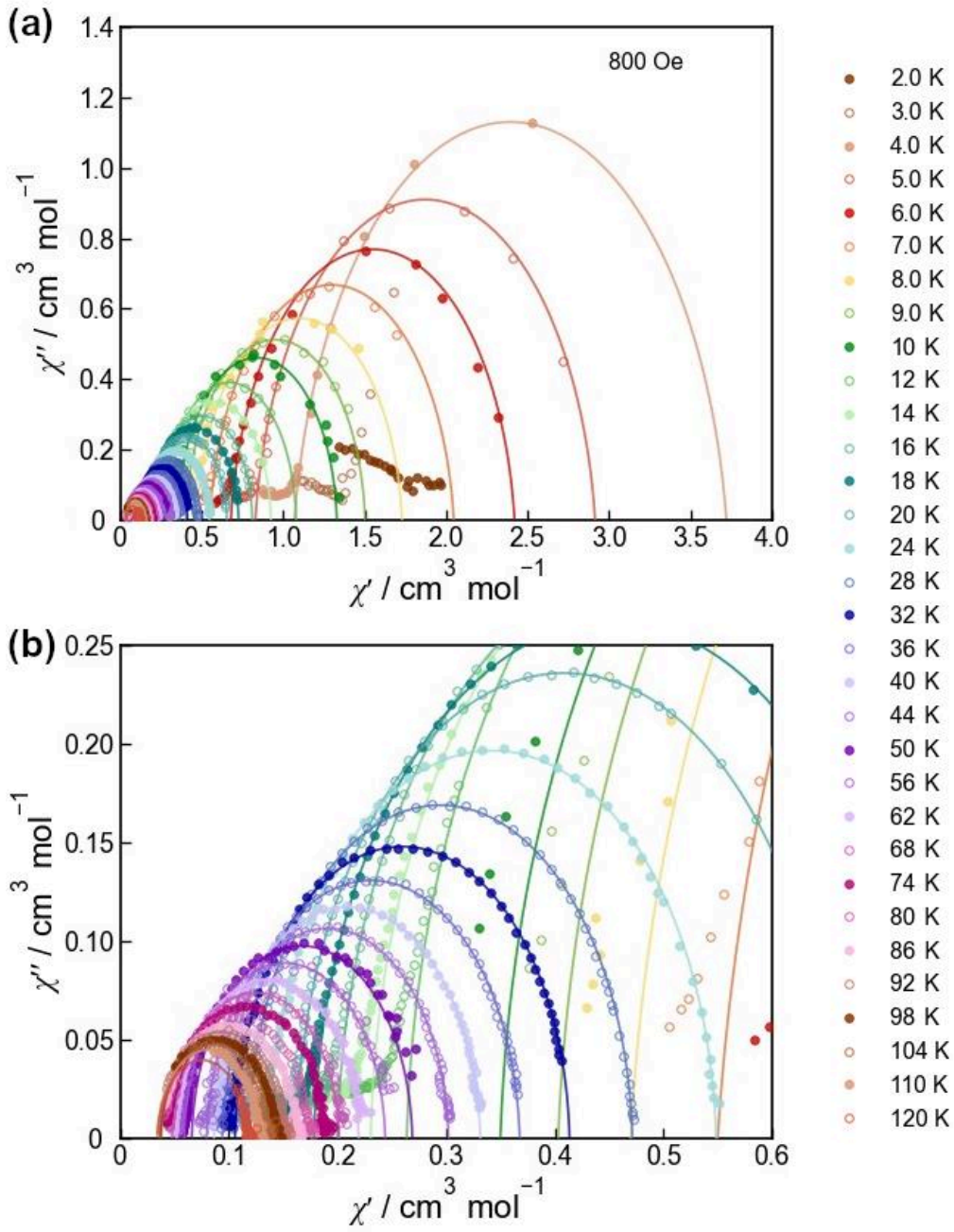

Figure S94. Cole-Cole plot showing fitting of ac data for **1-Dy** suspended in mineral oil in a polypropylene bag in a 0.08 T dc field to the generalized Debye model; (a) all data, (b) zoomed in to the high temperature region.

Table S5. Best fit parameters to the generalized Debye model for **1-Dy** suspended in mineral oil in a polypropylene bag in zero dc field. Note that the α parameter has been fixed at 0.014 for T ≥ 80 K according to its evolution observed at lower temperature.

T (K)	τ (s)	χ_S (cm^3 mol^{-1})	χ_T (cm^3 mol^{-1})	α
2	1.47251E-01	0.9100	5.9600	0.2717
3	1.43259E-01	0.7000	4.0800	0.2654
4	1.37433E-01	0.5440	3.1368	0.2772
5	1.35415E-01	0.4605	2.5618	0.2808
6	1.34738E-01	0.4168	2.1666	0.2633
7	1.30086E-01	0.3891	1.8696	0.2426
8	1.22685E-01	0.3601	1.6428	0.2204
9	1.13390E-01	0.3354	1.4570	0.1929
10	1.04292E-01	0.3118	1.3098	0.1673
12	8.55904E-02	0.2744	1.0885	0.1294
14	6.83684E-02	0.2397	0.9324	0.1060
16	5.43279E-02	0.2103	0.8194	0.1001
18	4.37083E-02	0.1864	0.7288	0.0861
20	3.53695E-02	0.1692	0.6561	0.0739
22	2.87692E-02	0.1541	0.5969	0.0672
24	2.34606E-02	0.1419	0.5467	0.0598
26	1.93606E-02	0.1234	0.5042	0.0617
28	1.60179E-02	0.1158	0.4668	0.0546
30	1.33408E-02	0.1089	0.4362	0.0514
32	1.10888E-02	0.1025	0.4094	0.0511
34	9.38239E-03	0.0969	0.3871	0.0523
36	7.88232E-03	0.0924	0.3653	0.0459
38	6.73419E-03	0.0889	0.3469	0.0443
40	5.75149E-03	0.0865	0.3295	0.0388
42	4.91046E-03	0.0835	0.3141	0.0349
44	4.21559E-03	0.0795	0.3000	0.0305
46	3.55806E-03	0.0775	0.2877	0.0348
48	3.04710E-03	0.0738	0.2751	0.0302
50	2.56982E-03	0.0711	0.2645	0.0310
52	2.18683E-03	0.0698	0.2554	0.0308
54	1.84390E-03	0.0683	0.2456	0.0220
56	1.54242E-03	0.0654	0.2376	0.0254
58	1.30371E-03	0.0645	0.2300	0.0244
60	1.08168E-03	0.0520	0.2187	0.0245
62	9.04788E-04	0.0520	0.2123	0.0192

64	7.52181E-04	0.0510	0.2062	0.0206
66	6.23123E-04	0.0490	0.1994	0.0197
68	5.17515E-04	0.0480	0.1939	0.0163
70	4.34010E-04	0.0465	0.1885	0.0139
72	3.57971E-04	0.0455	0.1824	0.0134
74	2.99011E-04	0.0448	0.1780	0.0134
76	2.55042E-04	0.0450	0.1730	0.0146
78	2.12582E-04	0.0440	0.1690	0.0145
80	1.78283E-04	0.0430	0.1652	0.0140
82	1.50813E-04	0.0420	0.1616	0.0140
84	1.27502E-04	0.0410	0.1586	0.0140
86	1.08386E-04	0.0410	0.1555	0.0140
88	9.07831E-05	0.0400	0.1510	0.0140
90	7.72304E-05	0.0390	0.1480	0.0140
92	6.55410E-05	0.0390	0.1453	0.0140
94	5.53469E-05	0.0380	0.1420	0.0140
96	4.62624E-05	0.0380	0.1393	0.0140
98	3.94997E-05	0.0380	0.1364	0.0140
100	3.31994E-05	0.0370	0.1335	0.0140
102	2.79481E-05	0.0370	0.1315	0.0140
104	2.39388E-05	0.0370	0.1295	0.0140
106	2.01048E-05	0.0370	0.1269	0.0140
108	1.68074E-05	0.0360	0.1251	0.0140
110	1.45339E-05	0.0360	0.1222	0.0140
112	1.19157E-05	0.0360	0.1210	0.0140
114	9.84826E-06	0.0350	0.1190	0.0140
116	8.34653E-06	0.0350	0.1170	0.0140
118	7.12598E-06	0.0350	0.1150	0.0140
120	5.81534E-06	0.0350	0.1130	0.0140

Table S6. Best fit parameters to the generalized Debye model for **1-Dy** suspended in mineral oil in a polypropylene bag in a 0.08 T dc field. Note that the α parameter has been fixed at 0.025 for T ≥ 50 K according to its evolution observed at lower temperature.

T (K)	τ (s)	χ_S (cm^3 mol^{-1})	χ_T (cm^3 mol^{-1})	α
4	1.45957E+02	1.0700	3.7200	0.1000
5	4.04141E+01	0.8300	2.9144	0.0854
6	1.62528E+01	0.6800	2.4200	0.0780
7	7.96232E+00	0.5500	2.0469	0.0722
8	4.19433E+00	0.4700	1.7300	0.0600
9	2.49586E+00	0.4032	1.5032	0.0451
10	1.64717E+00	0.3500	1.3300	0.0390
12	7.51276E-01	0.2639	1.0801	0.0287
14	4.06563E-01	0.2307	0.9253	0.0215
16	2.42777E-01	0.2003	0.8119	0.0234
18	1.56648E-01	0.1785	0.7276	0.0291
20	1.05718E-01	0.1619	0.6558	0.0284
22	7.48106E-02	0.1485	0.5978	0.0267
24	5.45765E-02	0.1361	0.5486	0.0296
26	4.08545E-02	0.1262	0.5072	0.0297
28	3.12743E-02	0.1181	0.4715	0.0279
30	2.42430E-02	0.1112	0.4402	0.0252
32	1.92033E-02	0.1057	0.4136	0.0247
34	1.53055E-02	0.0998	0.3893	0.0257
36	1.23688E-02	0.0942	0.3677	0.0280
38	1.01519E-02	0.0915	0.3492	0.0255
40	8.29934E-03	0.0864	0.3315	0.0273
42	6.85982E-03	0.0838	0.3175	0.0275
44	5.64387E-03	0.0797	0.3022	0.0277
46	4.66941E-03	0.0764	0.2896	0.0271
48	3.83669E-03	0.0734	0.2771	0.0246
50	3.17905E-03	0.0660	0.2690	0.0250
52	2.59928E-03	0.0640	0.2620	0.0250
54	2.13226E-03	0.0610	0.2510	0.0250
56	1.76461E-03	0.0590	0.2440	0.0250
58	1.43620E-03	0.0570	0.2370	0.0250
60	1.20377E-03	0.0530	0.2272	0.0250
62	9.73515E-04	0.0520	0.2197	0.0250
64	8.01638E-04	0.0510	0.2132	0.0250
66	6.55860E-04	0.0480	0.2058	0.0250

68	5.43950E-04	0.0480	0.2017	0.0250
70	4.48051E-04	0.0460	0.1953	0.0250
72	3.69712E-04	0.0455	0.1901	0.0250
74	3.08685E-04	0.0455	0.1855	0.0250
76	2.56518E-04	0.0450	0.1810	0.0250
78	2.13719E-04	0.0430	0.1762	0.0250
80	1.78518E-04	0.0420	0.1710	0.0250
82	1.50733E-04	0.0420	0.1680	0.0250
84	1.26104E-04	0.0410	0.1640	0.0250
86	1.06245E-04	0.0400	0.1600	0.0250
88	8.89631E-05	0.0400	0.1570	0.0250
90	7.69043E-05	0.0390	0.1530	0.0250
92	6.48354E-05	0.0380	0.1500	0.0250
94	5.48439E-05	0.0380	0.1470	0.0250
96	4.64501E-05	0.0380	0.1440	0.0250
98	3.90646E-05	0.0370	0.1420	0.0250
100	3.29244E-05	0.0370	0.1392	0.0250
102	2.71707E-05	0.0360	0.1365	0.0250
104	2.33151E-05	0.0360	0.1350	0.0250
106	1.93660E-05	0.0355	0.1320	0.0250
108	1.62626E-05	0.0345	0.1290	0.0250
110	1.36940E-05	0.0343	0.1274	0.0250
112	1.14634E-05	0.0342	0.1248	0.0250
114	9.57551E-06	0.0343	0.1223	0.0250
116	8.05873E-06	0.0343	0.1205	0.0250
118	6.90180E-06	0.0343	0.1185	0.0250
120	5.62728E-06	0.0343	0.1167	0.0250

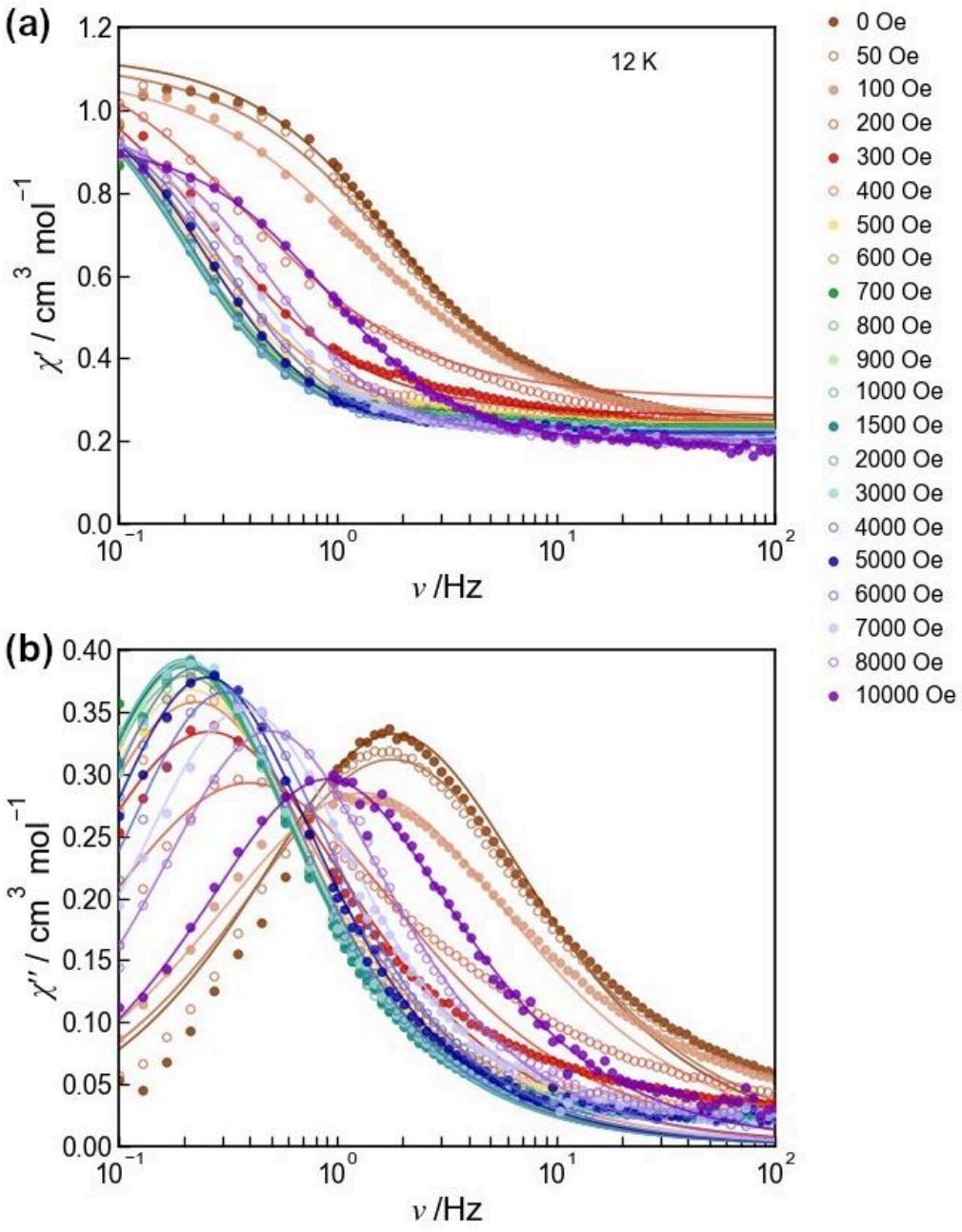

Figure S95. Fitting the ac frequency dependence of the (a) in-phase (χ′) and (b) out-of-phase (χ′′) components of the ac susceptibility for **1-Dy** suspended in mineral oil in a polypropylene bag at 12 K and variable dc field to the generalized Debye model.

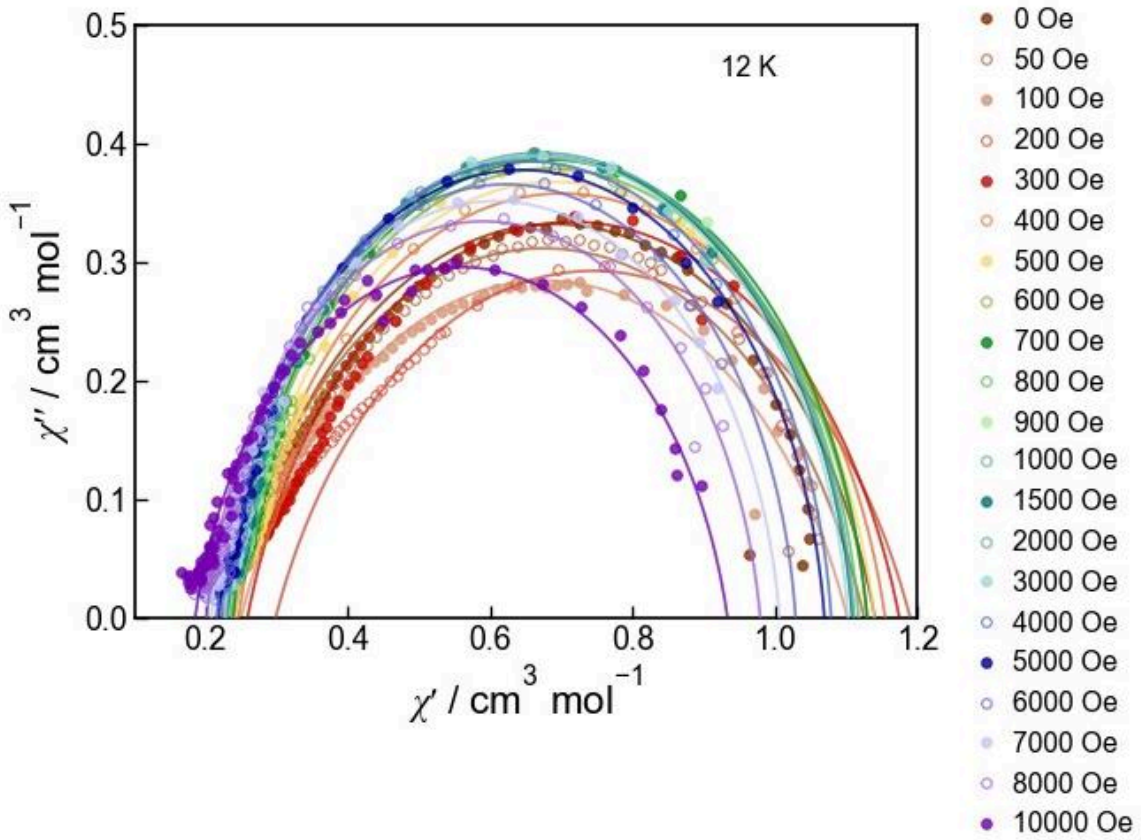

Figure S96. Cole-Cole plot showing fitting of ac data for **1-Dy** suspended in mineral oil in a polypropylene bag at 12 K and variable dc field to the generalized Debye model.

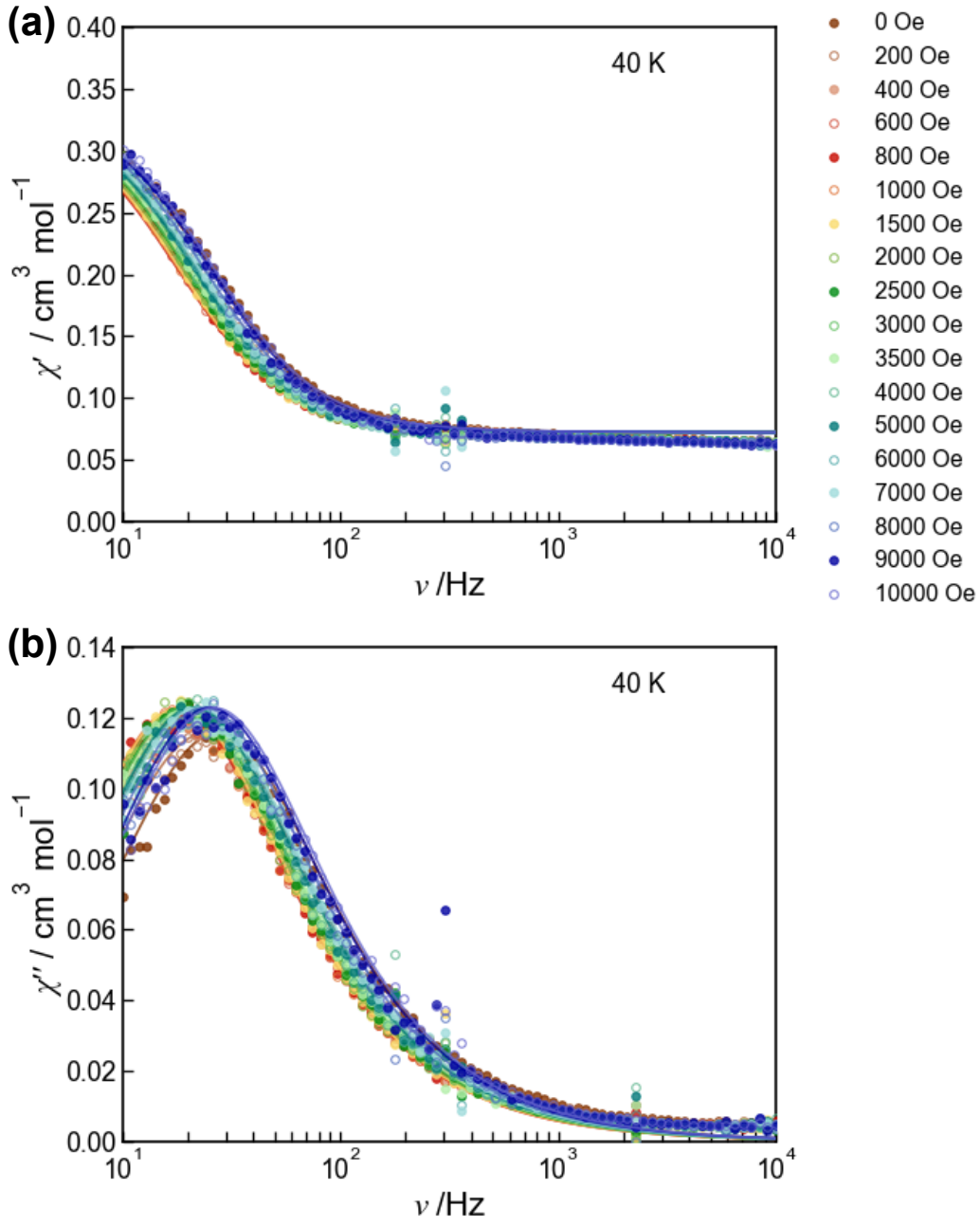

Figure S97. Fitting the ac frequency dependence of the (a) in-phase (χ′) and (b) out-of-phase (χ″) components of the ac susceptibility for **1-Dy** suspended in mineral oil in a polypropylene bag at 40 K and variable dc field to the generalized Debye model.

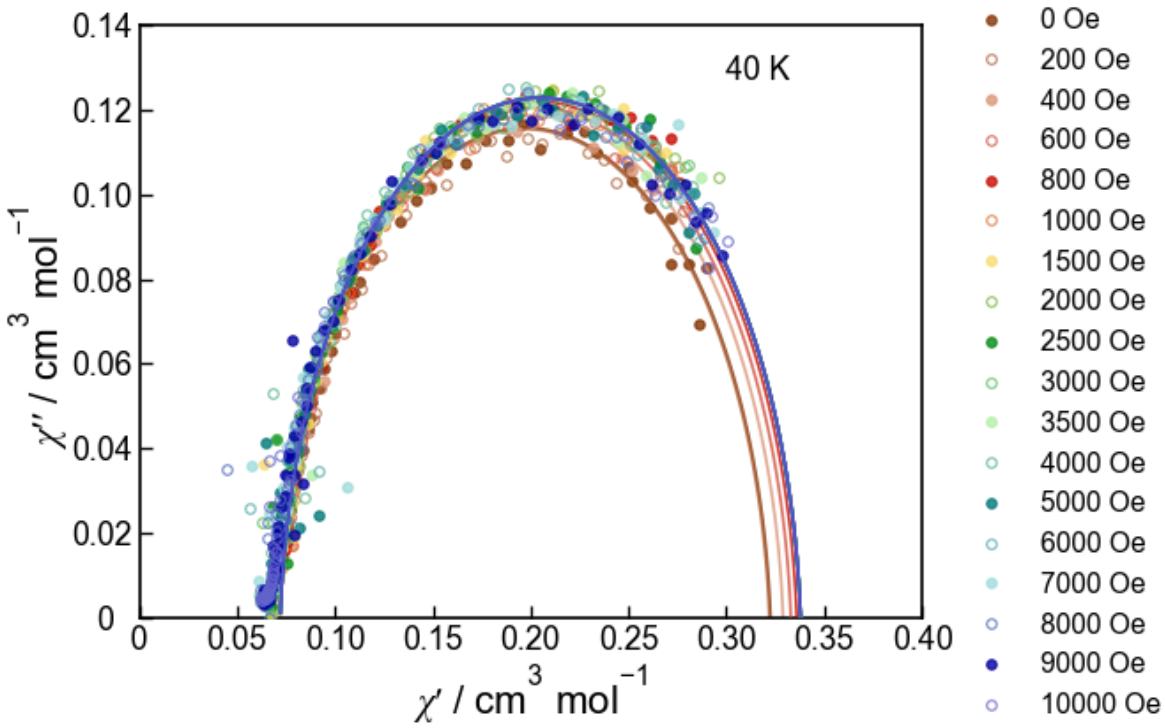

Figure S98. Cole-Cole plot showing fitting of ac data for **1-Dy** suspended in mineral oil in a polypropylene bag at 40 K and variable dc field to the generalized Debye model.

Table S7. Best fit parameters to the generalized Debye model for **1-Dy** suspended in mineral oil in a polypropylene bag in at 12 K and variable dc field.

H (Oe)	τ (s)	χ_S (cm^3 mol^{-1})	χ_T (cm^3 mol^{-1})	α
0	8.76416E-02	0.24000	1.14100	0.19054
50	8.95203E-02	0.22571	1.12571	0.22815
100	1.20253E-01	0.25000	1.10218	0.25000
200	3.99786E-01	0.29856	1.19057	0.26000
300	6.09480E-01	0.25899	1.17527	0.19746
400	7.01920E-01	0.24639	1.15543	0.15000
500	7.42237E-01	0.24205	1.14030	0.12577
600	7.72583E-01	0.23816	1.13025	0.10270
700	7.90682E-01	0.23855	1.13002	0.09000
800	7.95703E-01	0.23602	1.11806	0.08159
900	7.87238E-01	0.23509	1.12188	0.07900
1500	7.81688E-01	0.23127	1.10906	0.07506
2000	7.91849E-01	0.22994	1.11207	0.07373
3000	7.52655E-01	0.22690	1.10312	0.07378
4000	7.01277E-01	0.22324	1.07953	0.06670
5000	6.23681E-01	0.21885	1.06997	0.07496
6000	5.15704E-01	0.21561	1.02939	0.06724
7000	4.21697E-01	0.20850	1.00678	0.08017
8000	3.20551E-01	0.20185	0.97986	0.09527
10000	1.75568E-01	0.18550	0.93379	0.14775

Table S8. Best fit parameters to the generalized Debye model for **1-Dy** suspended in mineral oil in a polypropylene bag in at 40 K and variable dc field. Note that the α parameter has been fixed at 0.05, χ_S has been fixed at 0.072 and for non-zero fields χ_T has been fixed at the value indicated.

H (Oe)	τ (s)	χ_S (cm^3 mol^{-1})	χ_T (cm^3 mol^{-1})	α
0	5.78755E-03	7.2E-02	3.2264E-01	0.05
200	6.70644E-03	7.2E-02	3.22E-01	0.05
400	7.94366E-03	7.2E-02	3.29E-01	0.05
600	8.42191E-03	7.2E-02	3.33E-01	0.05
800	8.83600E-03	7.2E-02	3.36E-01	0.05
1000	8.82572E-03	7.2E-02	3.38E-01	0.05
1500	8.68817E-03	7.2E-02	3.38E-01	0.05
2000	8.41760E-03	7.2E-02	3.38E-01	0.05
2500	8.13101E-03	7.2E-02	3.38E-01	0.05
3000	8.05019E-03	7.2E-02	3.38E-01	0.05
3500	7.82158E-03	7.2E-02	3.38E-01	0.05
4000	7.55457E-03	7.2E-02	3.38E-01	0.05
5000	7.45719E-03	7.2E-02	3.38E-01	0.05
6000	7.23738E-03	7.2E-02	3.38E-01	0.05
7000	7.08064E-03	7.2E-02	3.38E-01	0.05
8000	6.71477E-03	7.2E-02	3.38E-01	0.05
9000	6.30572E-03	7.2E-02	3.38E-01	0.05
10000	6.04170E-03	7.2E-02	3.38E-01	0.05

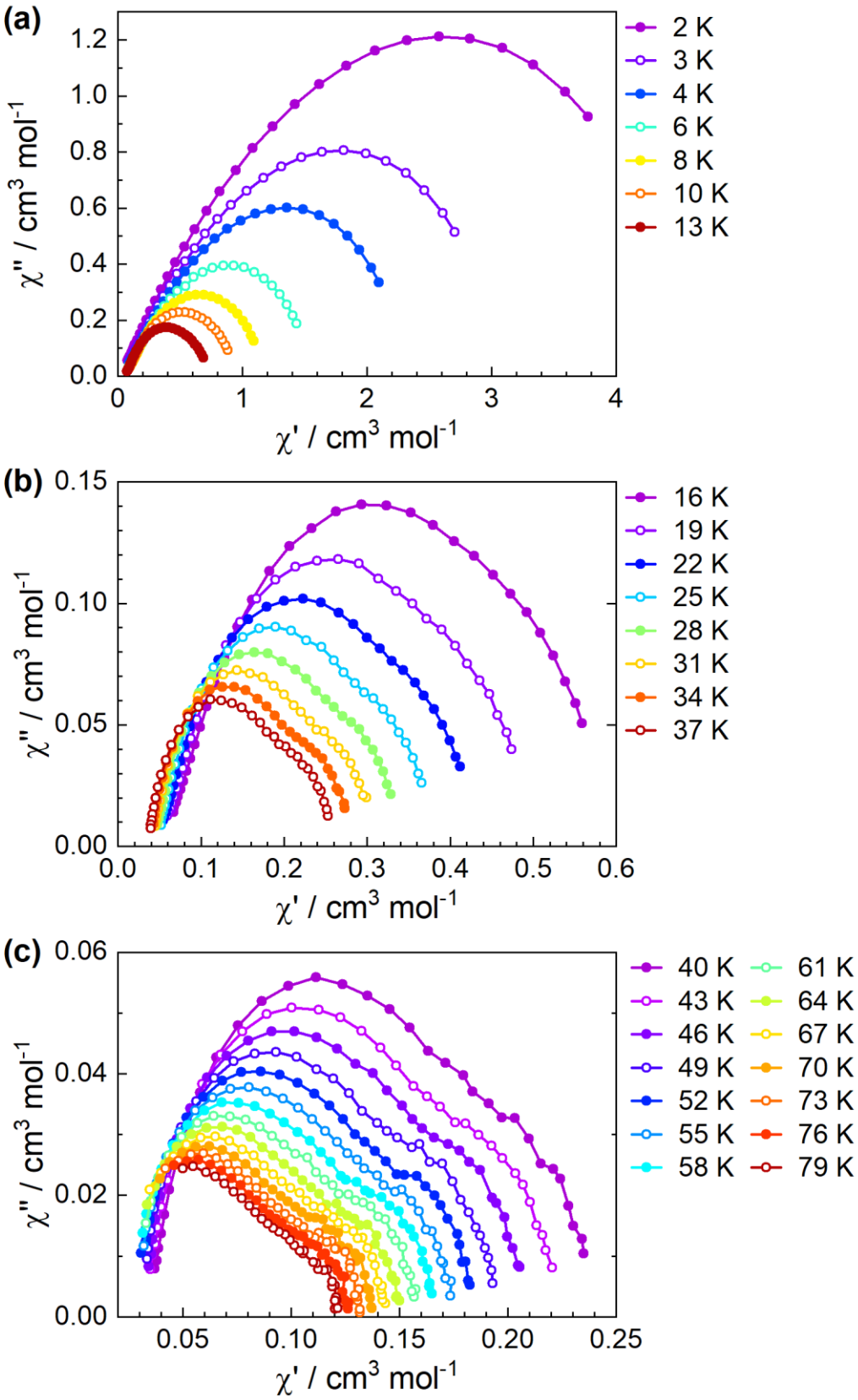

Figure S99. Cole-Cole plot showing ac data (a) 2–13 K, (b) 16–37 K, (c) 40–79 K for 200 mM frozen solution of **1-Dy** in fluorobenzene in zero dc field; lines are guides for the eyes.

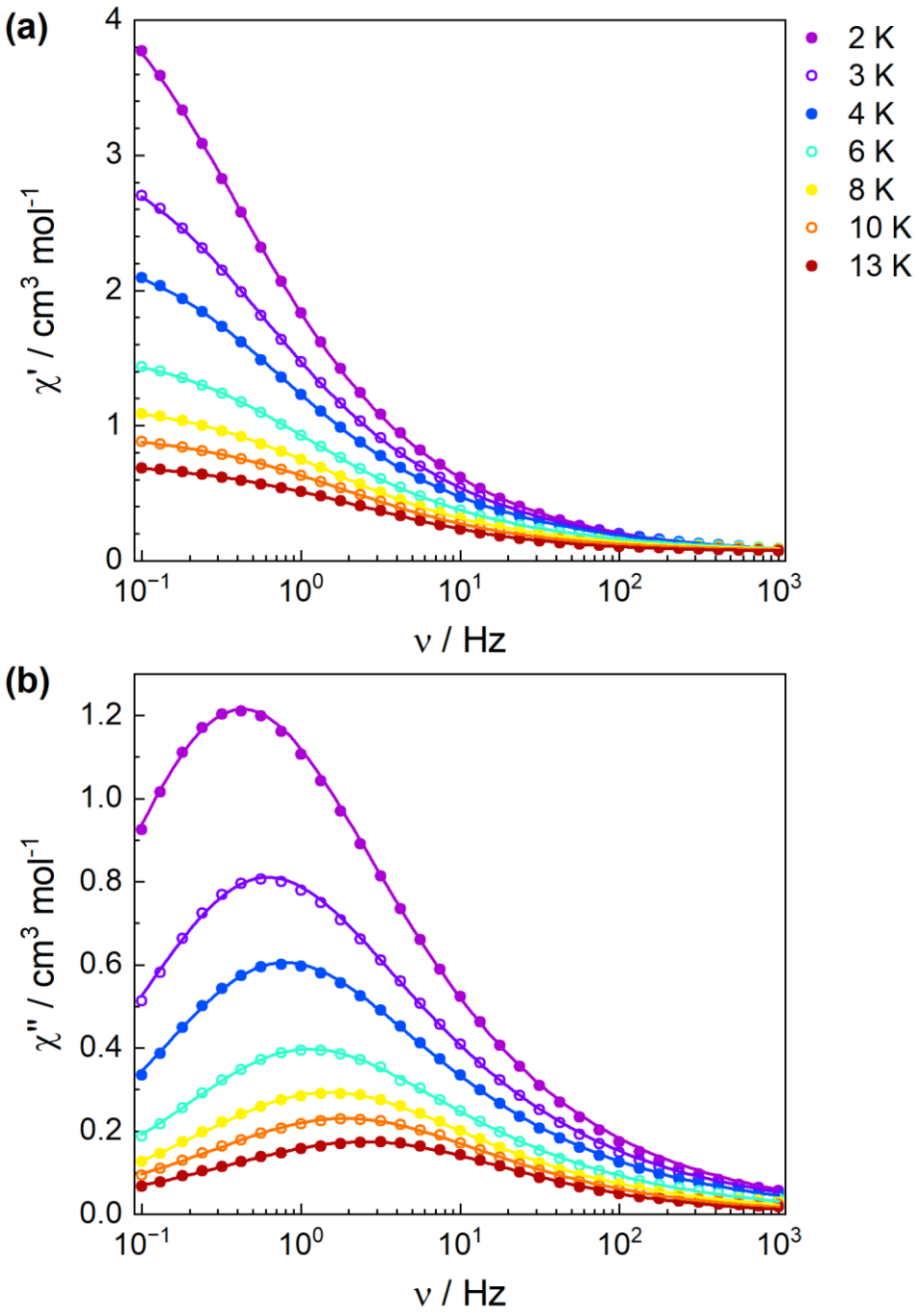

Figure S100. Fitting of the ac frequency dependence of the (a) in-phase (χ′) and (b) out-of-phase (χ″) components of the ac susceptibility for a 200 mM frozen solution of **1-Dy** in fluorobenzene (2–16 K) in zero dc field to Havriliak-Negami model.

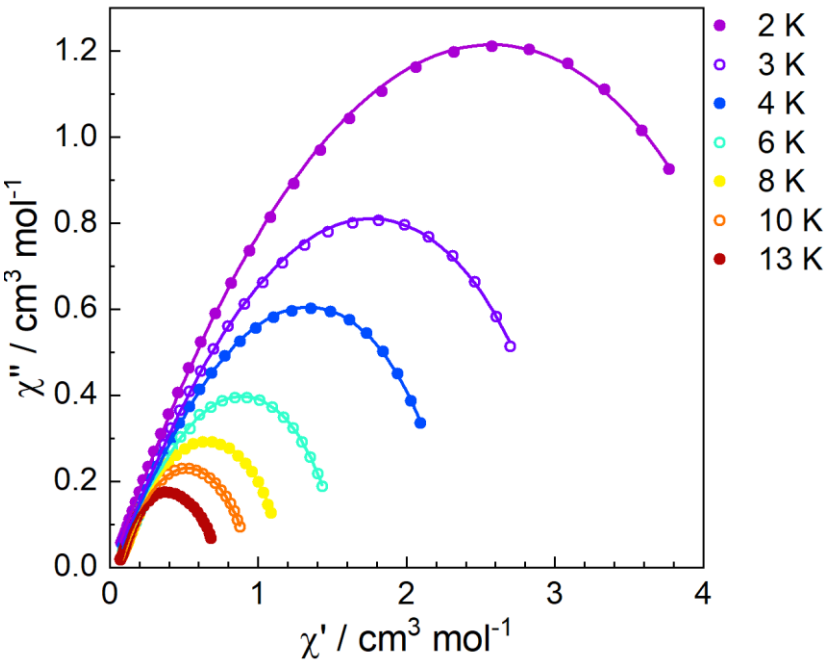

Figure S101. Cole-Cole plot showing fitting of ac data for 200 mM frozen solution of **1-Dy** in fluorobenzene (2–13 K) in zero dc field to Havriliak-Negami model.

Table S9. Best fit parameters to the Havriliak-Negami model for 200 mM frozen solution of **1-Dy** in fluorobenzene in zero dc field.

T (K)	τ (s)	χ_S (cm^3 mol^{-1})	χ_T (cm^3 mol^{-1})	α	γ
2	5.72850E-01	0.01001	4.75035	0.3308	0.7284
3	4.44912E-01	0.02301	3.14835	0.2959	0.6516
4	3.56140E-01	0.03738	2.35697	0.2846	0.6338
6	2.30695E-01	0.05765	1.57645	0.3023	0.6821
8	1.48240E-01	0.06641	1.19181	0.3392	0.7864
10	9.56223E-02	0.06858	0.96249	0.3777	0.9200
13	5.35059E-02	0.06648	0.74819	0.4164	1.1179

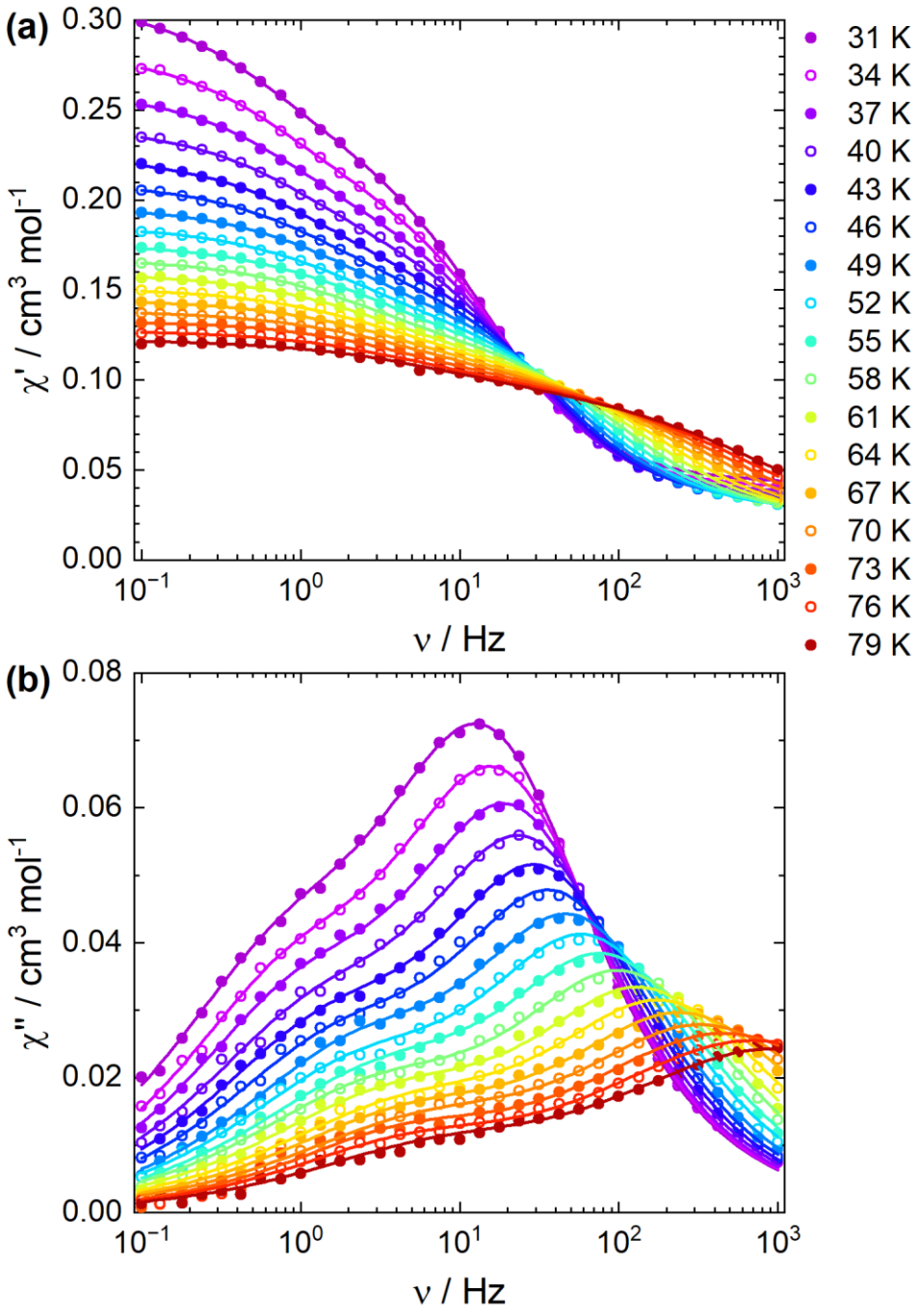

Figure S102. Fitting of the ac frequency dependence of the (a) in-phase (χ′) and (b) out-of-phase (χ″) components of the ac susceptibility for a 200 mM frozen solution of **1-Dy** in fluorobenzene (31–79 K) in dc zero field to the double generalized Debye model.

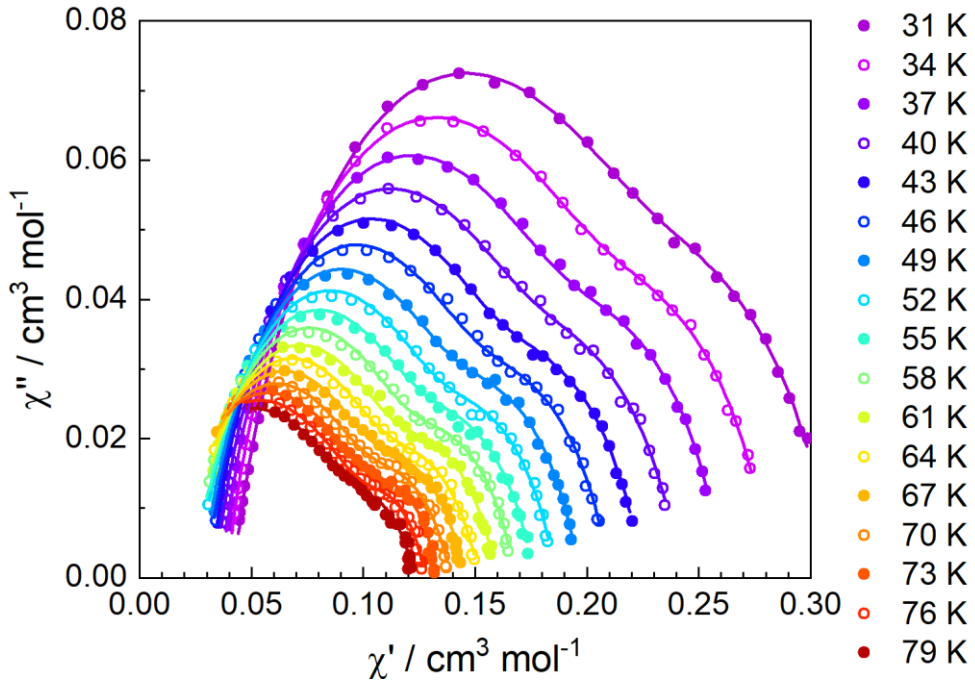

Figure S103. Cole-Cole plot showing fitting of ac data for 200 mM frozen solution of **1-Dy** in fluorobenzene (31–79 K) in dc zero field to the double generalized Debye model.

Table S10. Best fit parameters to the double generalised Debye model for 200 mM frozen solution of **1-Dy** in fluorobenzene in zero dc field.

T / K	τ_1 / s	τ_2 / s	$\Delta\chi_1$ / $cm^3\ mol^{-1}$	$\Delta\chi_2$ / $cm^3\ mol^{-1}$	$\Delta\chi_{total}$ / $cm^3\ mol^{-1}$	α_1	α_2
31	1.04415E-2	2.25283E-1	0.17777	0.09108	0.04179	0.2058	0.2689
34	8.60700E-3	1.96454E-1	0.16179	0.08204	0.0388	0.1980	0.2544
37	7.10859E-3	1.74266E-1	0.14764	0.07718	0.03625	0.1933	0.2556
40	5.73667E-3	1.38529E-1	0.13351	0.07446	0.03377	0.1897	0.2812
43	4.59411E-3	1.19845E-1	0.12339	0.06979	0.03159	0.1869	0.2768
46	3.74834E-3	1.01594E-1	0.11471	0.0656	0.02994	0.1889	0.2844
49	2.89406E-3	7.93483E-2	0.10535	0.06292	0.02842	0.1853	0.2807
52	2.35834E-3	7.74748E-2	0.10332	0.05675	0.02588	0.2065	0.2887
55	1.76599E-3	5.75630E-2	0.09354	0.0579	0.02501	0.2010	0.3189
58	1.40002E-3	5.97924E-2	0.09377	0.05141	0.02268	0.2268	0.3098
61	1.04517E-3	4.70191E-2	0.08731	0.05042	0.02195	0.2300	0.3266
64	7.73812E-4	3.78702E-2	0.08515	0.04708	0.01955	0.2492	0.3441
67	5.78735E-4	3.56011E-2	0.08622	0.04225	0.0166	0.2792	0.3314
70	4.23175E-4	3.12863E-2	0.08675	0.03844	0.01369	0.3127	0.3415
73	3.19045E-4	3.97106E-2	0.09895	0.02783	0.00621	0.3876	0.2726
76	2.13724E-4	3.70496E-2	0.10352	0.02416	0.00000	0.4279	0.2867
79	1.56363E-4	2.63243E-2	0.09881	0.02380	0.00000	0.4313	0.3224

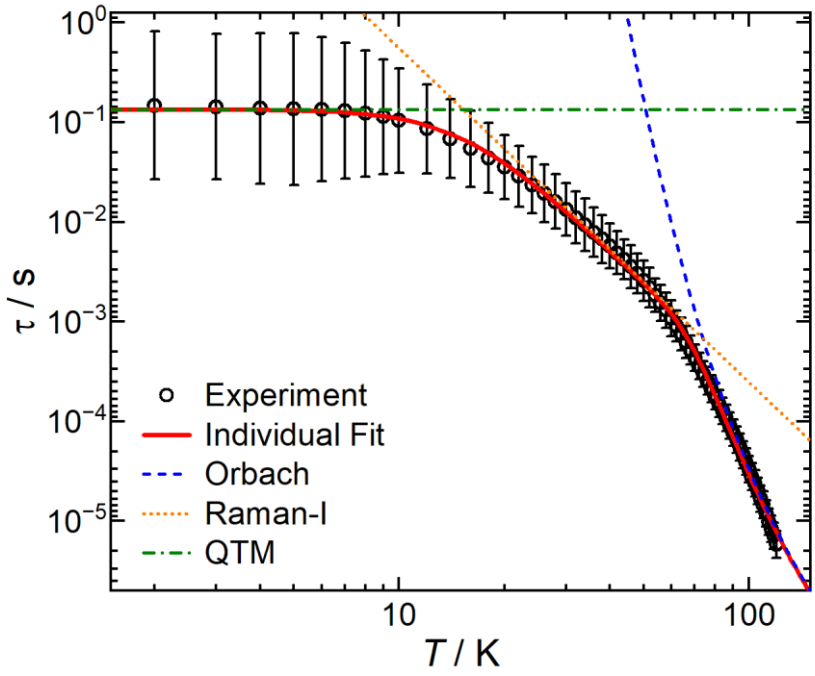

Figure S104. Temperature dependence of the magnetic relaxation time (τ) of **1-Dy** in zero dc field. Bars denote ESDs of distribution of times from the generalized Debye model.[3,4] Individual fit is of the zero dc field average relaxation times to Eqn 1, without errors.

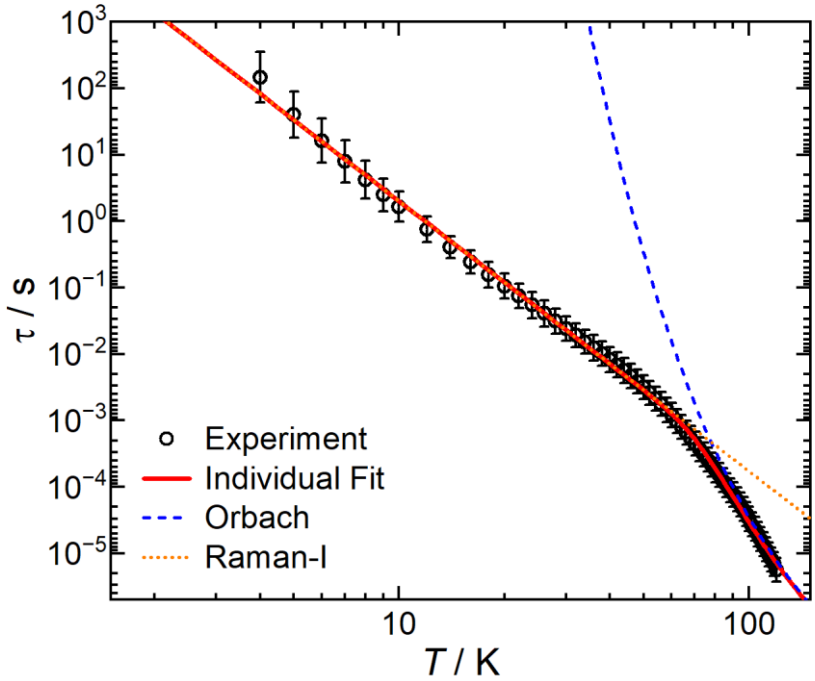

Figure S105. Temperature dependence of the magnetic relaxation time (τ) of **1-Dy** in 0.08 T dc field. Bars denote ESDs of distribution of times from the generalized Debye model.[3,4] Individual fit is of the 0.08 T field average relaxation times to Eqn 1 ($\tau_{QTM}^{-1} = 0$), without errors.

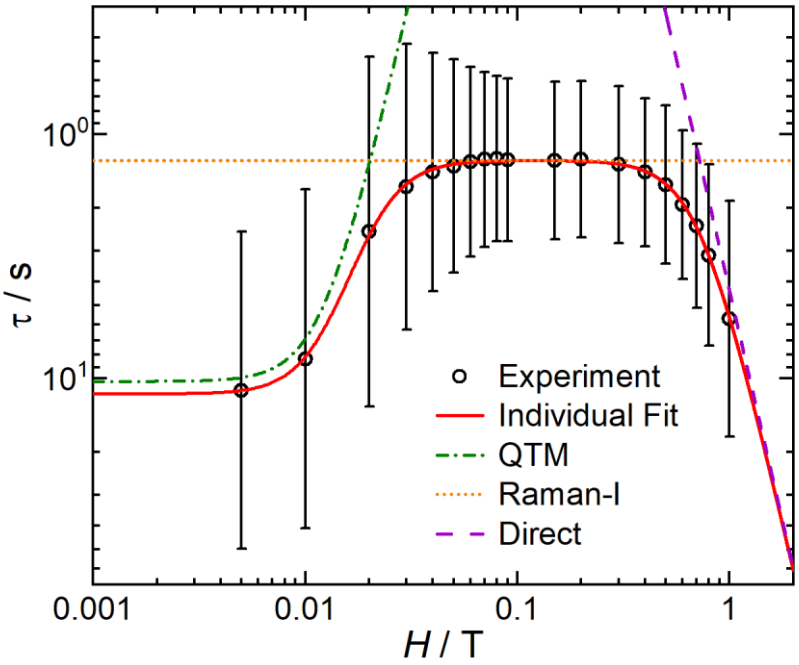

Figure S106. Field dependence of the magnetic relaxation time (τ) of **1-Dy** at 12 K. Bars denote ESDs of distribution of times from the generalized Debye model.[3,4] Individual fit is of the 12 K average relaxation times to Eqn 2, without errors.

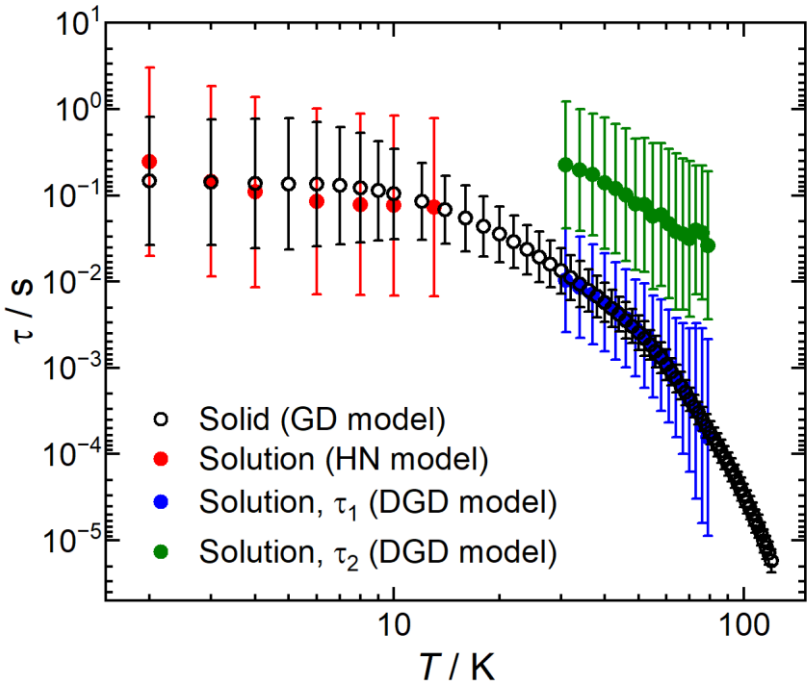

Figure S107. Comparison of relaxation times for **1-Dy** as a solid suspended in mineral oil in a polypropylene bag using the generalized Debye model (GD, black) and as 200 mM frozen solution in fluorobenzene using the Havriliak-Negami model (HN, red) or the double generalized Debye model (DGD, blue – short time, green – long time) to extract relaxation times. Bars denote ESDs of distribution of rates from the appropriate model.

8. CASSCF-SO calculations

Table S11. Electronic structure of **1-Dy** calculated with the crystal field parameters obtained from CASSCF-SO using the solid-state geometry of **1-Dy** in zero-field. Each row corresponds to a Kramers doublet.

Energy (cm^{-1})	Energy (K)	g_x	g_y	g_z	Angle[a] (deg)	Wavefunction	$<J_z>$
0.00	0.00	0.0	0.0	19.9	--	99.6% |± 15/2⟩	±7.5
427.96	615.74	0.0	0.0	16.9	0.8	98% |± 13/2⟩ + 2% |± 9/2⟩	±6.5
823.47	1184.74	0.1	0.1	14.0	1.6	94% |± 11/2⟩ + 5% |± 7/2⟩	±5.4
1149.15	1653.38	0.7	0.7	11.1	5.3	88% |± 9/2⟩ + 2% |± 13/2⟩ + 9% |± 5/2⟩	±4.3
1385.01	1992.73	1.3	2.6	8.2	10.6	76% |± 7/2⟩ + 5% |± 11/2⟩ + 1% |± 9/2⟩ + 1% |± 5/2⟩ + 15% |± 3/2⟩ + 2% |± 1/2⟩ + 1% |∓ 1/2⟩	±3.1
1531.01	2202.80	4.2	5.2	8.7	83.7	54% |± 5/2⟩ + 7% |± 9/2⟩ + 1% |± 7/2⟩ + 4% |± 3/2⟩ + 23% |± 1/2⟩ + 4% |∓ 1/2⟩ + 3% |∓ 3/2⟩ + 4% |∓ 7/2⟩	±1.7
1638.24	2357.08	1.2	2.3	15.0	87.5	46% |± 3/2⟩ + 12% |± 7/2⟩ + 4% |± 5/2⟩ + 1% |± 1/2⟩ + 14% |∓ 1/2⟩ + 2% |∓ 3/2⟩ + 19% |∓ 5/2⟩ + 1% |∓ 7/2⟩ + 2% |∓ 9/2⟩	±0.6
1709.26	2459.26	0.2	0.5	19.3	87.9	39% |± 1/2⟩ + 1% |± 7/2⟩ + 9% |± 5/2⟩ + 16% |± 3/2⟩ + 15% |∓ 1/2⟩ + 14% |∓ 3/2⟩ + 4% |∓ 5/2⟩ + 2% |∓ 7/2⟩	±0.2

[a] The angle between the g_z value of the excited Kramers doublet and the ground Kramers doublet.

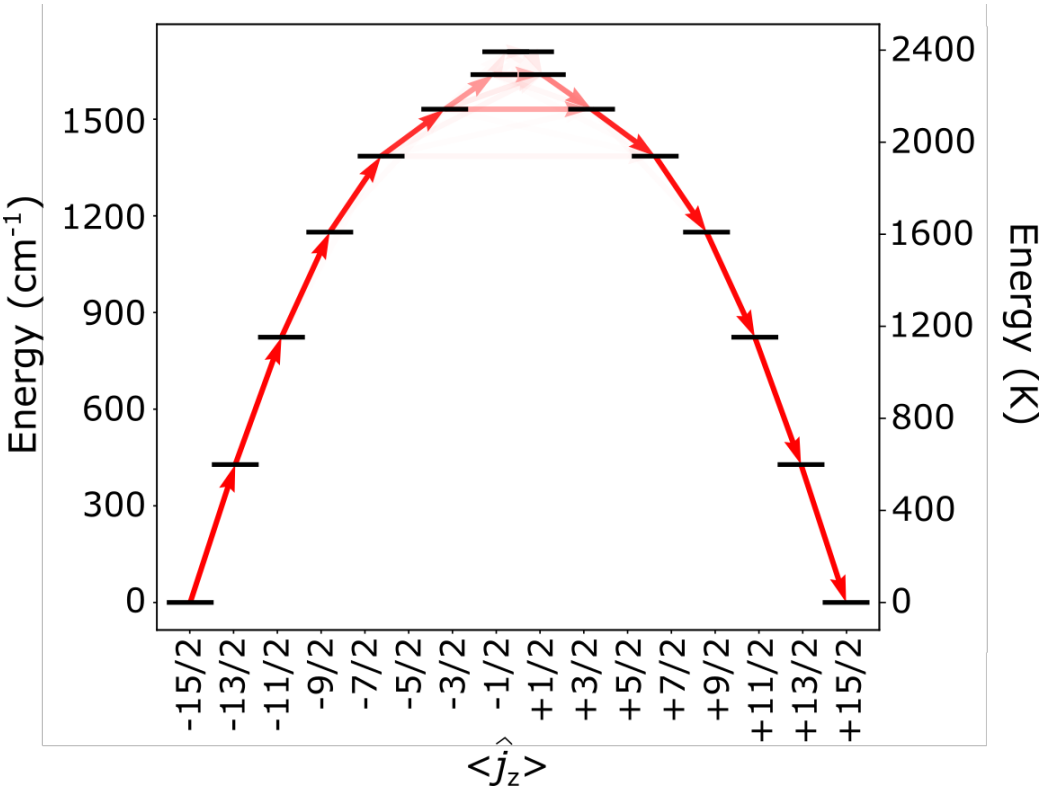

Figure S108. Energy barrier to magnetic relaxation for a model of **1-Dy**. Electronic states from CASSCF-SO calculations, labelled with their dominant m_J composition in the J = 15/2 basis. Arrows represent the Orbach relaxation pathway, where the opacity of the arrows is proportional to the transition probability approximated with the average matrix elements of magnetic moment connecting the states, $\gamma_{ij} = (1/3)[|\langle i|\mu_x|j\rangle|^2 + |\langle i|\mu_y|j\rangle|^2 + |\langle i|\mu_z|j\rangle|^2]$, normalized from each departing state and commencing from |–15/2>.

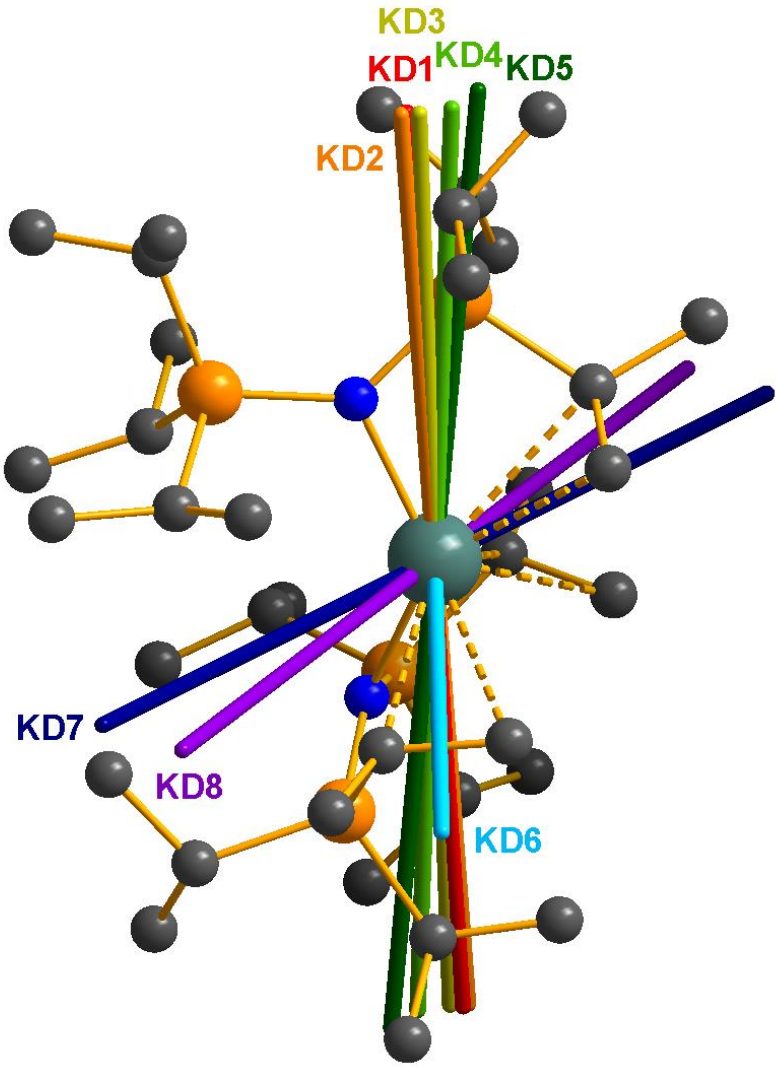

Figure S109. Structure of **1-Dy** cation with overlaid g_z vectors for Kramer's doublets (KD1–KD8) calculated with CASSCF-SO. Hydrogen atoms are omitted for clarity.

9. References

(1) Chilton, N. F.; Goodwin, C. A. P.; Mills, D. P.; Winpenny, R. E. P. The First Near-Linear Bis(Amide) f-Block Complex: A Blueprint for a High Temperature Single Molecule Magnet. *Chem. Commun.* **2015**, *51*, 101–103. https://doi.org/10.1039/C4CC08312A.

(2) Gransbury, G. K.; Corner, S. C.; Kragskow, J. G. C.; Evans, P.; Yeung, H. M.; Blackmore, W. J. A.; Whitehead, G. F. S.; Vitorica-Yrezabal, I. J.; Oakley, M. S.; Chilton, N. F.; Mills, D. P. AtomAccess: A Predictive Tool for Molecular Design and Its Application to the Targeted Synthesis of Dysprosium Single-Molecule Magnets. *J. Am. Chem. Soc.* **2023**, *145* (41), 22814–22825. https://doi.org/10.1021/jacs.3c08841.

(3) Reta, D.; Chilton, N. F. Uncertainty Estimates for Magnetic Relaxation Times and Magnetic Relaxation Parameters. *Phys. Chem. Chem. Phys.* **2019**, *21* (42), 23567–23575. https://doi.org/10.1039/C9CP04301B.

(4) Blackmore, W. J. A.; Gransbury, G. K.; Evans, P.; Kragskow, J. G. C.; Mills, D. P.; Chilton, N. F. Characterisation of Magnetic Relaxation on Extremely Long Timescales. *Phys. Chem. Chem. Phys.* **2023**, *25*, 16735–16744. https://doi.org/10.1039/D3CP01278F.